

**A Teleseismic Study of the Northern Cordilleran
Upper Mantle Beneath the SNORCLE Transect**

by

Andrew William Frederiksen

B.Sc., McGill University, 1994

A THESIS SUBMITTED IN PARTIAL FULFILLMENT OF
THE REQUIREMENTS FOR THE DEGREE OF
MASTER OF SCIENCE

in

THE FACULTY OF GRADUATE STUDIES
DEPARTMENT OF EARTH AND OCEAN SCIENCES

We accept this thesis as conforming
to the required standard

THE UNIVERSITY OF BRITISH COLUMBIA

December 1996

©Andrew William Frederiksen, 1996

In presenting this thesis in partial fulfilment of the requirements for an advanced degree at the University of British Columbia, I agree that the Library shall make it freely available for reference and study. I further agree that permission for extensive copying of this thesis for scholarly purposes may be granted by the head of my department or by his or her representatives. It is understood that copying or publication of this thesis for financial gain shall not be allowed without my written permission.

Department of Earth and Ocean Sciences

The University of British Columbia
Vancouver, Canada

Date Jan 2nd, 1997

Abstract

The study area of the SNORCLE Lithoprobe transect comprises the northern Canadian Cordillera and the northwestern Canadian shield. An array of five portable broadband seismographs has been deployed along the trend of the transect, to complement five permanent stations of the Canadian National Seismic Network and seven Alaskan short-period instruments. The objective of the experiment is to examine the physical state of the upper mantle along the transect. P-wave travel-time residuals up to 2 seconds have been measured, and analyzed using a non-linear tomographic technique, thereby recovering velocity structure between 100 and 600 km depth for the western portion of the transect.

Two significant P-wave mantle velocity anomalies have been located. The first, a relatively shallow high-velocity feature located at the western edge of the model, has been interpreted as being the edge of the Pacific slab from the southern Alaska subduction zone. The second is a large, tabular low-velocity anomaly centered at 60°N by 136°W , elongate northwest-southwest, dipping southeast, and reaching a depth of 450-500 km. This low-velocity anomaly is judged to reflect a thermal anomaly of the order of 100°C , with a possible compositional component. Multiple interpretations of the low-velocity feature are considered, the two main hypotheses being a mantle plume or a flow feature related to the proximity of the subducting slab and the opening of the northern Cordilleran slab window. The latter hypothesis is favored, due to the absence of other evidence for a plume in this region. In addition, the upper part of the low-velocity anomaly may reflect the influence of strain heating at lithospheric levels, related to the convergence of the Pacific and North American plates and the uplift of the St. Elias Mountains.

Contents

Abstract	ii
Table of Contents	iii
List of Tables	v
List of Figures	vii
Acknowledgements	viii
1 Introduction	1
1.1 Area of interest	1
1.2 History of plate motions	2
1.3 Geophysical data	7
1.4 Post-accretionary history of magmatism in the northern Cordillera	10
1.5 Terrane transport: controversies	11
1.6 Summary and motivation	13
2 The experiment	14
2.1 Rationale	14
2.2 Instrumentation	15

<i>CONTENTS</i>	iv
2.3 Deployment and events	16
2.4 Data quality and processing	19
3 Travel-time analysis	24
3.1 Rationale	24
3.2 Determination of travel times	26
3.3 The inverse problem	29
3.4 Linear inversion technique	32
4 Results	36
4.1 Residuals	36
4.2 Choice of inversion parameters	39
4.3 Resolution	44
4.4 Observed features	52
5 Discussion of results	59
5.1 The nature of the observed anomalies	59
5.2 Plume models for the observed low-velocity feature	63
5.3 Plate-related models for the observed low-velocity feature	65
5.4 Summary	70
Bibliography	73
A List of earthquakes used in this experiment	78

List of Tables

2.1 Stations used in this experiment.	17
---	----

List of Figures

1.1	Terranes of the Canadian cordillera	3
1.2	Detail: terranes and faults of the southern Yukon	4
1.3	Reconstruction of Pacific plate motions	5
1.4	Results of western-hemisphere S-wave tomography from Grand (1994)	8
1.5	Potential-field data for the northern Cordillera	9
2.1	Map of seismometer array	18
2.2	Event locations for travel-time inversion	19
2.3	Data quality for two events	21
2.4	Sample event section	23
3.1	Rationale for travel-time analysis	25
3.2	Cross-correlation and arrival-time picking	28
3.3	Grid knots used for travel-time inversion	31
4.1	Some contour maps of travel-time perturbations	37
4.2	Contour maps of perturbations after removal of station averages	38
4.3	Sample polar plots of travel-time perturbations gathered by station.	40
4.4	The effect of varying the degree of regularization for a linear inversion	42
4.5	Tradeoff curves for two linear iterations	43

LIST OF FIGURES

vii

4.6	Effect of non-linearity	44
4.7	Synthetic model from large-anomaly resolution test	46
4.8	Recovered model from large-anomaly resolution test	47
4.9	Depth sections from the checkerboard resolution test	48
4.10	Depth sections from the checkerboard resolution test (cont.)	49
4.11	E-W vertical sections from the checkerboard resolution test	50
4.12	N-S vertical sections from the checkerboard resolution test	51
4.13	Horizontal cross-sections through final model	53
4.14	Horizontal cross-sections through final model (cont.)	54
4.15	SW-NE cross-sections through final model	55
4.16	NW-SE cross-sections through final model	56
4.17	Event statics for final model	56
5.1	Position of the Alaskan slab	60
5.2	Geometry of a slab window	67
5.3	Cordilleran slab windows	68
5.4	Conceptual model of flow due to the opening of a slab window	70

Acknowledgements

Many people participated in the project this thesis describes. In particular, I would like to acknowledge the participation of Michael Bostock, who designed and supervised this project; Andy Langlois, Scott Dodd, and the operators of the portable stations; John Cassidy and Roger Hansen, for providing permanent-station data from both sides of the border; John VanDecar, for his excellent software and advice; Carl-Georg Bank for advice, moral support, and Fortran-to-English translation; the members of the UBC seismology group, John Amor, and Gerry Grieve, for advice and technical support; and the members of my thesis committee, Bruce Buffett, Derek Thorkelson, and Bob Ellis. Arthur Calderwood, Ben Edwards, Don Francis, and Shi Lang provided helpful geological insights. The use of the first person plural throughout the thesis is intended to reflect the collaborative nature of this project.

Chapter 1

Introduction

1.1 Area of interest

The Yukon Territory lies at the northern end of the Cordilleran fold and thrust belt, where the main belts of the Cordillera converge and turn a corner into Alaska. It consists of a collage of terranes of Mesozoic to Paleozoic (and possibly Precambrian) ages, divided by faults, and intruded by plutons, and locally overlain by Cenozoic volcanic and sedimentary strata. To the east of the terrane assemblage are the folded and thrust sedimentary rocks of the ancient North American margin, which lie along the North American craton.

This area lies adjacent to the Pacific active margin of the North American Plate, opposite a corner in the Pacific Plate where strike-slip motion along the Queen Charlotte-Fairweather transform fault becomes subduction along the Aleutian Trench. The region at the corner is tectonically complicated; at its apex lies the Yakutat Terrane, a block which was carried north along the Queen Charlotte fault and is colliding with the North American plate at the trench. A strike-slip transition fault between this terrane and the Pacific Plate may be taking over, as the strike-slip motion vaults westward to avoid the stopped terrane (von Huene, 1989).

A map of the principal terranes inland is shown in figure 1.1. They consist of a mix of per-

icratonic terranes (containing sedimentary material related to the North American craton) and accreted terranes (brought in from elsewhere, such as from island arcs). The entire Cordillera has been overprinted by arc magmatism from mid-Cretaceous to early Tertiary time (Monger and Nokleberg, 1996).

The most interesting recent structural features of this area are the Tintina and Denali fault zones (figure 1.2). Both are major dextral strike-slip fault zones striking northwest-southeast. The Denali Fault follows the boundary between the Coast Belt and the Insular Belt; the Tintina Fault, which lies about 300 km east of the Denali, lines up with the Rocky Mountain Trench farther south. The estimated displacements for these faults are approximately 400 km for the Denali, and 450 km or more for the Tintina (Lowe et al., 1994).

The Tintina Fault displays little seismicity, and is not thought to be currently active. The Denali Fault Zone displays considerable seismic activity, and is currently slipping. However, it is the Tintina Fault that marks a more major divide in the geophysical data (see section 1.3). The Teslin Fault is a poorly understood fault between the Denali and Tintina faults (Lowe et al., 1994).

1.2 History of plate motions

Several very complete reconstructions of the motions of oceanic plates in the northeastern Pacific have been performed, retracing their motions back to the mid-Cretaceous (Atwater, 1989, Engebretson et al., 1985, Stock and Molnar, 1988). Although there is appreciable variation in the timing and plate velocities determined by different methods, the overall history of Pacific plate motions off the coasts of what are now Alaska and northern British Columbia is well understood as far back as 120 Ma. Figure 1.3 summarizes one of these reconstructions.

In the mid-Cretaceous, the Farallon Plate dominated the eastern Pacific. Its motion was obliquely convergent with the North American Plate, but the relative velocity between the two

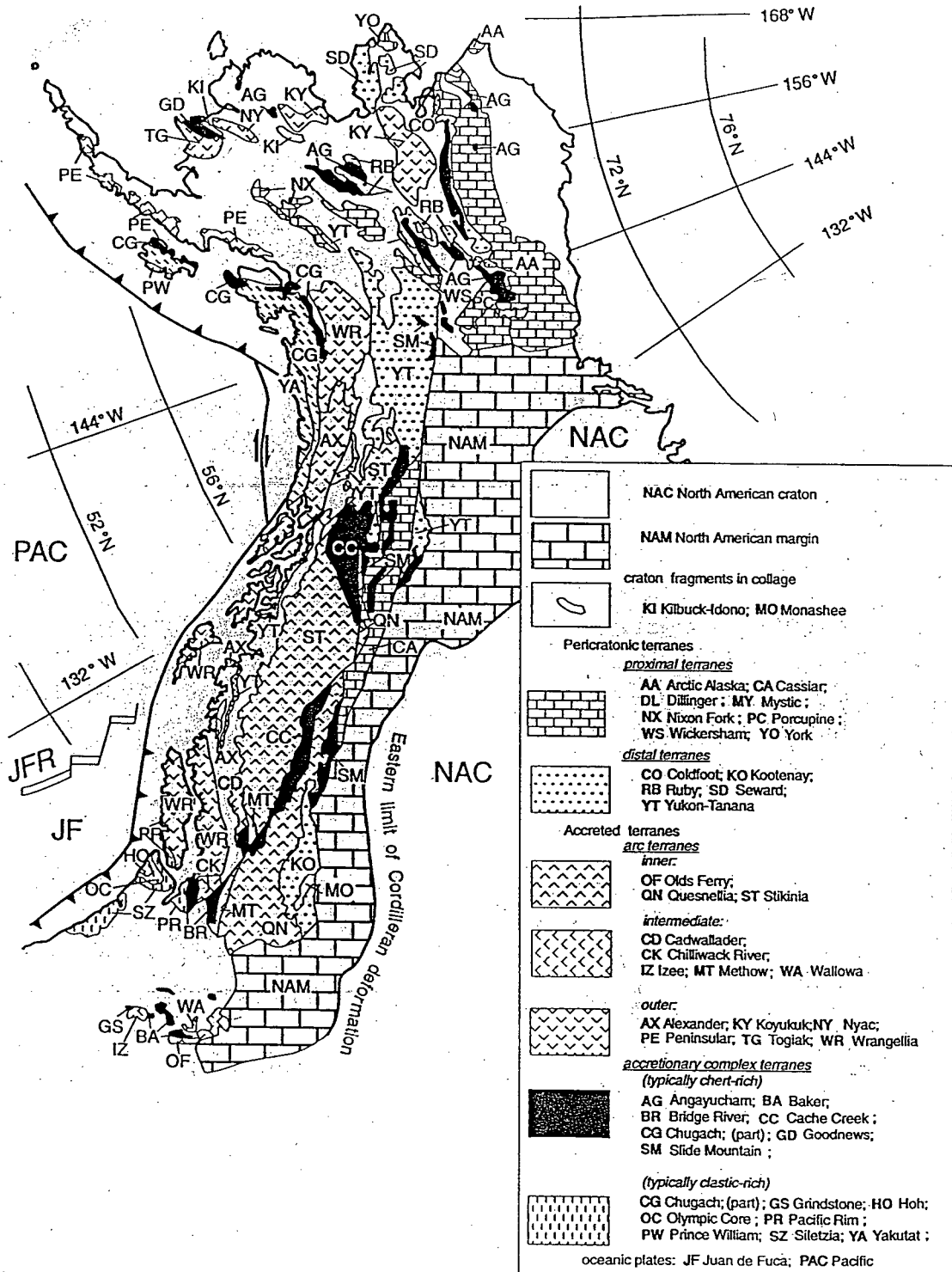


Figure 1.1: Map of the terranes of the Canadian cordillera, from Monger and Nokleberg (1996).

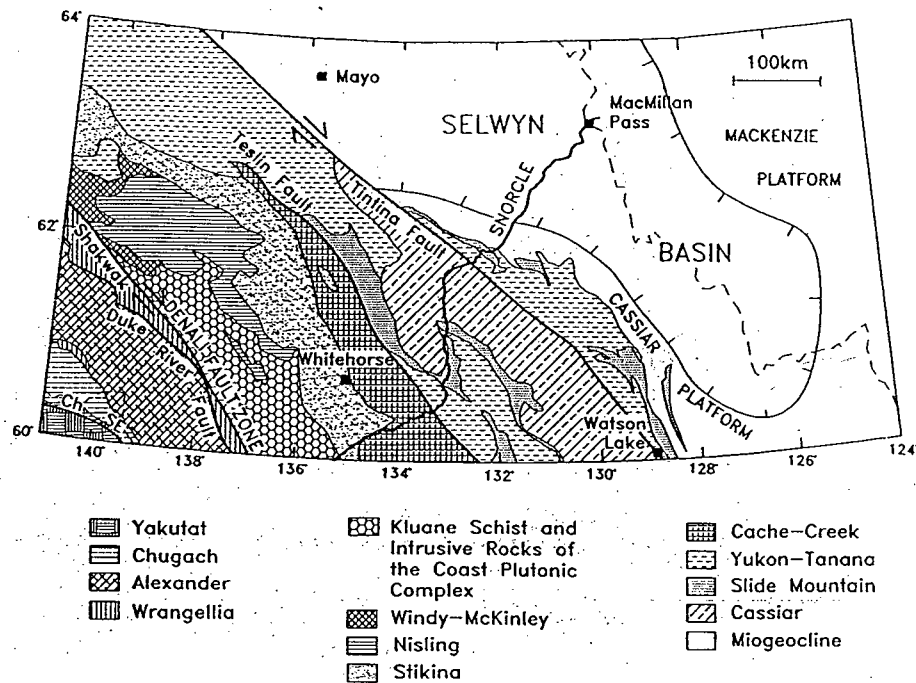


Figure 1.2: Detail of the terranes and major faults of the southern Yukon. From Lowe et al. (1994).

was quite small; the strike-slip component may have changed from left-lateral to right-lateral between 140 Ma and 110 Ma (Engebretson et al., 1985). At about 83 Ma, a spreading center formed in the Farallon Plate, dividing it into southern and northern pieces. The northern portion is known as the Kula Plate; the southern portion retained the Farallon name. There is some controversy over the location of the divide between the two plates between California and Mexico, but by all accounts the Kula plate was the one present along the coast adjacent to our area of interest (Atwater, 1989).

The Kula plate was quite remarkable for its velocity; in the hot-spot reference frame, it was moving northward at approximately 120 mm/yr (Atwater, 1989). Its motion relative to the North American plate was obliquely convergent, but dominated by the right-lateral strike-slip component. This relative motion became increasingly convergent into the Paleocene.

Due to its high velocity, the Kula Plate was quite short-lived (approximately 83 Ma to 43

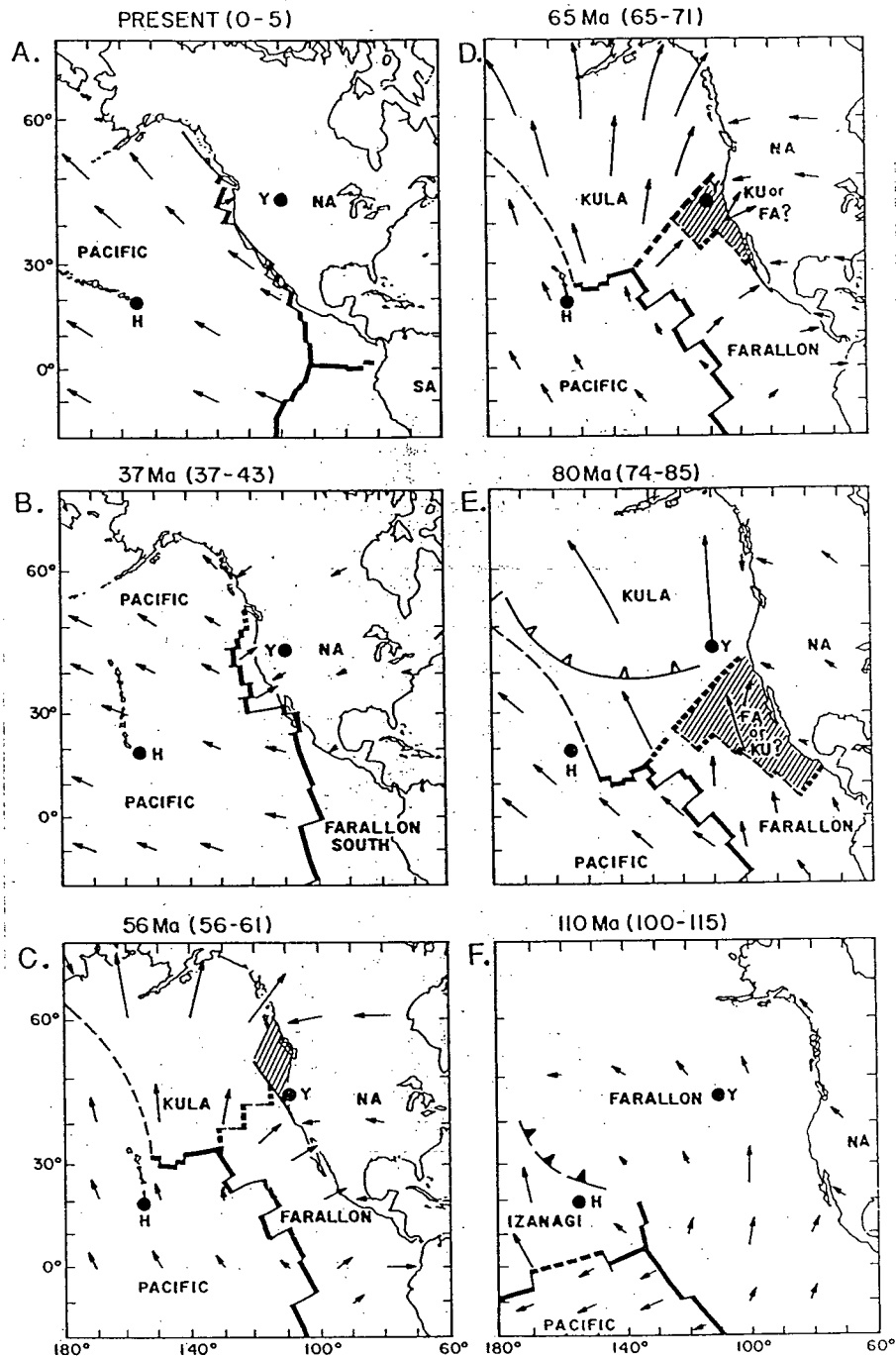


Figure 1.3: Paleogeographic map of the plates of the western Pacific, Cretaceous to present. The arrows indicate plate velocities relative to the hot-spot reference frame, their lengths corresponding to 10 Ma of motion. From Atwater (1989).

Ma); as it subducted beneath North America and eastern Siberia, the Pacific Plate gradually moved eastward. The Kula Plate was gone by the mid-Eocene, most of it having subducted and the remainder having merged with the Pacific plate when the Pacific-Kula ridge shut down. A section of the Farallon remained west of Mexico and South America, eventually becoming the present-day Cocos and Nazca plates, while some small sections remained to the north, including the present-day Juan de Fuca and Explorer plates (Atwater, 1989; Engebretson et al., 1985).

The issue of how these different plates interacted with North America is far from resolved. The uncertainties stem from the fact that the relative motions between North America and the various oceanic plates that interacted with it were generally highly oblique; therefore, there could have been a mix of subduction and strike-slip faulting at different points along the boundary, much as there is today. This leads in to a debate about the origin and transport of the accreted terranes that make up western North America – to what extent are they volcanic arcs rafted in by subduction, as opposed to blocks carried up the coast by strike-slip faulting (Irving et al., 1995)? As for the Yukon – how much strike-slip motion has there been, and can it be reconciled with motion farther south?

This history of plate motions also has important direct implications for the evolution of the upper mantle beneath the northern Cordillera. The subduction of the Kula Plate, in particular, is likely to have exerted considerable influence on the upper mantle, by both disrupting any existing structures and driving mantle circulation. The strike-slip motion between the Pacific and North American plates may also have driven shearing flow in the upper mantle. Finally, the ongoing subduction of the East Pacific Rise and separation of the Explorer and Pacific slabs may have complicated flow patterns beneath the northern Cordillera. This will be discussed in more detail in section 5.3.

1.3 Geophysical data

Although no previous regional seismic tomography experiments have taken place in the northern Cordillera, the region has been included in global and near-global tomographic studies. Grand (1994) performed a tomographic S-wave study of the mantle beneath the Americas and surrounding oceans. Although our area of interest cannot be well resolved by such a large-scale experiment, it does appear as a region of low to moderate upper-mantle velocity, the velocity being particularly low in the upper 100 km. Overall, the area exhibits higher upper-mantle velocities than more southern regions of the Cordillera, and lower velocities than Alaska (see figure 1.4).

A local-earthquake tomography experiment for southern Alaska is described in Zhao et al. (1995). An image of the crust and uppermost mantle was obtained to a maximum depth of 190 km. The main feature located was, not surprisingly, the subducting Pacific slab below southern Alaska and the Aleutian islands (its presence was included as a priori information). In addition, the authors located low-velocity anomalies associated with active volcanism at the surface, which dip to landward and descend to just below 100 km. The location and orientation of the slab at its eastern edge is somewhat uncertain; there is a tremendous drop-off in Benioff zone seismicity east of 145°W , associated with a bend in the descending slab, and so the location of the slab east of 145°W is poorly constrained (Stephens et al., 1984; Page et al., 1989).

Much regional geophysical work on this area is planned as part of the SNORCLE Lithoprobe transect; at the time of writing, however, only gravity and aeromagnetic data are available. Lowe et al. (1994) examined aeromagnetic and gravity data (figure 1.5). The authors located a gravity high and magnetic low associated with the northern Yukon-Tanana terrane (interpreted as a region of young extension in Lowe and Cassidy (1995)). In addition, they remarked on a considerable change in gravitational and magnetic character across the Tintina Fault, suggesting that it is a crustal-scale feature and not a shallow tear fault.

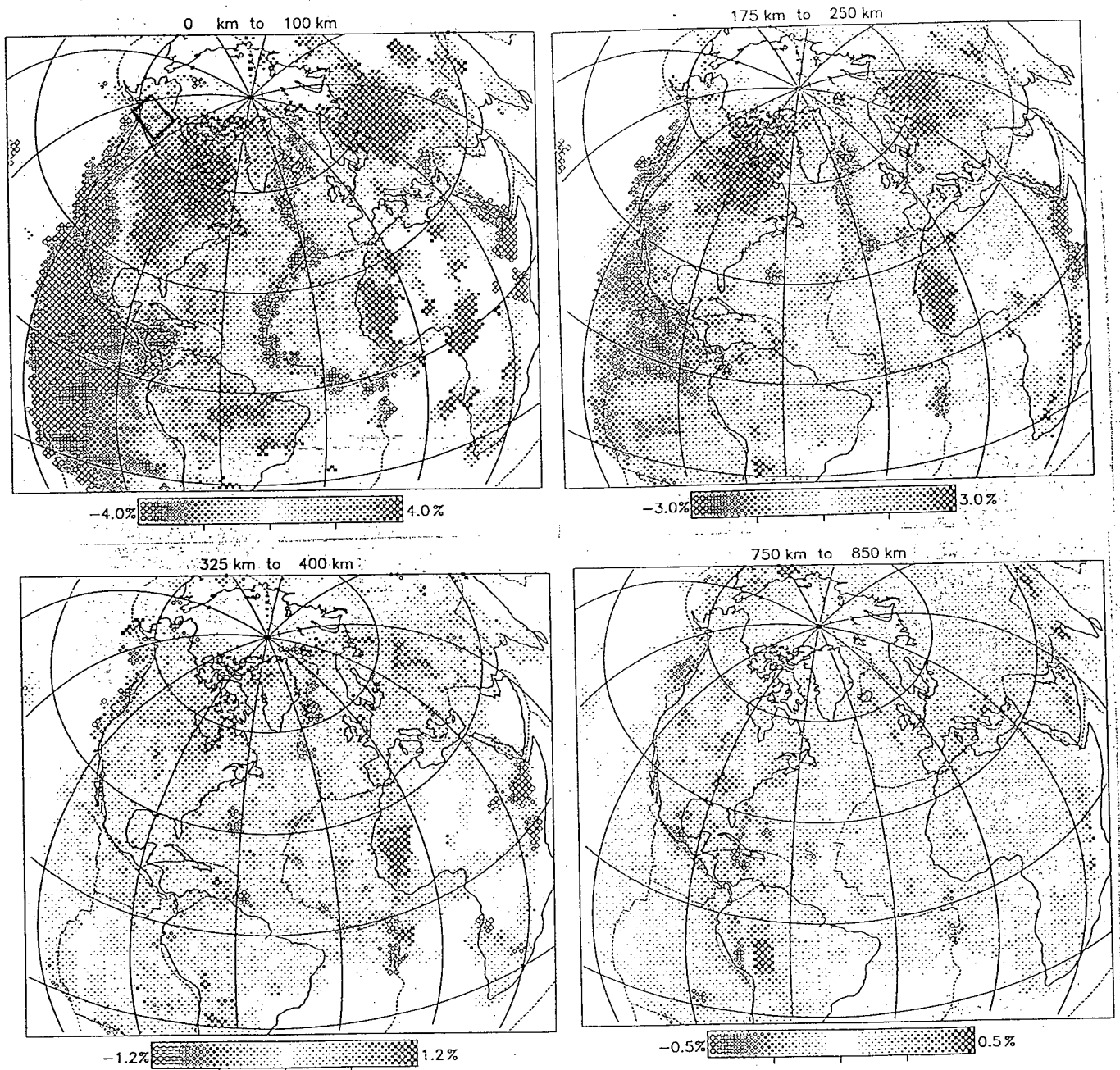


Figure 1.4: Results of S-wave mantle tomography from Grand (1994) for four different depths. Open circles represent low velocities; filled circles represent areas of high mantle S-wave velocity. The area of interest of this study is enclosed in a rectangle.

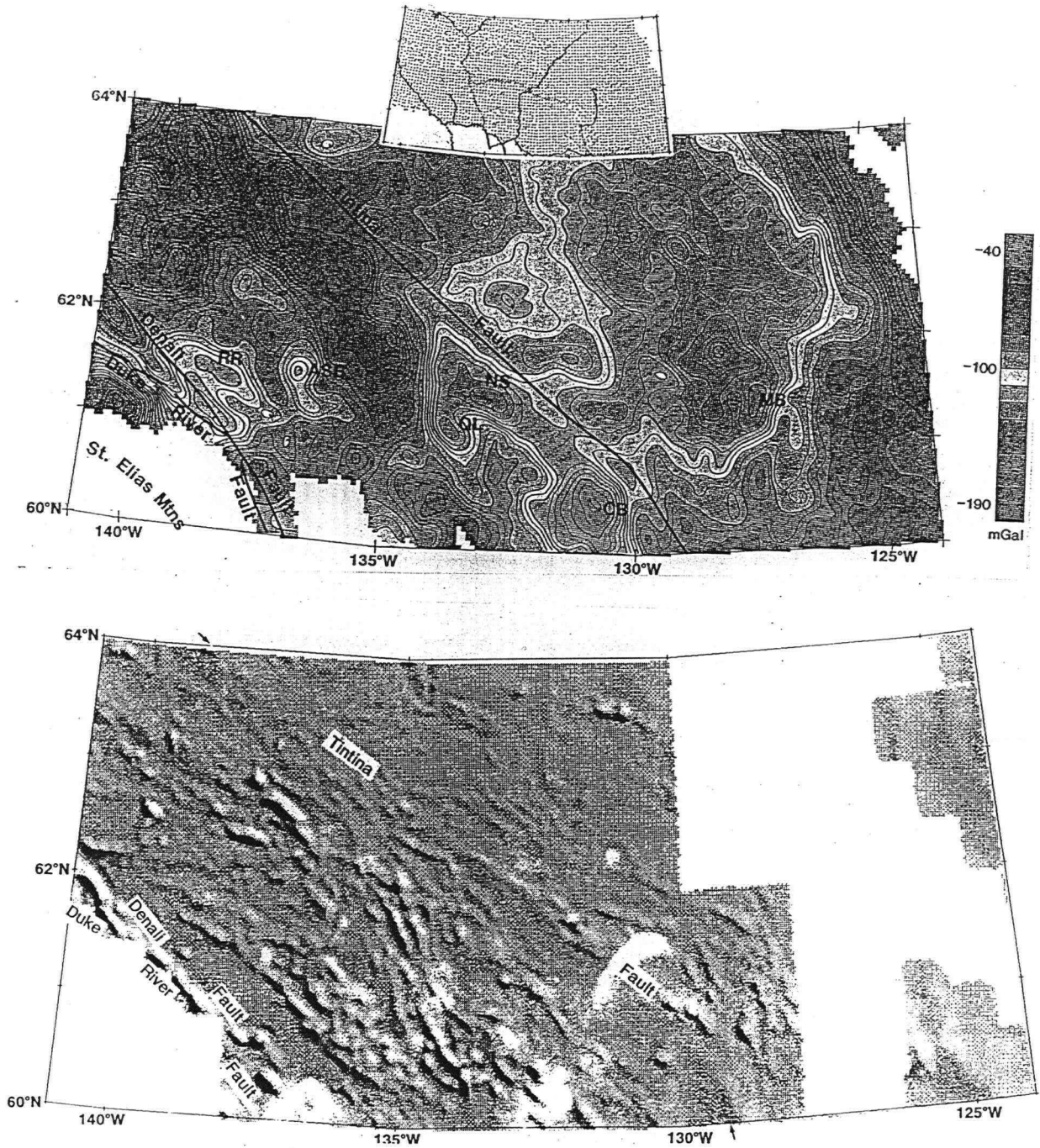


Figure 1.5: Bouger gravity anomaly (top) and total-field magnetic (bottom) data for the northern Cordillera, from Lowe et al (1994). The major faults are indicated.

In Lowe and Cassidy (1995), receiver-function analysis of teleseismic earthquakes at two permanent broad-band stations (Dawson Lake and Whitehorse, also used in this study) was combined with Bouger gravity data to determine the variation in crustal thickness between the Tintina and Denali faults. The authors conclude that there is an abrupt transition between thicker crust (≈ 39 km) south of 63°N and thinner crust (≈ 35 km) farther north. This difference was attributed to young extension in the northern region, associated with stress transfer between the Denali and Tintina fault zones.

1.4 Post-accretionary history of magmatism in the northern Cordillera

As the southern Yukon lies near an active margin and is composed of accreted terranes of various ages, it has been much affected by arc volcanism. Most of the area was included in the mid-Cretaceous to early Tertiary magmatic arc (Monger and Nokleberg, 1996) generated by the subduction of the Kula plate. This arc, and its associated plutonism, volcanism, and metamorphism, culminated in the mid-Eocene (circa 43 Ma) with the final consumption of the Kula plate (Erdmer and Mortensen, 1993). Much of the arc-related volcanic rocks from this period have been eroded away, and the plutons have been exposed.

It is possible that some of the rocks deposited during the lifetime of this arc may not be arc-related. The Late Cretaceous Carmacks Group (around 70 Ma), which once covered much of the southwest Yukon, includes flood basalts and has been interpreted as being plume-related (Johnston et al., 1996); this interpretation is examined further in section 1.5.

After the mid-Eocene, the change to strike-slip motion on the Queen Charlotte-Fairweather fault ended arc magmatism through most of this region, the exception being the Tertiary Wrangell Volcanic Belt northwest of the Saint Elias Mountains, which is of mixed arc-intraplate

character (Souther and Yorath, 1991; Skulski et al, 1991). All other volcanism in this region since then has been comparatively minor (Francis, pers. comm.; Souther and Yorath, 1991). Tertiary and Quaternary volcanism in the northern Cordillera exclusive of the Wrangell Volcanic Belt has been limited to small-volume eruptions of alkaline to tholeiitic magma (such as those of the Stikine Volcanic Belt); such eruptions have occurred at points all along the Canadian Cordillera, and may be related to minor intervals of extension. One example is the Atlin area volcanics in northwest British Columbia, on the southern boundary of our study area, described in Edwards et al. (1996).

1.5 Terrane transport: controversies

The tectonic history of the terranes of the northern Cordillera is a matter of some debate. At issue is the importance of strike-slip motion in terrane transport, and the degree to which the terranes of the Cordillera were rigidly attached after accretion. The principal difficulty in answering this question is that estimates of geological displacements along faults have generally yielded far less strike-slip motion than paleomagnetic measurements require; as well, estimates of fault slip from the Yukon do not match those from farther south (Monger and Nokleberg, 1996; Johnston et al, 1996; Irving et al., 1995).

Paleolatitudes determined magnetically from Cretaceous igneous rocks generally indicate over 1000 km of motion since Cretaceous time. In Umhoefer et al (1989), paleomagnetic data from rocks in B.C. and Alaska are used to argue that a large block of Alaska, the Yukon, British Columbia and northern Washington (referred to as "Baja British Columbia") lay at the paleolatitude of Mexico around 90 Ma (requiring about 2500 km of northward displacement since in the Coast Belt), and that this is consistent with reconstructions of oceanic plate motions for the region, assuming that this block was carried northward by the Kula plate.

Irving et al. (1995) described paleomagnetic measurements for the Spences Bridge Group,

a mid-Cretaceous volcanic group lying in the Intermontane Belt in south-central B.C., which they placed at a paleolatitude of about 51° , requiring about 1100 km (± 600 km) of northward displacement. This is not incompatible with the Baja B.C. model, assuming that the "Baja B.C." block did not remain rigid, and therefore that post-Cretaceous displacement increases westward. The Spences Bridge Group results can be reconciled with northern Cordilleran geology, as it is not difficult to accommodate this much displacement on the existing faults; the Denali and Tintina faults together could accommodate this much. In the southern Cordillera, however, it is difficult to accommodate this much motion along the known faults; the authors therefore proposed a major unrecognized dextral strike-slip fault located somewhere in the Omineca Belt, active during the Late Cretaceous or Paleocene.

Paleomagnetic measurements have also been performed on the rocks of the Carmacks Group (briefly described in section 1.4); these rocks, located between the Denali and Tintina faults, were found to have been displaced by 1900 ± 700 km, placing them at the present-day latitude of Oregon at 70 Ma. This would place them in the vicinity of the Yellowstone hotspot at the time of their deposition; given geochemical evidence suggesting a possible plume origin for these rocks, the authors propose that they represent the Late Cretaceous expression of the Yellowstone hotspot (Johnston et al., 1996).

In order to reconcile these paleomagnetic results with Southern Cordilleran geology, two possibilities present themselves: either there is a large-scale source of error in the paleomagnetic data (such as unrecognized tilting, although tilting was corrected for in the paleomagnetic results), or there has been considerable unrecognized strike-slip motion in the southern Canadian Cordillera. This study is unlikely to shed much direct light on this issue; however, major transitions in the crust may reflect major transitions in the underlying mantle. As well, the subduction of the Kula plate is likely to have exerted a considerable influence on the upper mantle in this area.

1.6 Summary and motivation

The northern Cordillera has experienced continuous tectonic activity since the Cretaceous: oblique subduction up to the mid-Eocene, and strike-slip deformation afterward. The latter is expressed by the Denali and Tintina fault zones (particularly the Denali after the Eocene). The total amount of post-Cretaceous strike-slip motion is in dispute, as paleomagnetic data require over 1000 km of motion, an amount which is difficult to reconcile with what is known about strike-slip motion in the southern Canadian Cordillera. The history of magmatism in this area reflects this plate-tectonic history: there was extensive arc magmatism until the mid-Eocene, after which magmatism has been limited to relatively small-volume alkaline volcanos which may be extension-related. Some of the Cretaceous rocks (the Carmacks group) may be plume-related.

The structure and history of surface crustal rocks are likely to reflect the structure and evolution of the upper mantle beneath the northern Cordillera. We may expect some form of transition in the upper mantle between the more stable eastern portion of the Cordillera and the western portion where the most extensive deformation occurred, as well as between the Cordillera and the stable North American craton. As well, the structure of the upper mantle may provide clues as to the origin of recent magmatism in the region. The plate tectonic history of this area places limits on the age of upper mantle structures; in particular, it is unlikely that any pre-Eocene structures persist in the sub-northern Cordilleran mantle, due to the disruptive effect of the subduction of the Kula plate. With these factors in mind, the objective of this thesis is to examine large-scale upper mantle structure beneath the northern Cordillera and so provide constraints on the current state and past history of the region.

Chapter 2

The experiment

2.1 Rationale

Obtaining a detailed seismic image of the upper mantle beneath a given region is difficult to accomplish by conventional means. The main problem for controlled-source work is the difficulty in transmitting sufficient energy from a near-surface, anthropogenic source to appreciable distances below the Moho. Some recent large-scale refraction lines have been designed specifically to recover upper-mantle information, such as the 1995 Deep Probe experiment (Gorman et al., 1996). Peaceful nuclear explosions have been used for this purpose in the Soviet Union (Ryberg et al., 1996). In any case, nothing short of a nuclear explosion will produce seismic energy comparable to that which is generated on a daily basis by earthquakes. Therefore, passive seismic techniques are an obvious means to obtain information about the upper mantle to considerable depth.

Although the study area is seismically active, northern Cordilleran regional seismicity occurs entirely at shallow depths, and so fails to effectively illuminate the mantle, as the direct S and P arrivals propagate along paths which are predominantly crustal. This study is therefore based on distant earthquakes, more specifically events occurring in the *teleseismic* range. Teleseismic

earthquakes are those that occur sufficiently distant from the receiver that the main S and P phases bottom below the upper mantle discontinuities (i.e. below 660 km depth), and sufficiently close that the phases bottom above the core-mantle boundary, thus avoiding triplications that can complicate extraction of accurate travel times. This translates to an epicentral distance range of approximately 30° to 110° . An advantage of using teleseismic earthquakes is that much of the ray path outside of the area of interest is common for all stations, and may therefore be accounted for by a simple static correction; this is explained in more detail in chapter 3.

2.2 Instrumentation

The Geological Survey of Canada operates a sizable network of permanent seismic stations, known as the Canadian National Seismic Network. Five of these stations were used for this experiment: stations DAWY (Dawson City, Yukon), DLBC (Dease Lake, B.C.), HYT (Haines Junction, Yukon), WHY (Whitehorse, Yukon), and YKW3 (one of four broad-band stations included in the Yellowknife Array, Yellowknife, N.W.T.) All of these are broad-band, three-component stations, with the exception of station HYT, which is a vertical short-period instrument.

In addition, through the assistance of Roger Hansen at the University of Alaska (Fairbanks), seismograms from seven Alaskan short-period permanent stations were incorporated into the data set. These stations provide coverage at the western edge of the study area.

To complement these stations and better cover the region of the SNORCLE transect, five portable seismic stations were installed in the Yukon and eastern Northwest Territories: stations FLSN (Fort Liard, N.W.T.), FPSN (Fort Providence, N.W.T.), FSSN (Fort Simpson, N.W.T.), LKSN (Lutsel Ke, N.W.T.), and WLSN (Watson Lake, Yukon). The locations of these instruments were constrained by the practical difficulties involved in locating year-round sites with dependable electric power in such a remote area. The instruments used were Guralp

CMG-3T 3-component broadband seismometers, recorded onto Interay NARS CSD 20 data loggers. These data loggers record onto four-millimeter digital audio tape (DAT) cartridges that are easily changed in the field. See table 2.1 for detailed information about the stations used in this study.

2.3 Deployment and events

Figure 2.1 shows the locations of the stations deployed for this experiment. The general orientation is along a line trending approximately east-west, with broader off-line coverage in the Cordillera. The portable stations were active in this deployment for the one-year period from July, 1995, to July, 1996; in addition, a few earlier archived events from the permanent stations were used to improve the event coverage from the east and north. The portable stations were deployed at sites with available AC power; local station managers monitored the sites and mailed the tapes to Vancouver on a monthly basis. The deployment of the instruments and servicing of the sites were performed by Andy Langlois, a technician for the Geological Survey of Canada based in Yellowknife.

The event set used for travel-time inversion is plotted in figure 2.2; in addition, a large number of events from Alaska (particularly the Aleutian Islands) were recorded, and may be used in future work, although they occurred too close to the array to be used as teleseismic events. As the figure shows, azimuthal coverage is good. The majority of events occur along the western Americas-western Pacific "ring of fire", which is unfortunately largely in line with the array, and so does not provide broad azimuthal coverage. Fortunately, there are a large number of southern Pacific events (such as from Fiji and Tonga) which fall just inside the edge of the teleseismic range and neatly fill in much of the southwestern quadrant. A scattering of Eurasian (Alpine-Himalayan) events provide some coverage to the north. The main gaps are the range of back azimuths from 40° to 110° , in which there are only a small number of

Table 2.1: Stations used in this experiment.

Station	Type	Lat. ($^{\circ}$ N)	Lon. ($^{\circ}$ W)	El. (m)	Samp. (Hz)	Components
BCP	Alaska short-period	59.953	139.635	396	120	Vertical
CYK	Alaska short-period	60.083	142.485	10	120	Vertical
DAWY	CNSN broad-band	64.053	139.432	346	40	3-comp.
DLBC	CNSN broad-band	58.437	130.027	978	40	3-comp.
FLSN	Portable broad-band	60.402	123.820	700	20	3-comp.
FPSN	Portable broad-band	61.050	117.438	119	20	3-comp.
FSSN	Portable broad-band	61.774	121.299	161	20	3-comp.
HYT	CNSN short-period	60.825	137.504	1416	100	Vertical
LKSN	Portable broad-band	62.400	110.730	500	20	3-comp.
PNL	Alaska short-period	59.668	139.397	585	120	Vertical
SSP	Alaska short-period	60.179	142.841	460	120	Vertical
WAX	Alaska short-period	60.448	142.851	991	120	Vertical
WHY	CNSN broad-band	60.660	134.881	1292	40	3-comp.
WLSN	Portable broad-band	60.115	128.751	675	20	3-comp.
YAH	Alaska short-period	60.359	141.745	2135	120	Vertical
YKU	Alaska short-period	59.554	139.725	40	120	Vertical
YKW3	CNSN broad-band	62.562	114.605	198	20	3-comp.

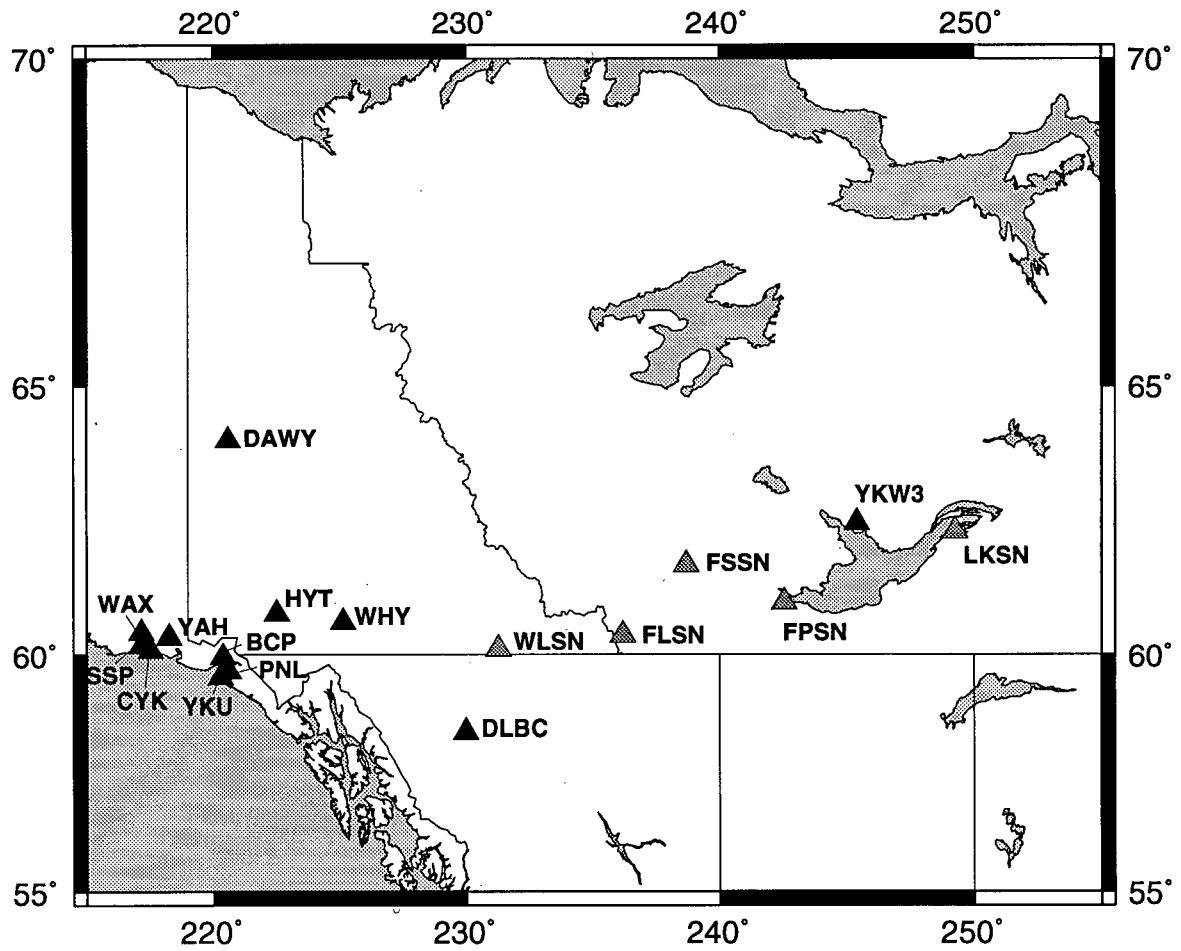


Figure 2.1: A map of the array of seismometers used in this experiment. Permanent stations are shown in black; temporary stations are shown in gray.

Mid-Atlantic Ridge earthquakes, and the range from 180° to 220° .

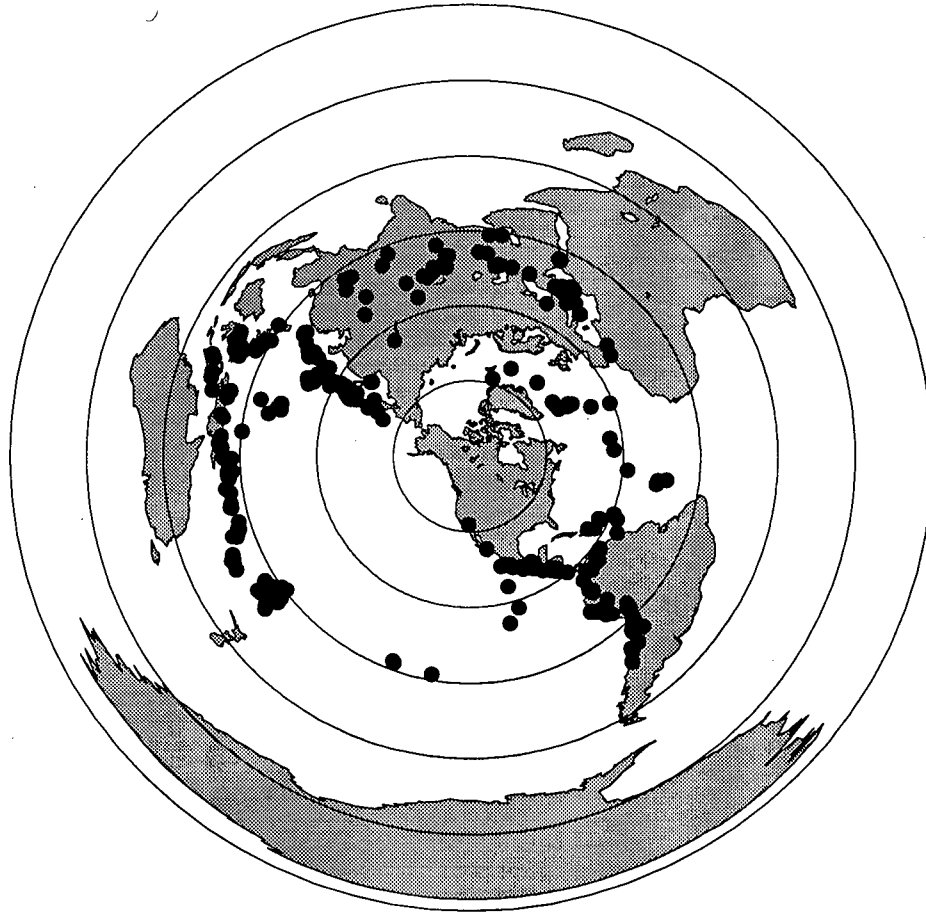


Figure 2.2: A map of the event locations used for the P-wave travel-time inversion, using a projection equidistant from the approximate center of the array. The circles mark 30° increments in distance.

2.4 Data quality and processing

Treatment of the data from the temporary stations presented a number of problems, due to both difficulties with the sites and problems with the instrumentation. The Interay data loggers depend on GPS antennae for accurate timing; unfortunately, the GPS systems were not locked

to the satellites for a considerable proportion of the recording time, some of the timing outages lasting over a month. Due to the difficulties involved in performing regular maintenance on stations located in such a remote area, the problem was not detected until well into the recording period. In addition, the internal timing system of the data loggers proved to be somewhat unpredictable during periods of no GPS lock, occasionally exhibiting large clock shifts with no apparent cause.

Fortunately, header information included in the field tapes provided complete information on the state of the GPS system and the behavior of the internal clock. We therefore were able to reconstruct reasonably accurate times over the shorter outages by linearly interpolating the starting and ending times. As such interpolation would be quite inaccurate over long periods of GPS failure, travel-time data from the longer outages were not used.

The quality of waveform data from the temporary stations was variable. As the portable system requires AC electric power (a battery being present to cover short outages), stations had to be placed in settlements close to sources of anthropogenic noise. Some of this noise was reduced by band-pass filtering. WLSN proved to be the highest-quality station, rivalling the permanent stations in data quality. FSSN and FLSN were generally good, although intermittent anthropogenic noise was a problem. FPSN proved problematic due to frequent periods of noise, while LKSN operated for a shorter period than the others and so provided relatively few good events.

Little processing was required for the permanent stations, as the CNSN and Alaskan sites were quite carefully chosen, and had the benefit of permanent vaults and reliable timing, as well as the considerable skills of the site maintainers. The quality of data for these stations was generally very high, with some variation from station to station (figure 2.3).

In order to evaluate general data quality, event sections were plotted, with seismograms arranged by distance from the earthquake's epicenter; an example is shown in 2.4. For large

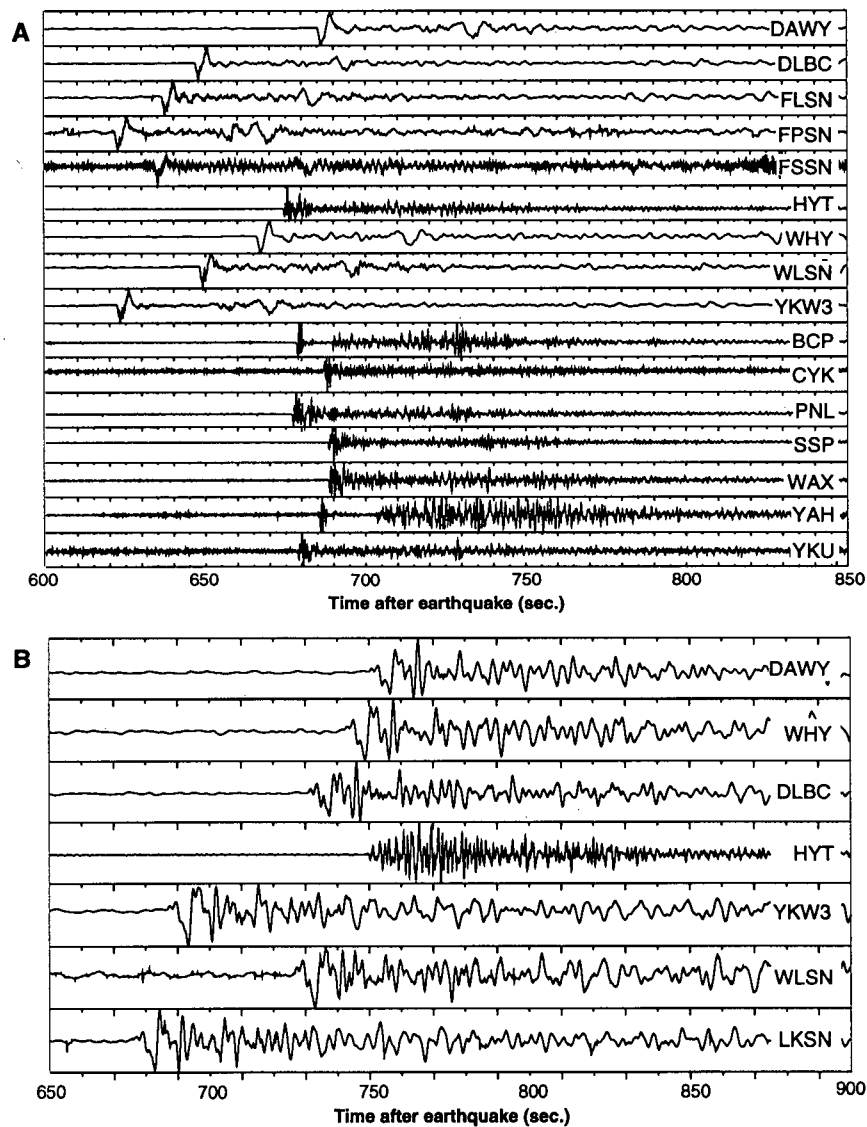


Figure 2.3: Waveform data for two events recorded by the array used in this study. Event A was a deep subduction event (Columbia, Aug. 19, 1995; 126 km depth); note the sharp P-wave arrival. Event B (Mid-Atlantic Ridge, June 2, 1996) was shallower (10 km) and displays a more highly oscillatory character. Note the difference between the broad-band and short-period responses. Before plotting, this data was band-pass filtered using corner frequencies at 0.05 Hz and 5 Hz.

events, multiple arrivals were recorded, including surface waves; this broad spectrum, along with the presence of three-component instruments, allows for the analysis of the entire three-dimensional waveform, although we concentrated on travel-time analysis for this study. For P-wave travel-time purposes, the longer-period waves were removed with a band-pass filter (usually with corner frequencies at 0.5 Hz and 5 Hz), leaving sharply-defined P-wave arrivals.

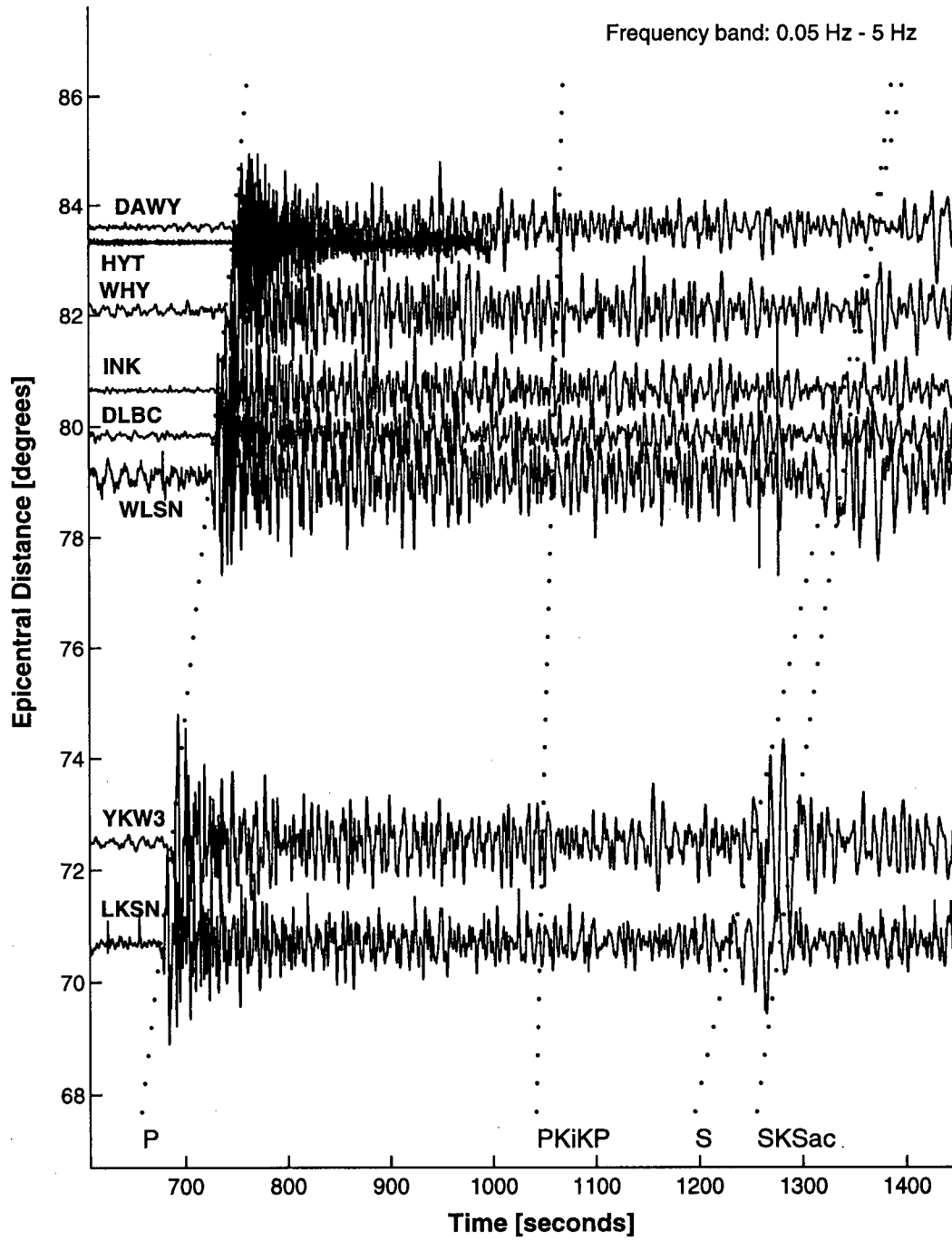


Figure 2.4: A sample event section (for the event in figure 2.3 B).

Chapter 3

Travel-time analysis

3.1 Rationale

Figure 3.1 is a cartoon illustrating the general configuration of a teleseismic tomography experiment. Two important considerations serve to simplify the analysis: the array is small compared to the distance to the source, and the first arrivals of P and S energy are always simple direct ray paths that bottom in the lower mantle. As a consequence, the rays for a given event follow almost identical paths for most of their length, diverging significantly only in the upper mantle on the receiver side. In addition, due to the large source-receiver separations and the relatively low velocities present in the crust, the ray paths are nearly vertical during their passage through the crust.

Suppose, then, that we represent the travel time from earthquake i to station j by the equation $t_{ij} = e_{ij} + m_{ij} + r_{ij}$, where e_{ij} is the component due to travel from the source to the point in the mid-mantle where the rays diverge, m_{ij} is the component due to travel in the upper mantle beneath the array, and r_{ij} is the component due to crustal travel below the stations. As the paths from the earthquake focus to the mantle beneath the array are nearly identical for a given event, we can assume that, to a good approximation, the travel-time components for the

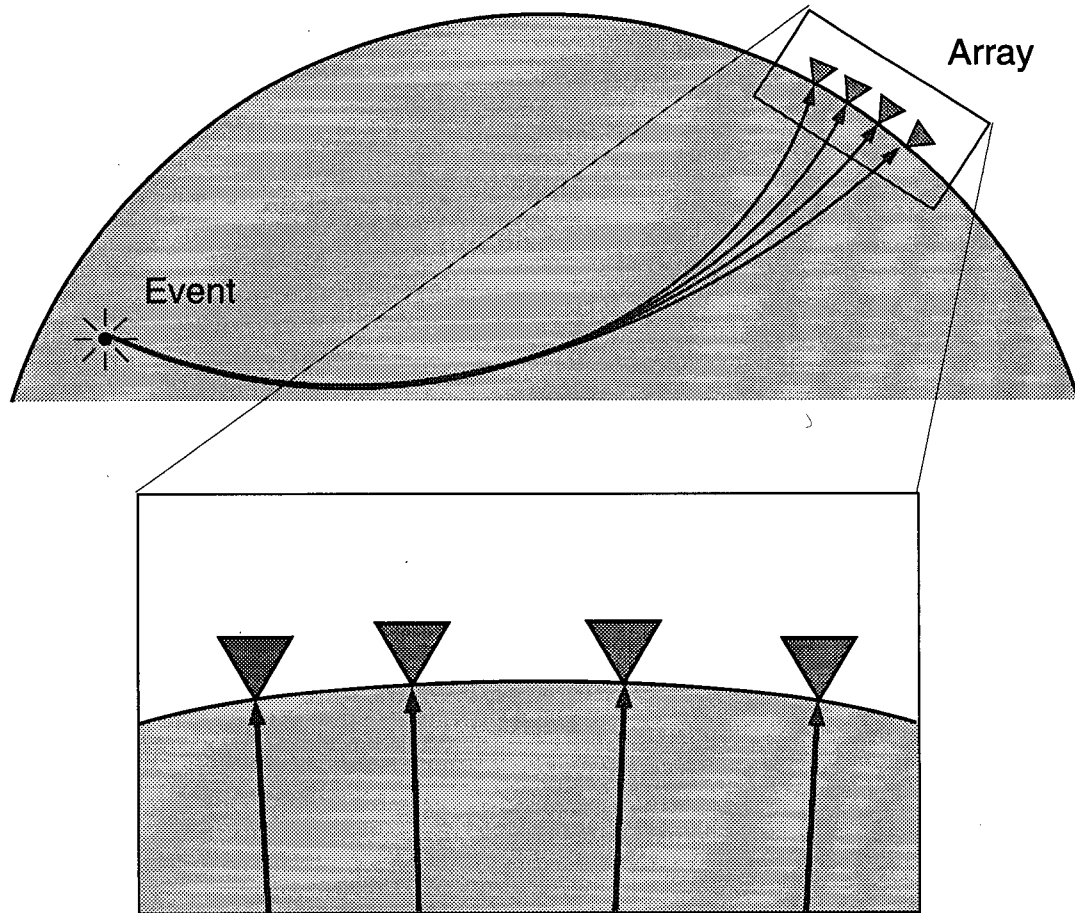


Figure 3.1: The ray paths for teleseismic events are nearly identical for all stations, except when close to the array. In the crust below the stations, the rays are almost vertical, and so nearly identical for all events. This is the justification for the use of static corrections to absorb effects from outside the model.

event are also identical, and so we can rewrite e_{ij} as e_i , a component depending only on the source. In a similar vein, the vertical nature of the crustal ray paths requires all the crustal ray paths beneath a given station to be nearly identical; therefore, to a good approximation, we can replace r_{ij} by r_j , which depends only on the station.

We have thus reduced our problem to one involving only tomography in the upper mantle beneath the array (as represented by the m_{ij} component) and simple event and receiver corrections (e_i and r_j , which are analogous to the static corrections used in the processing of seismic lines). If the static corrections can be correctly determined, the majority of remaining travel-time perturbations must be due to structure in the upper mantle beneath the array.

3.2 Determination of travel times

Accurate determination of the arrival time of an earthquake at a receiver is a more difficult problem than it would seem at first glance. The principal difficulty lies in ensuring that, between multiple seismograms, the equivalent point is consistently picked. This is eased in the teleseismic case by the consistency of the waveform between stations: as the teleseismic range contains no triplications, large phase shifts are unlikely. However, teleseismic events are generally low-frequency (averaging around 1 Hz for the P-wave), and so picking the same point on each seismogram is likely to give imprecise travel times, as well as being difficult to do when the signal-to-noise ratio is low.

It is therefore preferable to pick arrivals based on some measure of the correspondence of the first few cycles of the event on each seismogram. For the type of travel-time analysis we will perform, only relative travel times are required; that is, it is not necessary to pick the precise first arrival of energy on every seismogram, as long as the same point is chosen on each. The point chosen should, however, be early in the wave train, in order to avoid complications due to crustal multiples.

Consider two seismograms for the same event recorded at different stations, as shown in figure 3.2. The shift that best aligns the two seismograms is that which maximizes the cross-correlation between the two. This is superior to visual picking of maxima in that it is not highly dependent on high-frequency noise, and can easily be automated. However, as there are local minima at every alignment of peaks and troughs (particularly in narrow-bandwidth data, such as that from a short-period instrument), there is a considerable risk of cycle-skipping. Thus, using cross-correlation to improve the accuracy of visually-chosen picks was judged to be the appropriate technique to use (VanDecar and Crosson, 1990).

Cross-correlating more than two seismograms imposes an additional complication: the difficulty of reconciling the best shifts for different pairs of traces. In general, these maximum cross-correlation shifts will not be entirely consistent, and so some sort of best-fit approximation must be used. For this project, John VanDecar's *mccc* program was employed (VanDecar and Crosson, 1990). It calculates the maximum cross-correlation shifts in a window around the hand-chosen picks for every possible pair of seismograms. The result is the system of equations $\tau_j - \tau_i = \Delta\tau_{ij}$, where τ_i is the absolute time for the i th trace and $\Delta\tau_{ij}$ is the best shift computed from the cross-correlation of traces i and j . Adding the constraint that $\sum_{i=1}^n \tau_i = 0$ (to ensure that the system is completely determined), we have an overdetermined linear system of equations, small enough to be easily solved in a least-squares sense. The program performs this calculation, and then writes the resulting picks to an output file (VanDecar and Crosson, 1990; VanDecar, 1991).

The basic picking procedure employed is as follows: first, the traces are band-pass filtered, and predicted picks (calculated from the IASP91 model) are written to the data files. The hand picking is then performed (using Seismic Analysis Code [SAC] [Tapley and Tull, 1992]) and low signal-to-noise ratio traces are rejected. The multi-channel cross-correlation is then performed, and the resulting improved picks are plotted to check for cycle-skipping. The corner

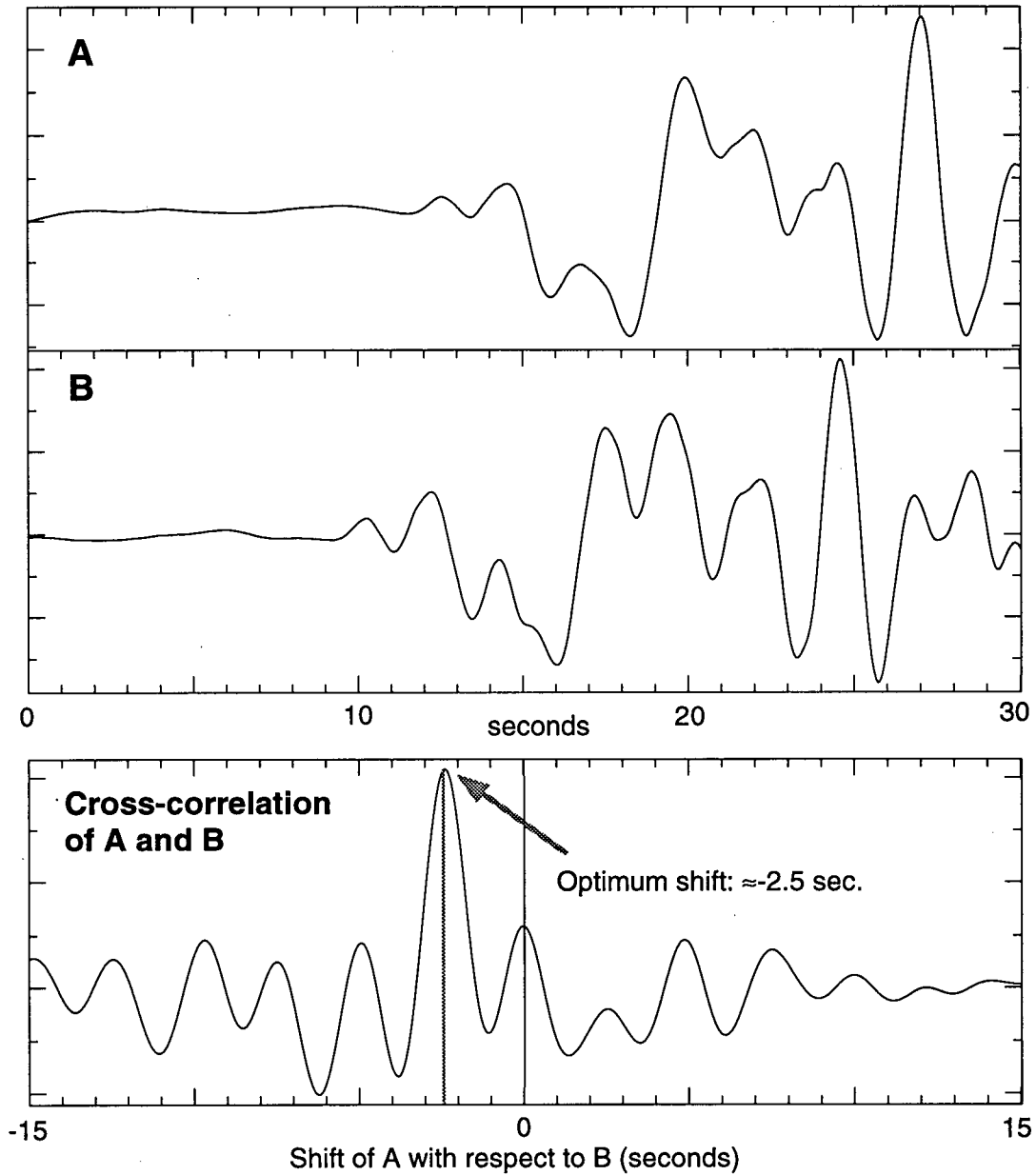


Figure 3.2: Seismograms A and B consist of the same event recorded at different stations. Their cross-correlation is plotted as a function of the offset applied to seismogram A. The shift that provides the largest positive cross-correlation between the two is clearly that which best aligns them; note, however, that there are local maxima corresponding to misalignments of multiples of the dominant wavelength.

frequencies employed vary from event to event; generally, the 0.5 Hz to 5.0 Hz band, covered by both short-period and broad-band instruments, is used, but some events require a wider band. Large earthquakes, unless occurring at great depth, generally appear highly oscillatory in the usual high-frequency band, causing the first arrival to be difficult to recognize; these events are therefore generally picked in a lower frequency band (0.05 Hz to 3.0 Hz). A consequence of this is that data from the short-period instruments can seldom be used for these large events.

3.3 The inverse problem

The forward problem of determining seismic travel times is formally expressed as

$$t_{ij} = \int_{\Gamma_{ij}} \frac{1}{v(\mathbf{r})} d\gamma$$

where t_{ij} is the travel time from source i to receiver j , Γ_{ij} is the ray path from source i to receiver j , and $v(\mathbf{r})$ is the seismic velocity function of the Earth (P- or S-wave as the case may be). If we introduce the *slowness* $s(\mathbf{r})$, defined by $s(\mathbf{r}) = \frac{1}{v(\mathbf{r})}$, the equation becomes the linear-looking

$$t_{ij} = \int_{\Gamma_{ij}} s(\mathbf{r}) d\gamma.$$

This equation is almost that of a linear problem; however, non-linearity enters through the ray path Γ_{ij} , which is dependent on the slowness function $s(\mathbf{r})$. Therefore, the inversion method used must be non-linear.

As a first step, we must decide how the model is to be described. For reasons explained in section 3.1, we need only consider that part of the upper mantle located immediately below the array, over a depth range between 100 and 900 kilometers. Within this region, we need a finite parameterization of the slowness function; the parameterization to use is determined by the nature of the data set. As all of the rays used are direct arrivals, with no reflections

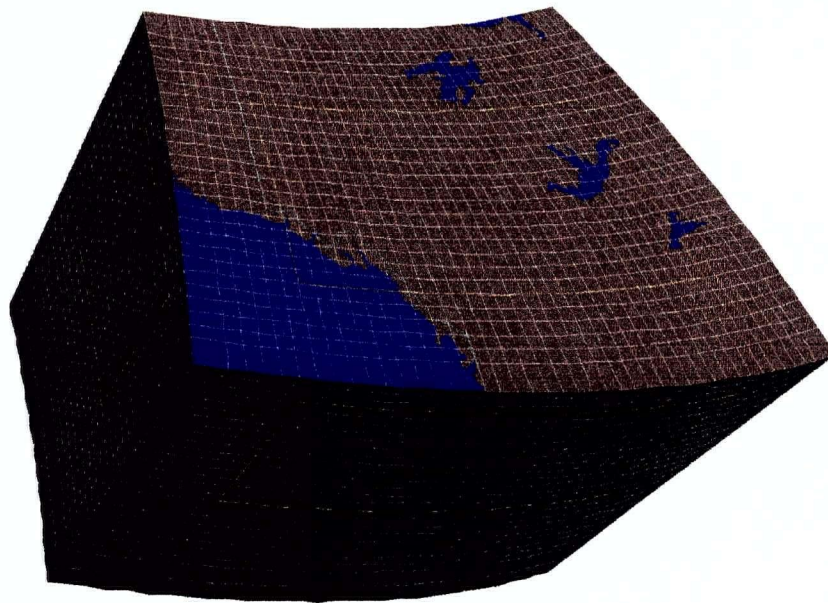
or refractions within the area of interest, we have no means of detecting sharp interfaces; in any event, including sharp changes in velocity in a tomographic inversion causes the inverse problem to be highly non-linear and unstable. Thus, it is best to represent the slowness as a smooth function; this will capture large-scale variations in the region of interest, although it will smooth out discontinuities (such as the phase transitions at 410 and 660 km depth). In addition, the model is best described in terms of perturbations around a standard Earth model; the IASP91 standard model (Kennett and Engdahl, 1991) was selected for this purpose.

The parameterization chosen, then, is that of a tensioned spline over a mesh of grid nodes (VanDecar, 1991). This provides a smooth, simple function given fixed values at the nodes. Figure 3.3 is a plot of the grid used for this experiment. The area covered by the model runs from 54°N to 68°N, and from 147°W to 103°W, extending vertically to 1400 km depth. This, as the figure demonstrates, means that the model extends in all directions considerably beyond the area in which we would expect to obtain good resolution. The presence of these extra nodes allows the model perturbations to be damped down to zero at the edges, as well as allowing anomalies to be placed outside the region of best expected resolution should that best fit the data (VanDecar, 1991). The nodes are spaced every half-degree in latitude, and every degree in longitude, the outermost nodes being spaced farther apart.

In addition to these true model parameters, we will invert for three additional parameter sets: static corrections for the stations and the events, and focus mislocations for the events. The reasons for the use of the first two are explained in section 3.1. The earthquake mislocations allow for errors in the foci and have the effect of removing travel-time trends across the array. The station locations are assumed to be accurate, and in the case of the portable stations, were measured using the data loggers' in-board GPS units.

The inverse problem then becomes the following: given the relative travel times of the events to the receivers, determine the seismic velocities of the grid nodes of a taut-spline model, along

Knot Locations for Taut Spline Parameterization



Number of knots in radius = 27; latitude = 27; longitude = 43

Total number of knots = 31347

Figure 3.3: A plot of the grid used for the travel-time inversion. The slowness function is fixed at the grid knots, where the grid lines intersect. The region outlined in yellow is that in which we expect to be able to resolve structure.

with static event and receiver corrections and a set of event mislocation vectors.

3.4 Linear inversion technique

A first attempt at solving a non-linear inverse problem may be made by finding an approximation of the non-linear problem as a linear problem; this is also a necessary step for most true non-linear inversion techniques. Recall from the previous section that our forward problem can be stated as

$$t_{ij} = \int_{\Gamma_{ij}} s(\mathbf{r}) d\gamma.$$

Suppose we know the predicted travel times and ray paths for a standard radial Earth model (e.g. IASP91 (Kennett and Engdahl, 1991), used in this study). If we represent the ray paths and slowness function for this model as Γ_{ij}^0 and $s^0(\mathbf{r})$, respectively, and express the true model as a perturbation around this starting model (i.e., $s(\mathbf{r}) = s^0(\mathbf{r}) + \delta s(\mathbf{r})$ and $\Gamma_{ij} = \Gamma_{ij}^0 + \delta\Gamma_{ij}$), then we can rewrite the forward problem as

$$t_{ij} = \int_{\Gamma_{ij}^0 + \delta\Gamma_{ij}} (s^0(\mathbf{r}) + \delta s(\mathbf{r})) d\gamma.$$

According to Fermat's principle, the true ray path is a stationary point of the travel time function. Therefore, assuming that the model perturbation $\delta s(\mathbf{r})$ is small, we can neglect the influence of the changed ray path on the travel time and make the first-order linear approximation

$$t_{ij} = \int_{\Gamma_{ij}^0} (s^0(\mathbf{r}) + \delta s(\mathbf{r})) d\gamma.$$

Expressing the travel times in terms of perturbations about the travel times predicted from the starting model (i.e. $t_{ij} = t_{ij}^0 + \delta t_{ij}$), the forward problem may be rewritten as

$$\delta t_{ij} = \int_{\Gamma_{ij}^0} \delta s(\mathbf{r}) dl.$$

This is the linear approximation of our non-linear problem. Its validity depends on the magnitude of $\delta s(\mathbf{r})$; as we do not expect our slowness perturbations to be more than a few percent of the IASP91 values, this is a reasonable first approximation. By updating the starting model through successive iterations of linear inversion, a full non-linear inversion may be achieved.

In order to solve the linear inverse problem stated above, we need to express it in matrix terms using the parameterization described in the previous section. The matrix expression of the above linearization, with no weighting or normalization included, is $\delta t = \mathbf{P}\delta s$, where δt is the vector of measured travel-time perturbations, δs is the vector of model parameters (values of the slowness function perturbation at grid nodes), and \mathbf{P} is the matrix of partial derivatives $P_{ij} = \left. \frac{\partial t_i}{\partial s_j} \right|_{s=s^0}$ (VanDecar, 1991).

Calculating this matrix of partial derivatives is the most computationally intensive part of the inversion procedure. Since we begin with a standard radial Earth model, the takeoff angles and azimuths of the desired rays are easily computed. The next step is to determine how each ray is affected by each grid knot. This is done by “shooting” a ray through the model; as the effect of each node is quite local in this parameterization, it can safely be assumed that each ray is affected only by nearby nodes. Given sets of nodes likely to be affected by each ray, and sets of straight line segments approximating each ray’s path, we can then slightly perturb each grid knot, recalculate the spline coefficients, integrate the perturbed slowness along the ray paths affected by the perturbed knot, and so calculate each partial derivative (VanDecar, 1991).

As our problem is highly underdetermined, and we will in any case not want to fit the data exactly (due to the existence of errors in the data), the next step is to select some form of regularization for our model. A minimum-structure solution has the advantage of favoring simple, easy-to-interpret models, as well as avoiding the introduction of spurious structure into the model. We therefore minimize the Laplacian of the model (using a finite-difference matrix) in order to obtain a smoothest-model solution; a component of flattening is also included in the

regularization matrix (VanDecar, 1991).

The final matrix to be inverted includes the travel-time equation, weighted by the errors in the data (as estimated by multi-channel cross-correlation), along with the regularization matrix and components to invert for the source and receiver corrections. It is very large, albeit sparse; sufficiently so that inverting it directly would require a prohibitive amount of available computer memory. Therefore, the matrix is inverted iteratively using a conjugate-gradient method (VanDecar, 1991).

As this inversion method finds a least-squares solution to its matrix equation, a few data points with large errors (such as cycle skips) can greatly influence the solution. One way of dealing with this would be to reject measurements with large misfits after performing a preliminary inversion. An alternative which does not require rejecting data is to downweight data points with large misfits, rather than simply rejecting them. After an inversion has been performed, outliers are downweighted to the equivalent of an L1 norm, as opposed to the L2 norm inherent in the least-squares procedure (VanDecar et al., 1995; Scales, 1988). This process is then repeated (from 12 to 20 times in this case), adding a level of iteration to the calculation that reduces the effect of outliers without rejecting data.

This linear inversion technique is iterated in order to perform a non-linear inversion. There are two techniques typically used for this purpose: the creeping method, where the regularization is applied to the model perturbation at each step, and the leaping method, where the entire model is regularized at each step. The leaping method, although not guaranteed to converge, tends to return a more regular model and so was used in this study (Parker, 1994; VanDecar, 1991).

The linear numerical problem at non-linear iteration k is expressed as

$$\begin{pmatrix} \mathbf{WP} & \mathbf{WR} & \mathbf{WE} \\ \mathbf{F} & 0 & 0 \end{pmatrix} \begin{pmatrix} \delta \mathbf{s}^{(k)} \\ \mathbf{r}^{(k)} \\ \mathbf{e}^{(k)} \end{pmatrix} = \begin{pmatrix} \mathbf{W} \delta \mathbf{t}^{(k-1)} \\ -\lambda \mathbf{F} \left(\sum_{i=0}^{k-1} \delta \mathbf{s}^{(i)} \right) \end{pmatrix}$$

where \mathbf{W} is a weighting matrix based on the estimated standard deviations of the data ($W_{ij} = \frac{\delta_{ij}}{\sigma_i}$), \mathbf{R} and \mathbf{E} are index matrices ($R_{ip} = 1$ if ray i was recorded at receiver p , $= 0$ otherwise; similarly, $E_{iq} = 1$ if ray i originated from event q), \mathbf{F} is the difference matrix for the regularization used (we use $\mathbf{F} = \lambda_f \mathbf{F}_f + \lambda_s \mathbf{F}_s$, where f denotes flattening and s denotes smoothing; the λ s are weights applied to each form of regularization), and \mathbf{P} is the matrix of partial derivatives. The vectors to solve for are $\delta \mathbf{s}^{(k)}$, the slowness model for iteration k ; $\mathbf{r}^{(k)}$, the receiver corrections for iteration k ; and $\mathbf{e}^{(k)}$, the event corrections for iteration k . The right-hand side of the equation contains the data $\delta \mathbf{t}^{(k-1)}$ (the travel-time residuals corresponding to the previous model) and a summation term using all of the previous slowness models (to ensure that the entire model, not just the new perturbation, is regularized). Solving this equation is the innermost step in this three-level procedure (VanDecar, 1991).

Each non-linear iteration consists of an entire linear inversion, with the model from the previous iteration used as the reference model. As the reference model is no longer radial, an additional step is required: the 3-D ray tracing needed to find the correct launch angle and launch azimuth for each ray prior to calculating the partial derivatives. This is done using a shooting method (VanDecar, 1991).

Chapter 4

Results

4.1 Residuals

Before inverting travel-time data, it is useful to determine what conclusions can be drawn from arrival times; this can provide clues as to where to look for structure as well as providing a useful check for models generated by inversion. The relative travel time t_{ij} of event i to station j may be decomposed into $t_{ij} = t_{ij}^I + \delta t_{ij}$, where t_{ij}^I is the relative travel time as predicted by the IASP91 standard earth model, and δt_{ij} is the travel-time perturbation unaccounted for by the standard model. In order to account for crustal effects beneath the stations, we can further decompose the travel-time perturbation using the equation $\delta t_{ij} = \delta t_j^S + \delta \hat{t}_{ij}$, where δt_j^S is the average travel-time perturbation to station j , the averaging being performed over all the recorded events. The remaining perturbation $\delta \hat{t}_{ij}$ is then approximately that component of the travel-time which the inversion maps into the upper mantle.

A simple method for examining these data is to plot the travel-time residuals for a single event on a map. This can be quite valuable in experiments where the stations are finely spaced; however, due to the relatively small number of stations used in this experiment, the conclusions we can draw from such maps are limited. Figures 4.1 and 4.2 give examples of such maps for

events arriving from widely varying back azimuths, the first figure being a plot of δt_{ij} and the second being $\delta \hat{t}_{ij}$. There is a consistent pattern of westwardly-increasing delays in figure 4.1, much of which probably reflects the the younger mantle and crust of the Cordillera relative to the craton. The patterns in figure 4.2, which are more likely to reflect mantle structure, are far less systematic, and it is difficult to draw specific conclusions from them before inverting.

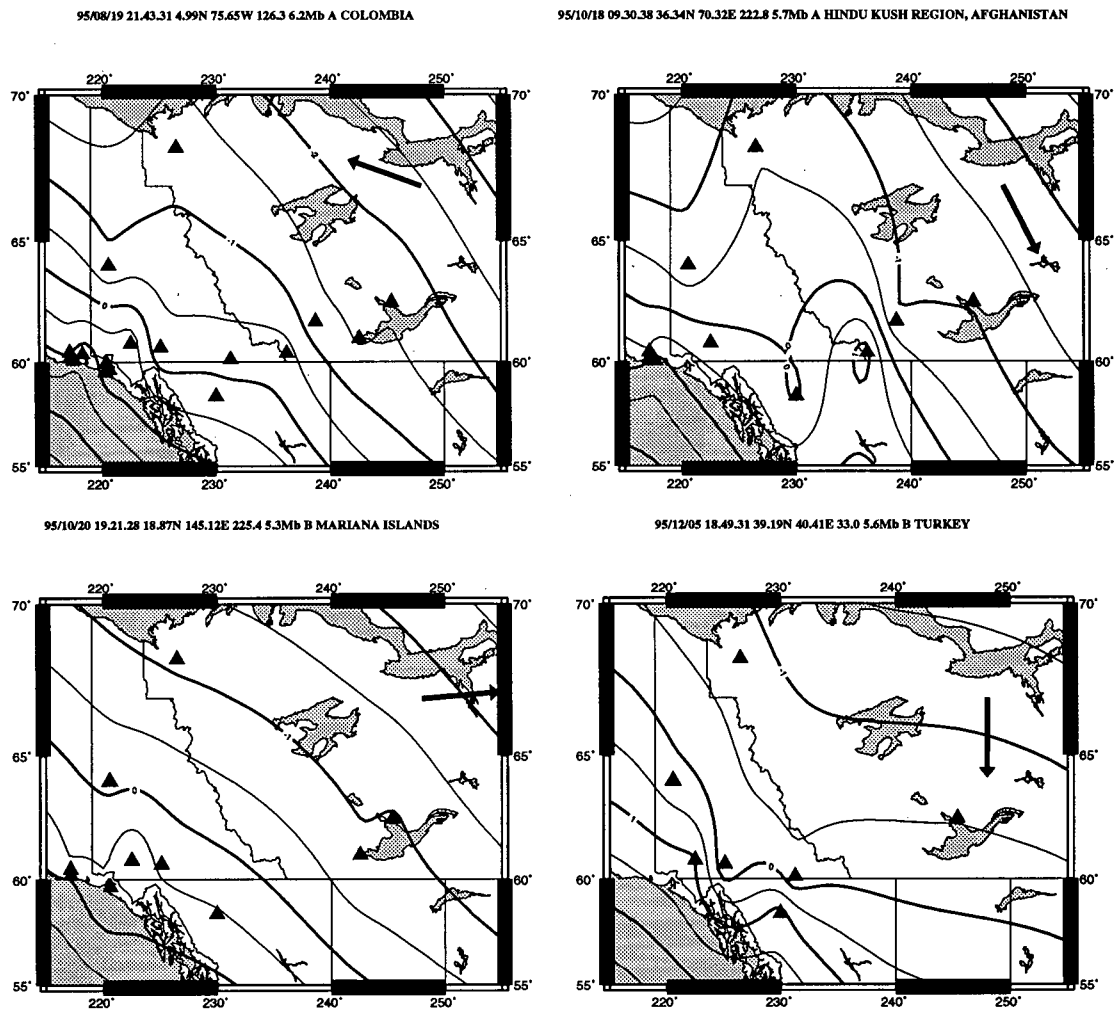


Figure 4.1: Some sample contour maps of travel-time perturbations for individual events. The arrow indicates the direction of propagation of the wavefront; the contour interval is 0.5 s.

It is perhaps more instructive to gather the perturbations by station rather than by event,

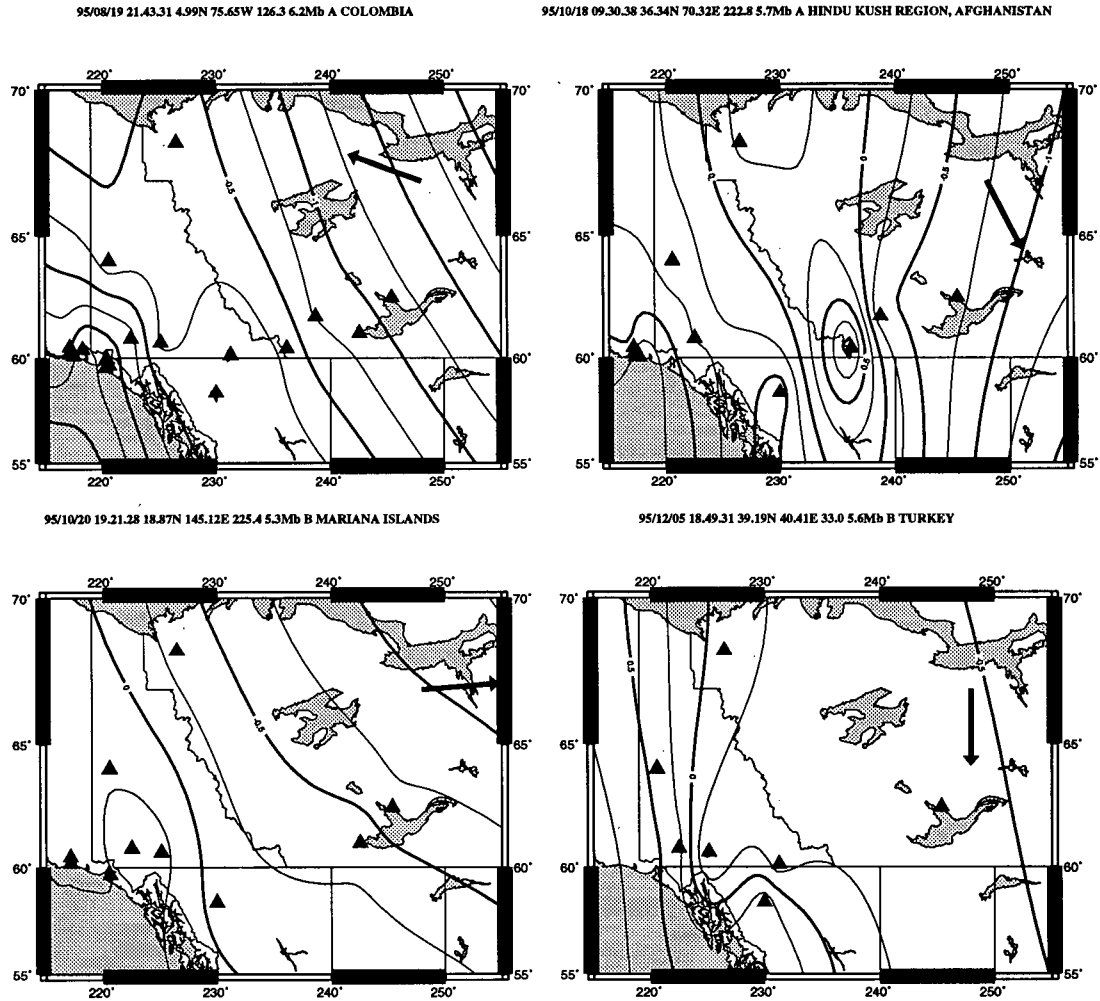


Figure 4.2: Contour maps of travel-time perturbations after the station averages have been removed. The events shown are the same as in the previous figure; the contour interval is 0.25

s.

as there can be at most 17 data points per event, as compared to a possible 385 data points per station. Unfortunately, the perturbations for different events to the same station are not directly comparable; although the averaging to zero performed by using only relative arrival times eliminates any static event bias, it also biases data points differently depending on which particular set of stations recorded each event. Consequently, the variations in travel-time perturbations to a given station between different events are only reflective of structure to the extent that the sets of stations recording the events were consistent. However, if we assume that this variation in the station set from event to event was largely independent of the location of the events, then we can suppose that the effect of the variation will only be to introduce scatter into the pattern of perturbations, and not to introduce spurious directional variations.

With this in mind, the travel-time perturbations (after removal of the station average) for each station were plotted against the back azimuth and epicentral distance of the event (figure 4.3). This is somewhat analogous to the event-side technique of plotting residual spheres (Creager and Jordan, 1984). Not all of these plots display obvious structure; stations with relatively few events (e.g. LKSN and the Alaskan stations) were omitted. On the plots shown, the main conclusions that may be drawn are directional. For instance, on the DAWY plot, we can state that there are regions of fast mantle to the northwest and southeast, and a slow region to the southwest; the plot for station WHY suggests a substantial fast region to the north. This is consistent with the inversion results (see below).

4.2 Choice of inversion parameters

In an inversion of this type, the choice of regularization parameters is crucial. Figure 4.4 demonstrates how the nature of the model varies depending on the choice of smoothing parameters; the most notable effect is the change in amplitude of the recovered anomalies, but there is also a considerable effect on the amount of structural detail recovered. The problem of choosing the

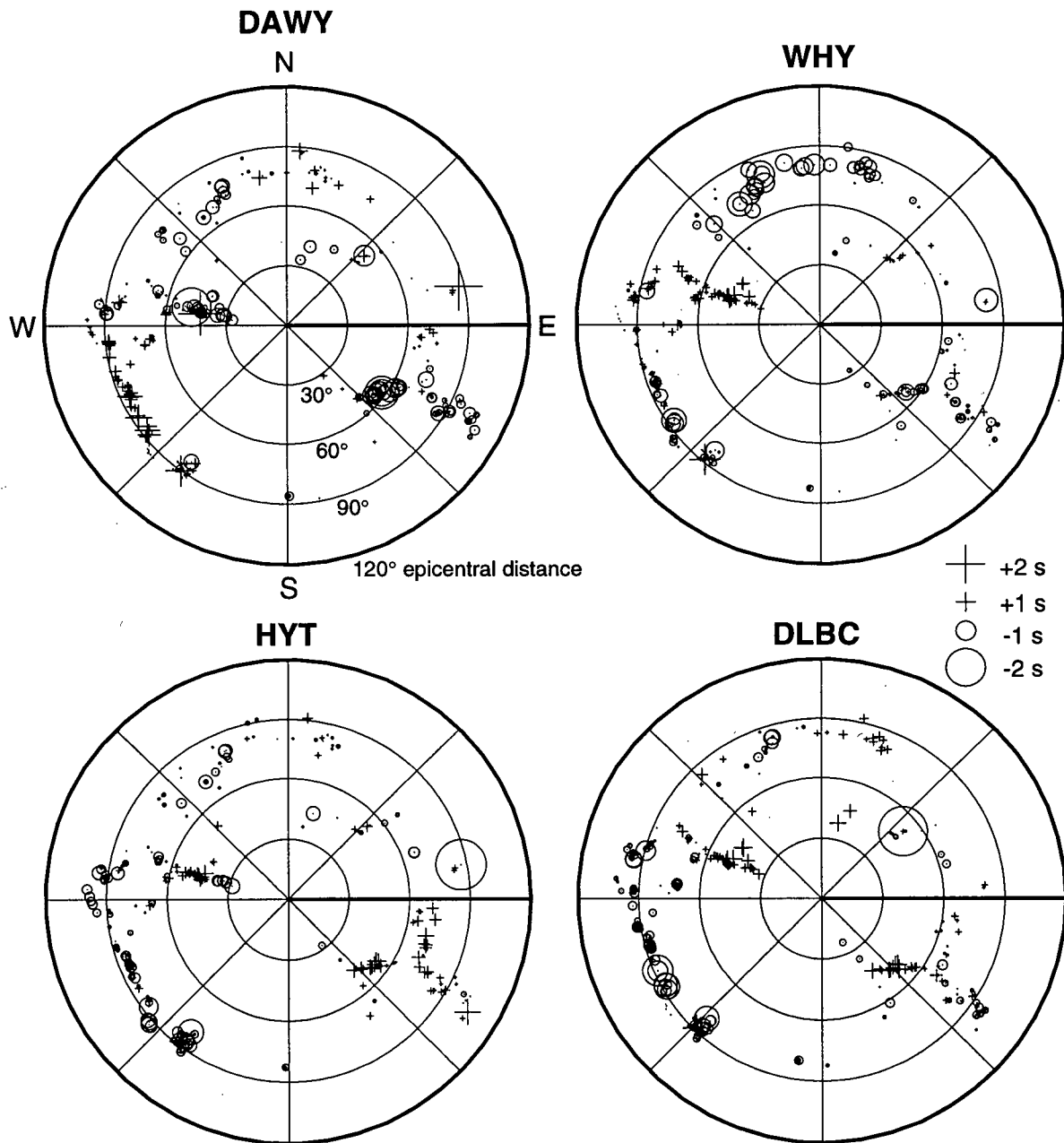


Figure 4.3: Sample plots of station-gathered corrected travel-time perturbations, on a radial projection. Crosses represent positive travel-time perturbations (slow arrivals) while circles represent negative perturbations (fast arrivals).

best regularization amounts to adjudicating a tradeoff between fitting the data and simplifying the model, quantified as a relationship between the travel-time misfit and the model norm. In our case, there are two regularization weights to be used, a smoothing weight (minimizing model roughness) and a flattening weight (minimizing model gradients). The relative weight of these two regularizations is chosen based on the desired form of the recovered model; as we desire a minimum-structure solution, the flattening weight is held to $\frac{1}{50}$ of the smoothing weight.

The misfit-norm relationship for a linear inversion may be plotted as a tradeoff curve. Two such curves are shown in figure 4.5, for the first and second linear iterations. Choosing the correct point on a tradeoff curve can be done using knowledge of the standard error of the data, which should correspond to the target root-mean-square misfit. If the standard errors of the data are not well known, the optimum regularization may be picked by its proximity to the point of maximum curvature of the tradeoff curve (Parker, 1994). Due to both the presence of non-Gaussian outliers in the data and our uncertain knowledge of the measurement error, the standard error of the data is somewhat uncertain; therefore, the latter method was used to find optimum models for both iterations. In order to ease ray tracing for the non-linear step of the inversion, a somewhat smoother than optimum model from the first iteration was used as the starting point for the second.

One problem in non-linear inversion is knowing when to stop iterating. The number of non-linear iterations required for convergence depends on the degree of non-linearity of the problem, and, due to the computationally-intensive nature of non-linear inversion, it is wasteful to pursue the inversion further than necessary. In figure 4.6, equivalent models from the first and second iterations are shown. The differences between the two are quite minor, much of the difference being due to the slight difference in regularization between the two models. An exception is the strong negative slowness anomaly at the extreme east of the first model; however, as shall be shown in the next section, this feature lies in a region where the model resolution is very poor.

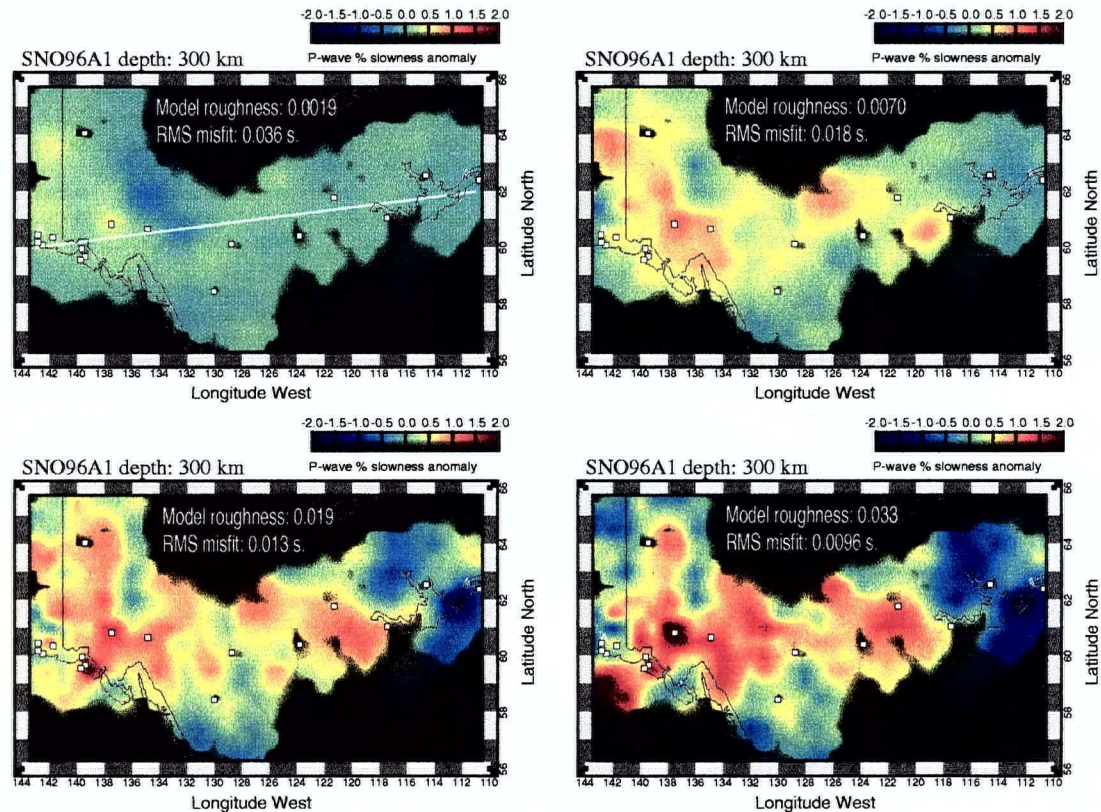


Figure 4.4: An example of the effect of varying the weight given to smoothing in the linear inversion. These otherwise identical horizontal sections through the first-iteration model show the effect of smoothing weights ranging from 50000 (upper left corner) to 5000 (lower right), ranging from a severe underfit to a severe overfit of the data. The chosen fit lies between the values used for the second and third plots. The inversions used 12 downweighting iterations apiece; black areas are those without good ray coverage (i.e. no sampling rays).

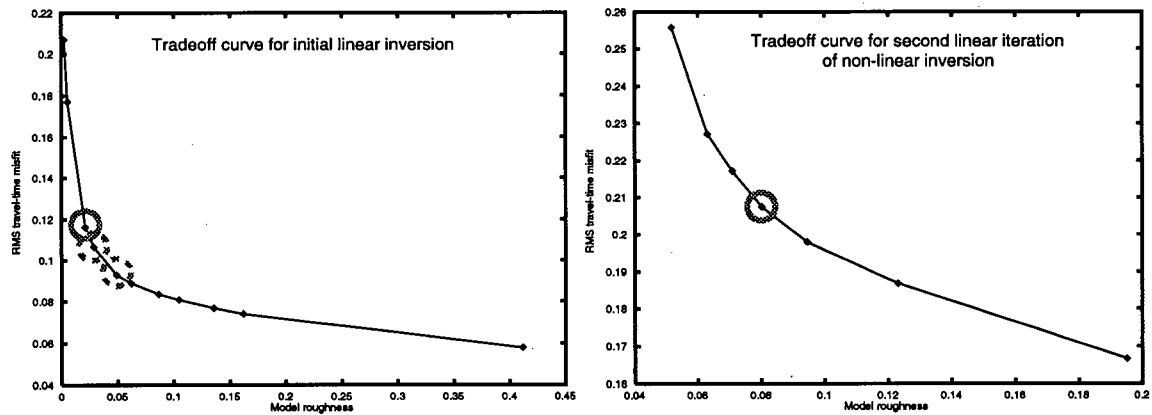


Figure 4.5: Tradeoff curves for the two linear iterations performed. The root-mean-square travel-time misfit is plotted against the model roughness (the integrated Laplacian of the model). The values used here were calculated without any downweighting of outliers, so the magnitudes of the misfits are exaggerated. The optimal model for the initial inversion (left) lies between the two points in dashed circles; however, to ease ray tracing, a somewhat smoother model was used as a starting model for the next iteration (solid circle). The optimum model from the second iteration (circled, right) was used as the final model.

Considering the minor nature of the differences between the first-iteration and second-iteration models, we decided to stop the inversion after two iterations of linear inversion.

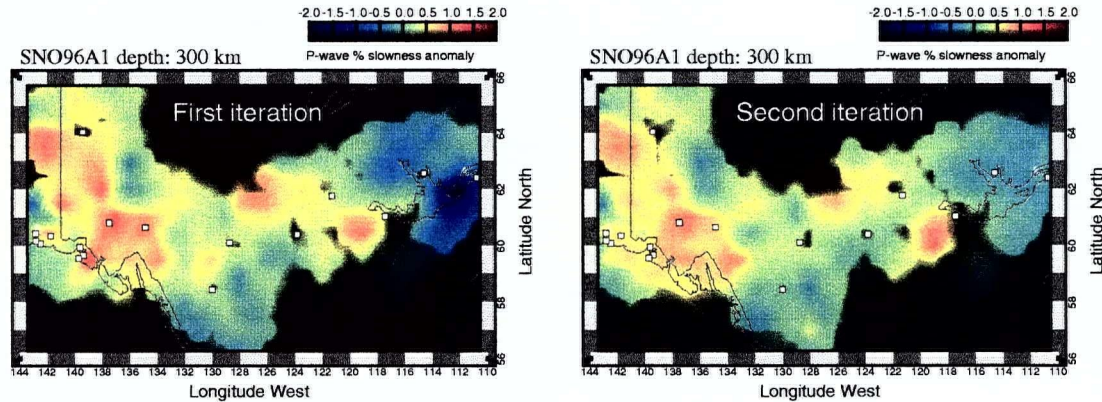


Figure 4.6: Horizontal sections for models with approximately optimal regularizations from the first (left) and second (right) linear iterations. Note that the regularizations are not exactly equivalent; the left-hand model was slightly less heavily regularized, which may account for differences in amplitude. Remaining differences between the two can largely be attributed to non-linearity.

4.3 Resolution

Calculating the resolution matrix for a linear inverse problem requires a singular-value decomposition of the matrix of partial derivatives. This is not possible in this case because the matrix is prohibitively large (VanDecar, 1991). Therefore, in order to evaluate the resolving power of this type of experiment, it is necessary to perform a resolution test. The way this is done is simple: a synthetic model is generated, the data that such a model would produce are calculated, these synthetic data are inverted, and the recovered model is compared to the input model. We performed only linear inversions of the synthetic data; therefore, the forward modeling amounted simply to a multiplication of the IASP91 model's partial derivatives matrix by the model vector

($\delta t = \mathbf{P}\delta\mathbf{s}$; see section 3.4), a very quick process involving no ray-tracing. Gaussian noise with a standard deviation of 0.015 second (approximating the estimated standard error of the real data after the downweighting of outliers) was added to the synthetic data; due to the Gaussian nature of this noise, it was unnecessary to perform any downweighting of outliers, and so the inversion process took only about forty minutes of CPU time on a Sun SPARC 10.

Two such tests were performed. The first test (figures 4.7 and 4.8) involved the recovery of a single large spike anomaly, in order to examine how the anomaly was deformed by the inversion given the available ray set. The most notable effect of the inversion is the reduction in amplitude of the anomaly; this is hardly surprising, as the smooth-model inversion used strongly penalizes spikes and tends to smooth out sharp changes in slowness. In addition to this reduction in amplitude, there is some downward and westward smearing of the anomaly; this reflects the paths of the rays intersecting the anomaly. Overall, however, this large anomaly was quite well recovered.

The second, more detailed resolution test involved a three-dimensional checkerboard of evenly-spaced positive and negative anomalies (figures 4.9 through 4.12). This type of test evaluates the ability of the experiment to resolve small anomalies, as well as locating areas of good and bad resolution in the model, and so determining which areas in the model can safely be interpreted.

We drew four main conclusions from the checkerboard resolution test. First, the resolution falls off quite rapidly to the east, particularly at shallower depths. In particular, resolution east of 122°W is very poor, except at great depth. Therefore, that part of the model that lies east of 122° will not be interpreted. Second, the magnitude of the anomalies was greatly underestimated. This is probably a consequence of the spike-like nature of the anomalies, as discussed previously for the large-spike test. As well, the peaks of the anomalies could only be sampled by a ray passing directly through their centers. For smoother structures, the magnitude

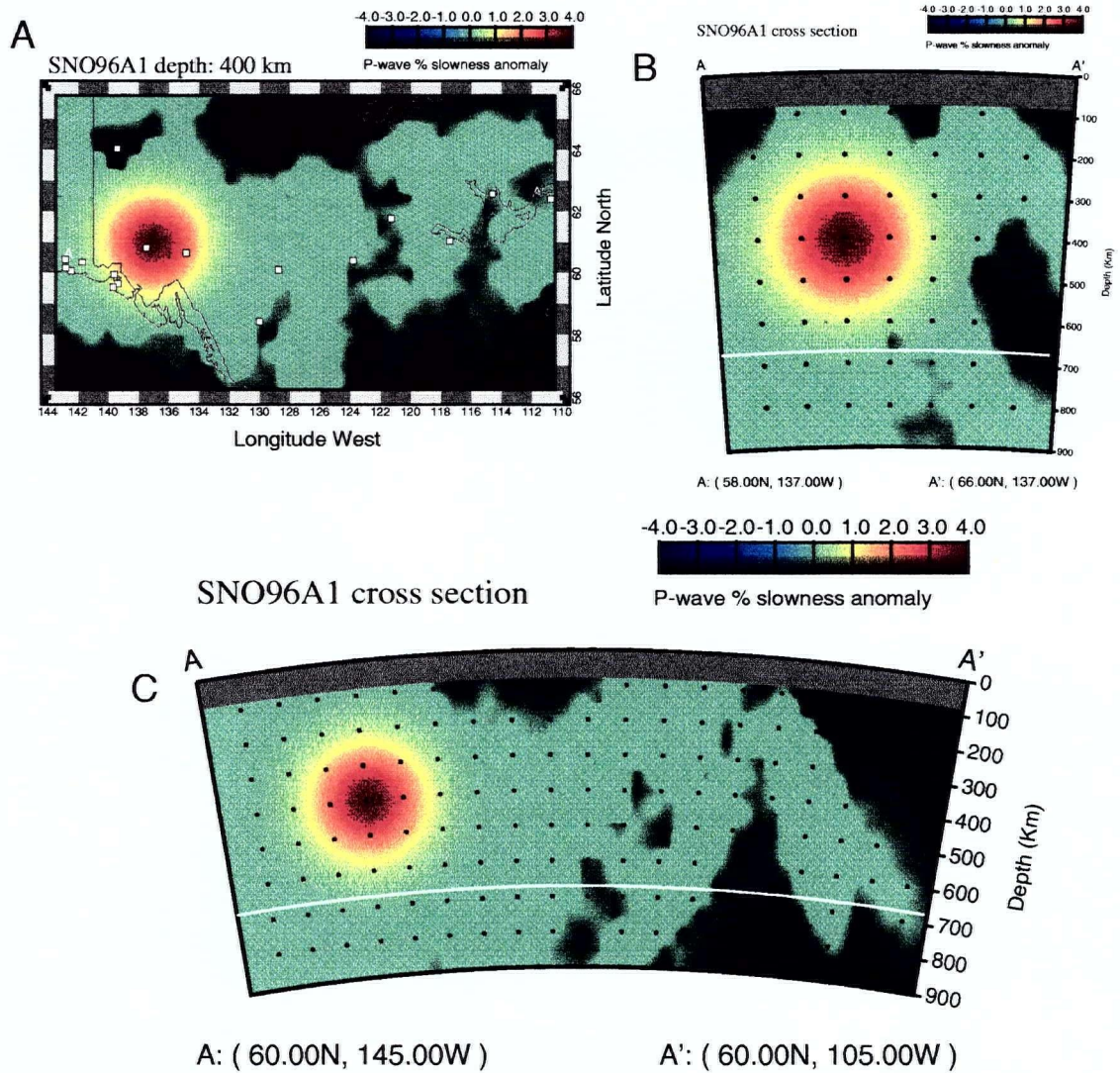


Figure 4.7: Three sections through the synthetic model used for the large-spike resolution test. The plots are: A) a horizontal section at 400 km depth, B) a vertical section oriented N-S along the 137° meridian, and C) a vertical section along an approximately E-W great circle intersecting the anomaly. Areas shaded black were not sampled by more than one ray and therefore cannot be resolved by the inversion.

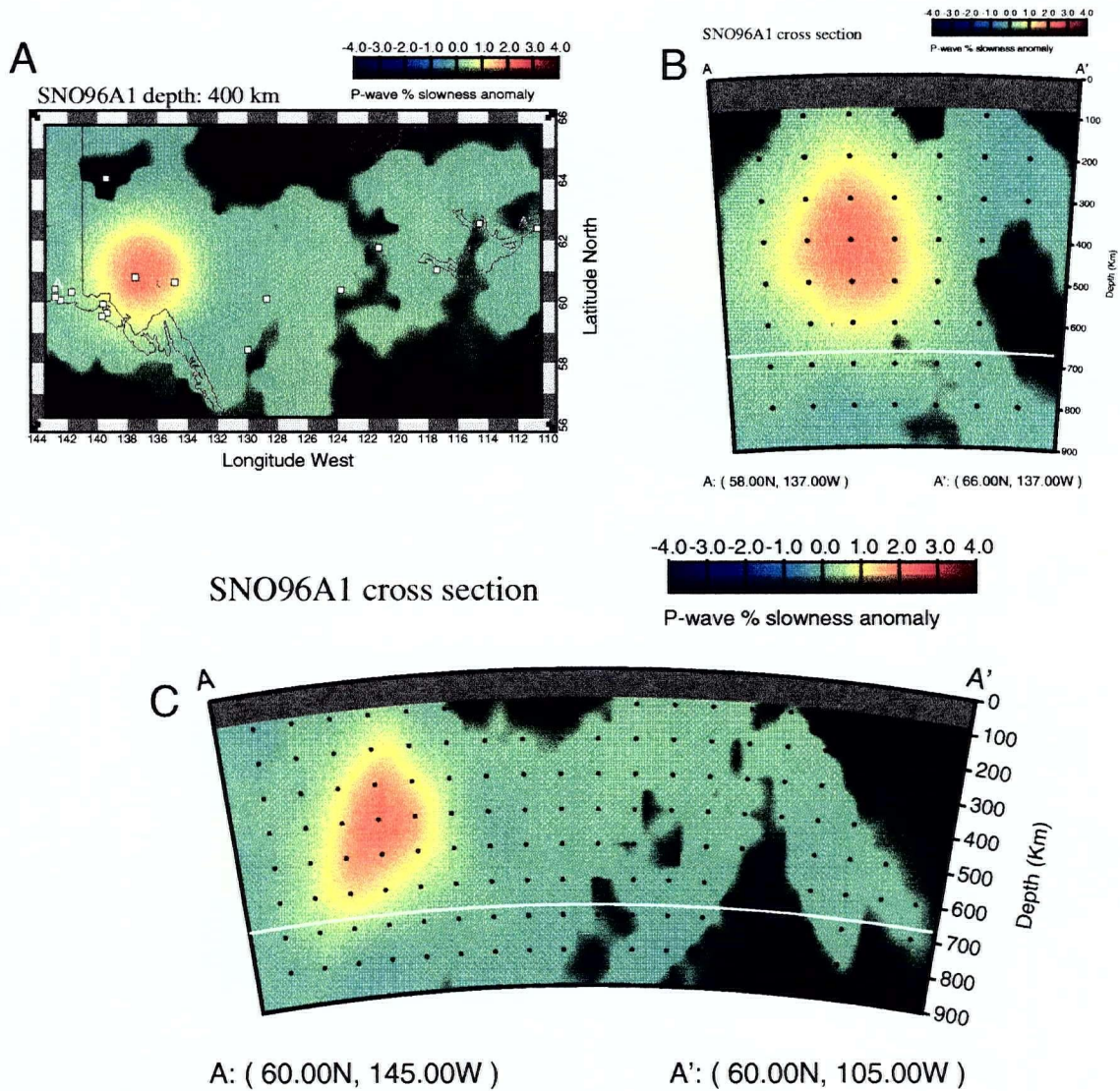


Figure 4.8: Three sections through the recovered model from the large-spike resolution test. The sections correspond to those in the previous figure, and the color scale is the same.

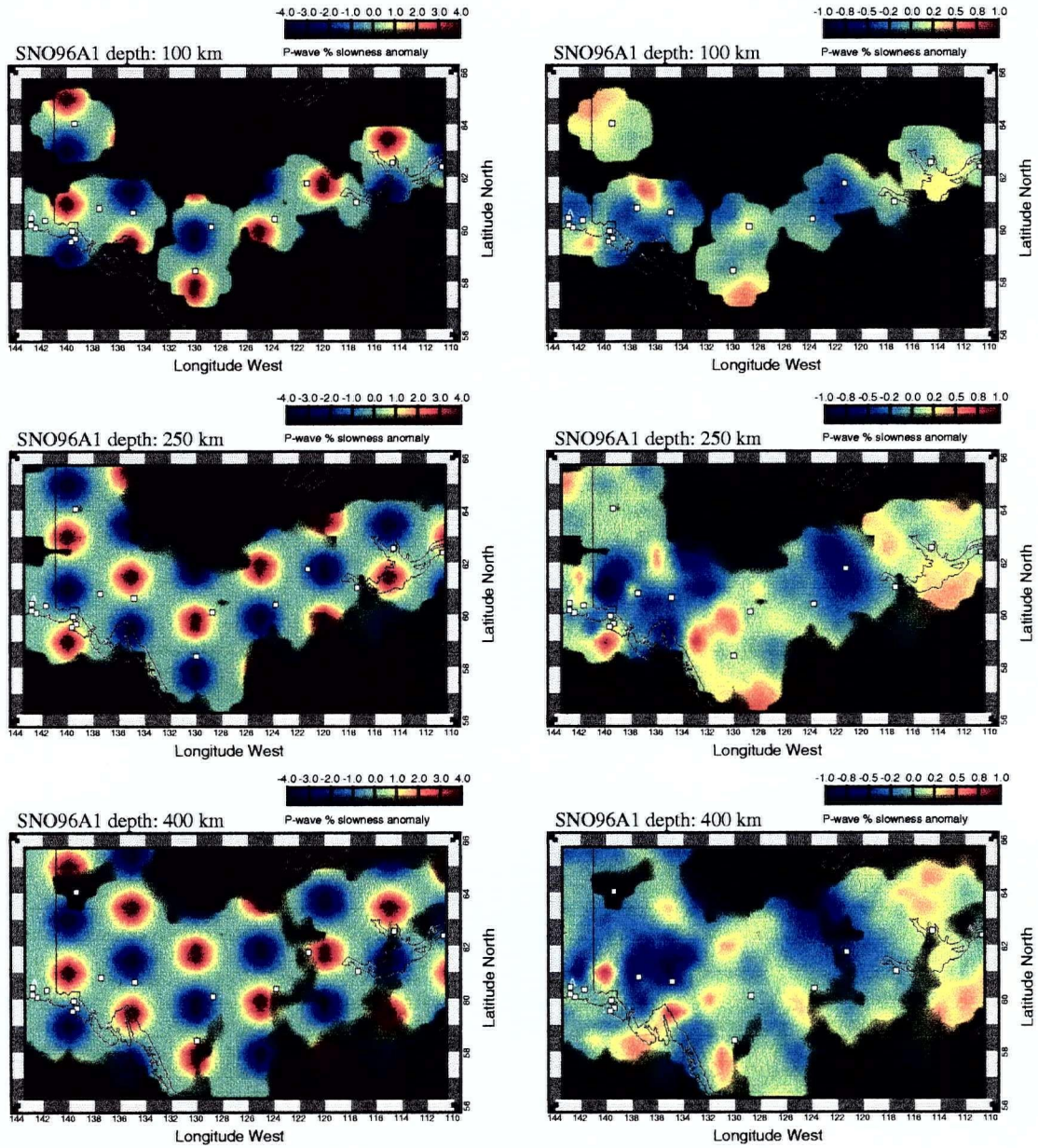


Figure 4.9: Horizontal sections through the input (left) and recovered (right) models from the checkerboard resolution test. Note the difference in color scales between the input and recovered models.

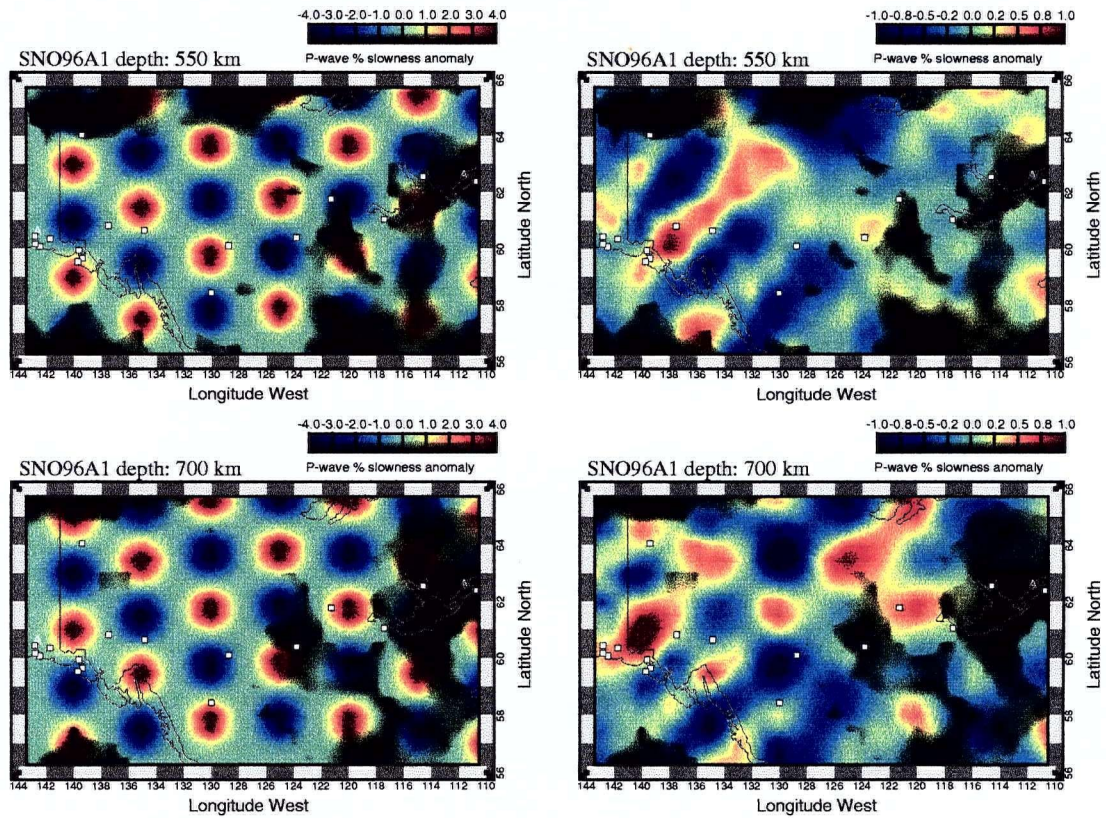


Figure 4.10: Deeper horizontal sections from the checkerboard resolution test. (See the previous figure for details.)

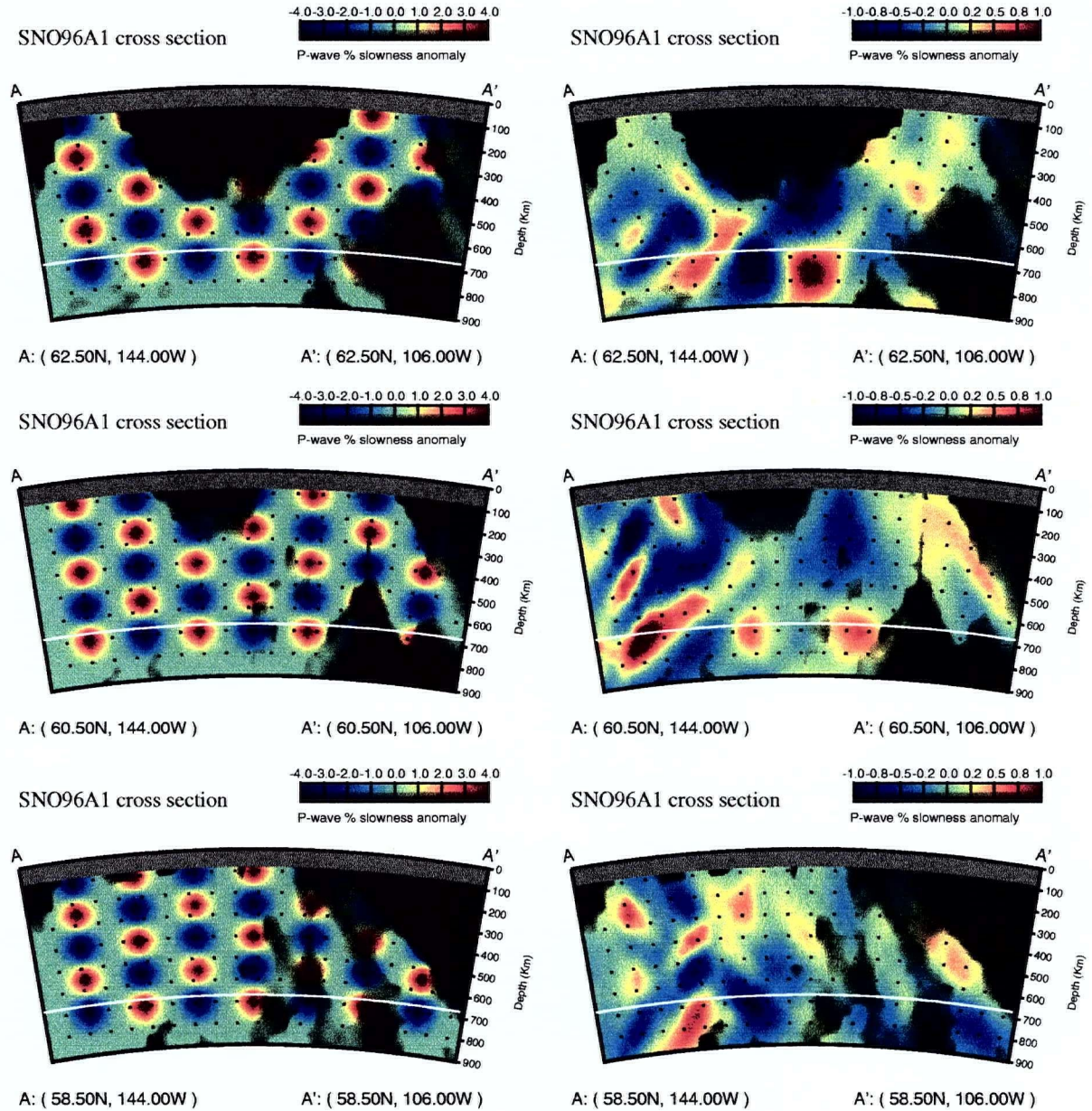


Figure 4.11: East-west oriented vertical sections through the input (left) and recovered (right) models from the checkerboard resolution test. The slices correspond to the middle three rows of anomalies in the checkerboard. The sections are stacked from northernmost to southernmost.

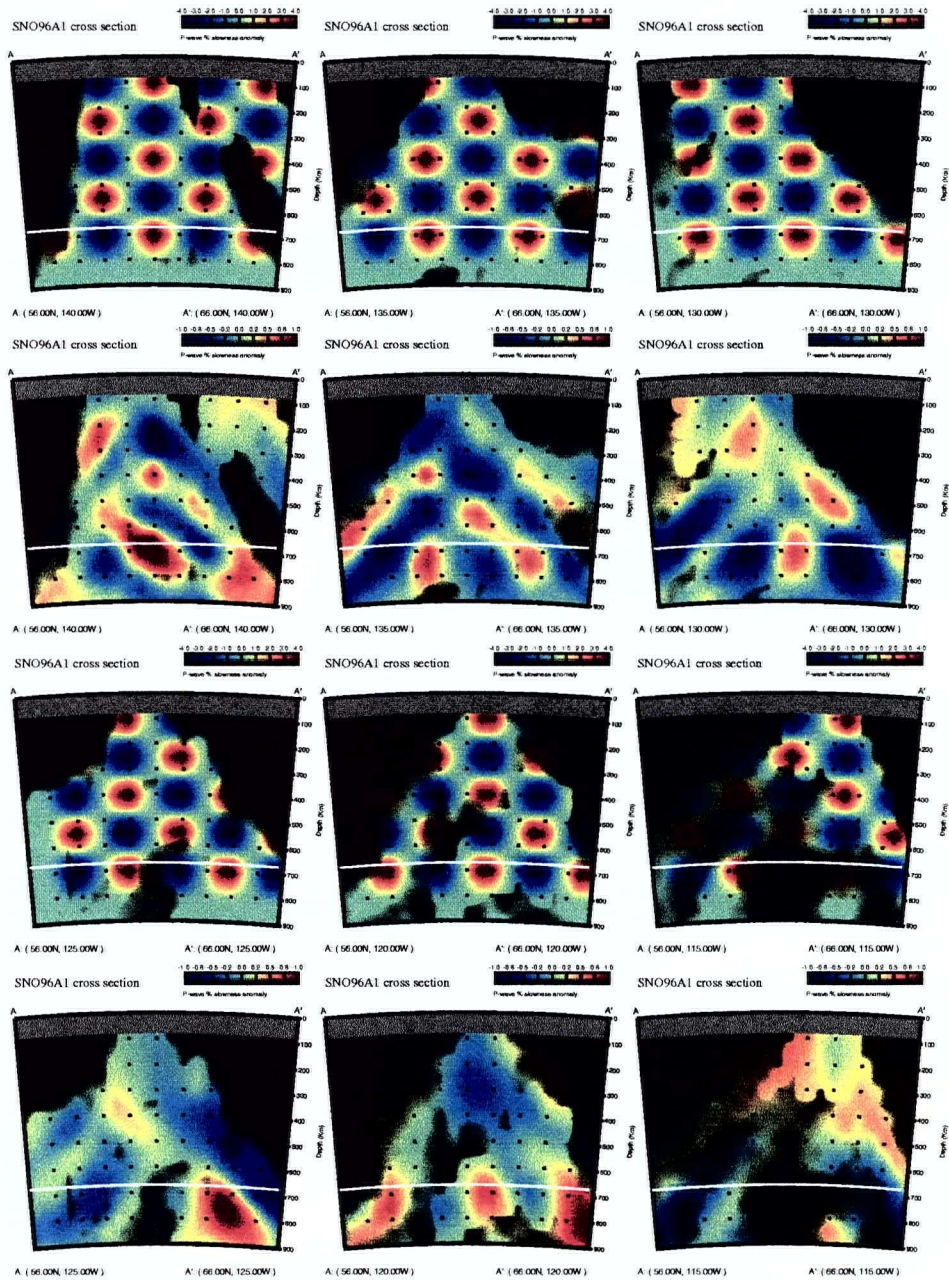


Figure 4.12: North-south oriented vertical sections through the input (first and third rows) and output (second and fourth rows) models from the checkerboard resolution test. The sections are arranged from westernmost (upper left corner) to easternmost (lower right); each slice is oriented with south at the left.

of anomalies is likely to be better measured; however, we can expect some underestimation. The uppermost part of the model shows the greatest tendency for underestimation and poor resolution, probably as the consequence of structure being absorbed into the station corrections and the absence of ray crossings at shallow depths.

Third, the resolution varies strongly with depth. The uppermost layer of anomalies was largely missed; in the deeper layers, there is considerable downward smearing. The best depth and lateral resolution seems to lie between 200 and 600 kilometers depth, in the western half the model; in that region, anomalies of about 150 km in all directions may be detected.

Finally, there is considerable smearing of the anomalies along lines plunging southwestward. This reflects the uneven distribution of events in the data set (see figure 2.2), and we can probably expect similar smearing to occur in the model recovered from real data. The smearing is greatest below 500 km.

In summary, we can expect reasonable recovery of structure below 200 km west of 122°W . Structure above 200 km may be missed and will probably be underestimated. We can expect structure below 500 km to be smeared somewhat southwestward. However, with all this in mind, we can interpret large-scale structure with a fair degree of confidence.

4.4 Observed features

Figures 4.13 through 4.16 present the final model we have selected. It is the result of two iterations of linear inversion, each consisting of 20 downweighting iterations around 2000 conjugate-gradient iterations; the regularization parameters used correspond to the points marked on figure 4.5. The total execution time for the inversion was about 150 hours on a Sun Sparc 10 computer. The station static corrections are shown on the horizontal model slices (figures 4.13 and 4.14); the event static corrections are shown in figure 4.17.

Before examining the structures located by the inversion, it is useful to examine the station

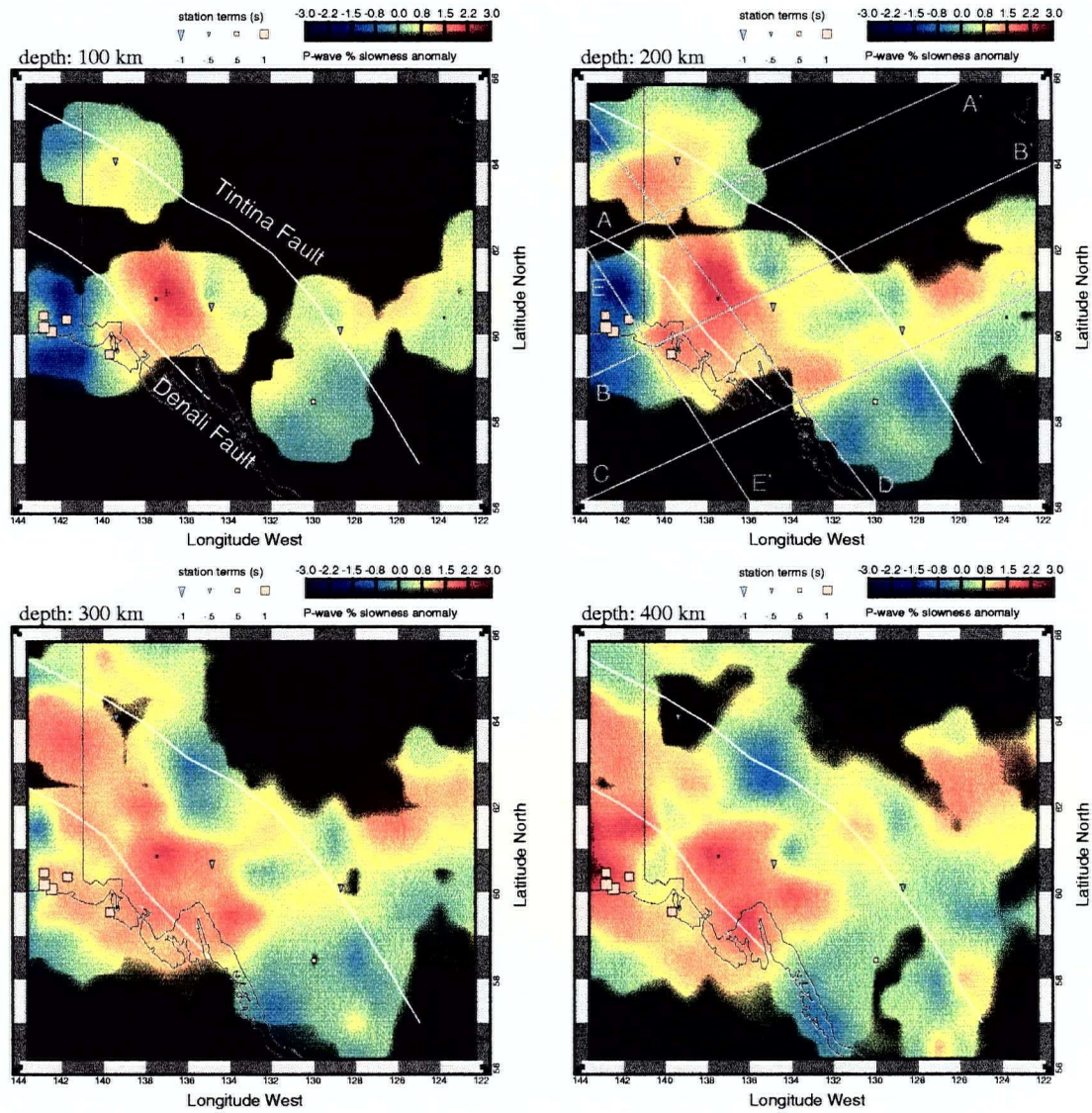


Figure 4.13: Horizontal cross-sections through the final tomographic model. The locations of the Tintina and Denali faults are marked in white; the cross-sections plotted in figures 4.15 and 4.16 are shown in grey on the 200 km section. Station statics are shown as triangles (negative) and squares (positive).

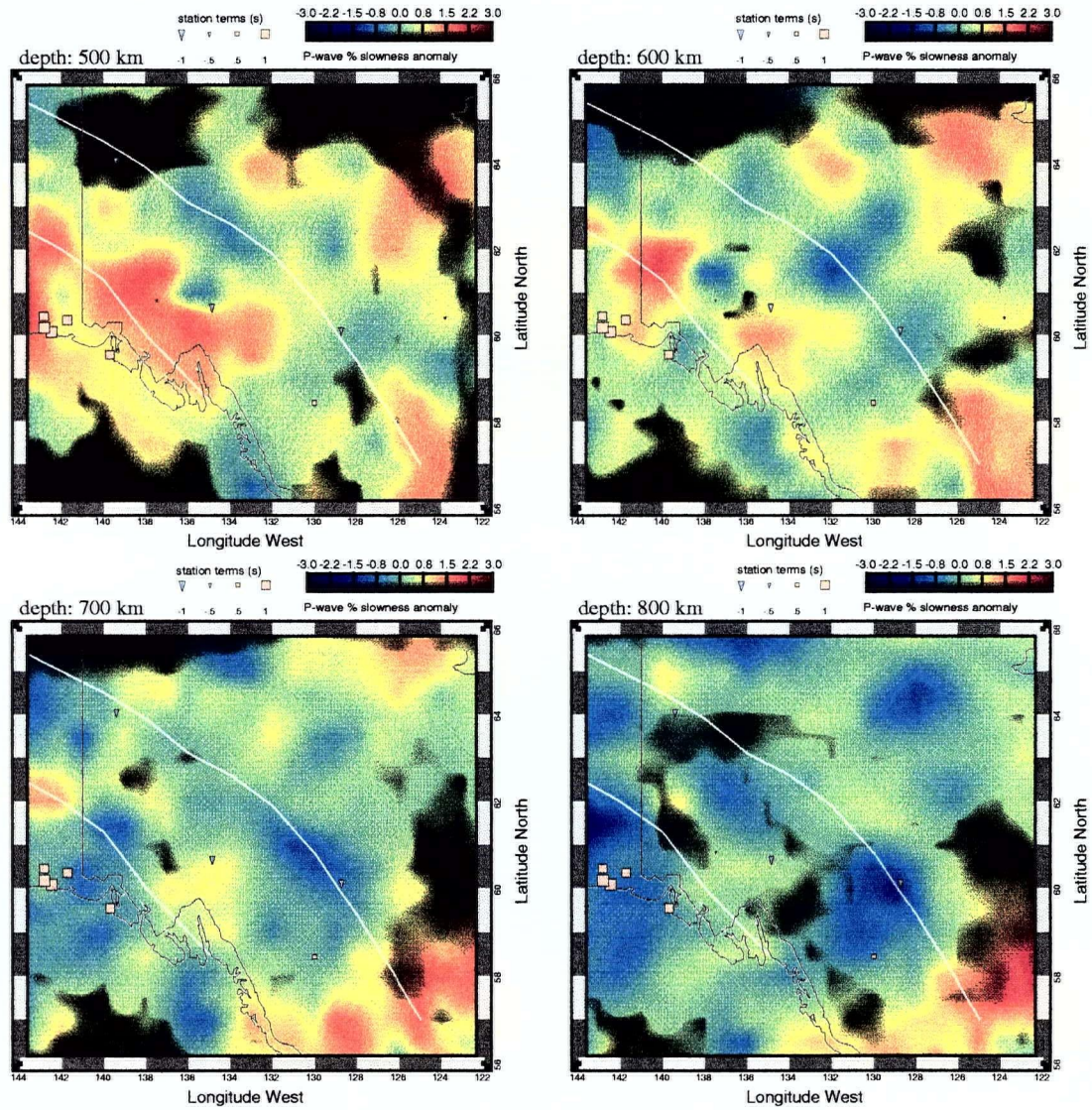


Figure 4.14: More horizontal cross-sections through the final tomographic model; see the previous figure for details.

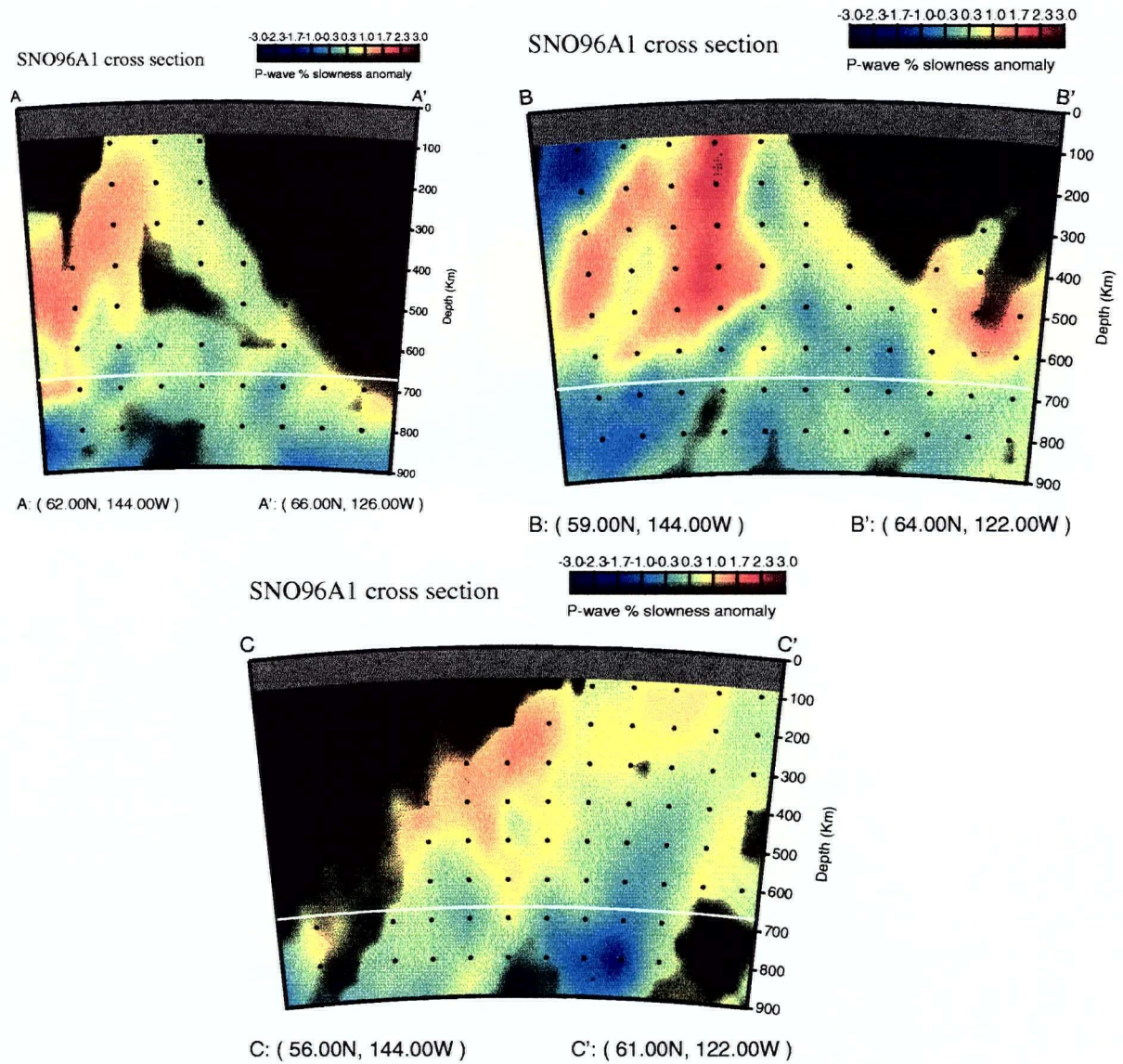


Figure 4.15: Southwest-to-northeast cross sections through the final tomographic model; see figure 4.13 for cross-section locations.

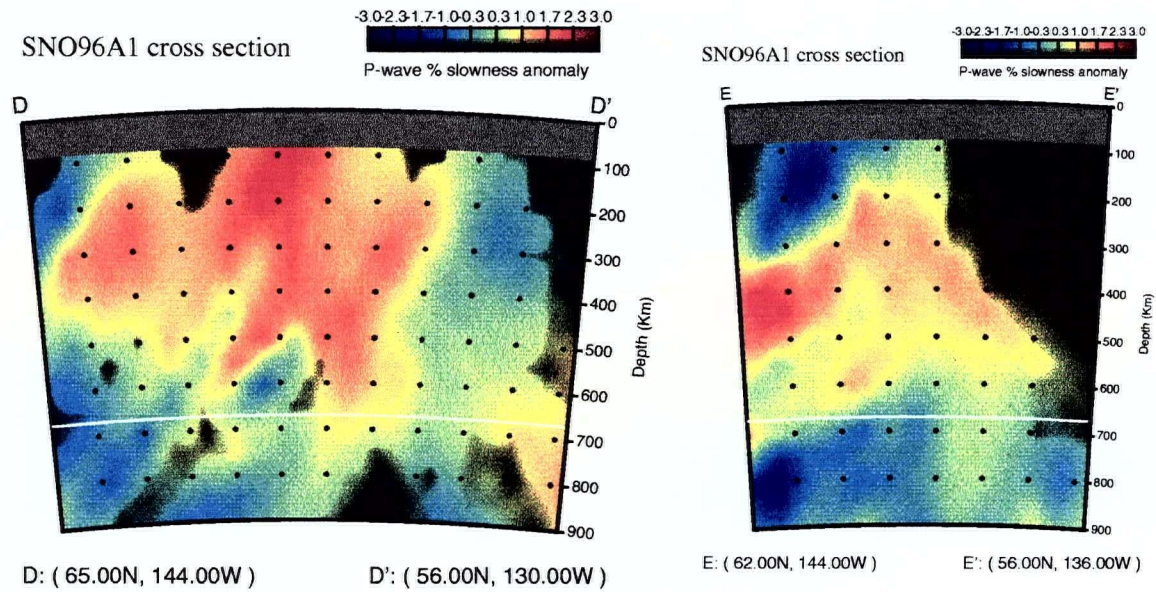


Figure 4.16: Northwest-to-southeast cross sections through the final tomographic model; see figure 4.13 for cross-section locations.

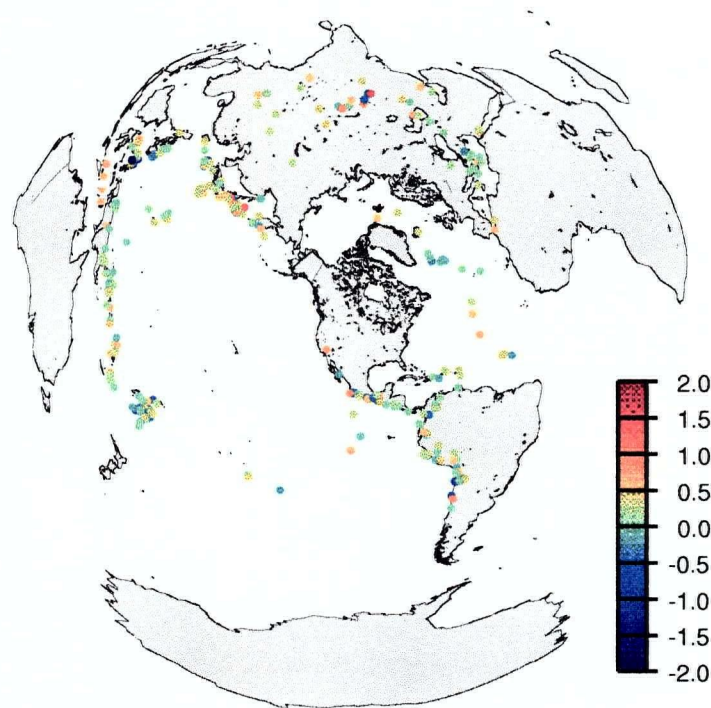


Figure 4.17: A map of the event static corrections for the final tomographic model.

and event static corrections. The event statics (figure 4.17) are generally small in magnitude and do not display any discernible structure. As structure in the event corrections may indicate problems with the inversion, this is a reassuring sign. The station corrections (figure 4.13) show mostly small negative values for the Canadian stations, and positive values centered near 1 second for the Alaskan stations. This may be reflective of thin or high-velocity crust on the Alaska side, or, more likely, may be the result of a difference in response between the Canadian and Alaskan instruments.

The strongest structure visible in the model is a large positive slowness anomaly, centered at about 60°N by 136°W at the 300 km level, ranging from 100 km to 600 km depth (although the vertical extent may be exaggerated by up to 100 km due to smearing). The anomaly appears to dip slightly to the southeast (see section D-D' in figure 4.16), and is elongated in a northwest-southeast direction. The dip is unlikely to be a smearing artifact, as it is oriented opposite to the expected direction of smearing. Its extent is greatest between 300 and 400 km depth, where it is about 700 km long (though it may extend beyond the model's edge) and 400 km wide. The northeastern edge of the anomaly, which approximately parallels the Tintina and Denali faults, is particularly sharp. The positive anomaly appears to extend beneath a negative anomaly (described below) to a depth of about 500 km (see, in particular, section B-B', in figure 4.15).

To the southwest of this anomaly, in the southwestern corner of the model, a smaller negative slowness anomaly is present. This feature extends from the top of the model (at 100 km) to a depth of about 250 km. It is not much bigger than the smallest feature this experiment was able to resolve (see previous section); however, it lies in the westernmost portion of the model, where resolution is sharpest.

Other than these two features, the model displays few significant slowness anomalies. There are indications of structure in the eastern part of the model, particularly a positive anomaly at about 63°N by 126°W which appears to extend to 700 km depth; however, this is in the region

where the resolution of the model deteriorates considerably.

Chapter 5

Discussion of results

5.1 The nature of the observed anomalies

In the previous chapter, two significant P-wave anomalies located in this study were described: a large positive slowness (low velocity) anomaly located between the Tintina and Denali faults and extending to considerable depth (400-600 km), and a negative slowness (high velocity) anomaly at the western edge of the model, penetrating to about 250 km depth. The high-velocity anomaly lies in roughly the expected horizontal position of the edge of the subducted slab from the Alaska subduction zone (figure 5.1). The depth and configuration of the slab edge are poorly constrained from previous studies, due to the decline in Benioff-zone seismicity east of 145°W (Stephens et al, 1984; Page et al., 1989). Extrapolation from the nearest available control on the slab location would suggest a depth to the top of the slab of about 50 km at 61°N by 143°N (Zhao et al., 1995). This extrapolation, combined with the slab thickness of 45-55 km from the tomographic model of Zhao et al. (1995), implies that the observed high-velocity anomaly is thicker and deeper than the actual slab, although the limited vertical resolution at upper levels and the general tendency toward downward smearing of structure in our inversion may account for much of this discrepancy.

60°N, trending approximately north-south. Based on reconstructions of past plate motions in this area (Engebretson et al., 1985), and estimates of current plate motions (Riddihough and Hyndman, 1991), the component of convergence between the North American and Pacific plates would place the edge of a rigid slab somewhat farther east than we have observed, although this statement is dependant on what assumptions are made about past plate boundary configurations. Therefore, our results suggest that the edge of the slab has not behaved rigidly. Additional support for the notion that the slab edge extends no farther than the 141°W meridian is provided by the absence of Neogene arc volcanism west of that line (Souther and Yorath, 1991).

The large low-velocity feature is better resolved, as it lies in that portion of the model where, according to the resolution test, the horizontal and vertical resolutions are good. Considering its large size, and the 100 km resolution of the model in all directions in this region, the recovered shape of the anomaly is likely to be approximately correct (compare this to the large-spike resolution test, in figures 4.7 and 4.8). Therefore, this feature may be interpreted in more detail, and it will be important to ascertain its magnitude, and investigate its possible origin.

The large low-velocity feature we observe reaches a maximum magnitude of 3%. This may be considered to be a lower bound on the true anomaly, as the smoothing inherent in the inversion tends to reduce the amplitude of sharp features. The large-spike resolution test showed a drop from a 4% peak anomaly in the input model to a 2.5% peak anomaly in the recovered model, for the worst-case scenario of a spike-like feature. For smoother features the underestimation should be less. We can thus state with some confidence that the true anomaly is at least 3% of the IASP91 slowness, and may be as much as 5%. With this in mind, we can attempt to explain the magnitude of the anomaly in terms of compositional and thermal heterogeneity.

If we assume a peridotite mantle composition, the magnitude of slowness anomaly expected due to compositional factors is limited. Lang (pers. comm.) calculated the difference in

predicted P-wave velocity for two end-member mantle xenolith compositions from the northern Cordillera, and found that the maximum slowness perturbation obtainable was less than 1%. More generally, Sobolev et al. (1996) found that for peridotite mantle, velocity variations are quite small, seldom exceeding 1% even for fairly extreme peridotite compositions; similar results were obtained by Humphreys and Dueker (1994b). We therefore conclude that the low-velocity feature we have observed cannot be explained as a purely compositional feature, and that a thermal anomaly must be present.

The interpretation of mantle images derived from seismic tomography in terms of temperature is an intricate problem. The most common method employed is to use experimentally derived temperature derivatives of seismic velocities. Such methods tend to produce unrealistically large temperature anomalies ($\approx 400^\circ\text{C}$ for a 3% anomaly) (Sobolev et al., 1996; Humphreys and Dueker, 1994a), which in most regions would indicate intersection with the solidus and the production of partial melt on a large scale. Sobolev et al. (1996) argued that this is due to the failure of such calculations to account for other temperature-dependent changes in the rock that occur over longer periods of time, particularly mineral reactions (e.g. the temperature-dependent partitioning of aluminum), anelasticity, and small degrees of partial melt of hydrous phases. Taking these factors into account, and employing chemical information obtained from mantle xenoliths, the authors determined that the 4% positive P-wave velocity perturbation measured in the experiment they examine (the French Massif Central) represents a 100-200° positive mantle temperature anomaly. Detailed mineral physics would be required to fully resolve the matter, but we presume our results to be comparable to those of Sobolev et al. (1996), and so conclude that the 3% anomaly that we have observed requires less than 200° of thermal anomaly, and is probably closer to 100°, depending on the degree of compositional variability.

5.2 Plume models for the observed low-velocity feature

Deep-rooted low-velocity mantle anomalies have frequently been ascribed to mantle plumes. Mantle plumes, in general, are thought to consist of a narrow (100-200 km in diameter) conduit of material which widens into a broader head only above 100-200 km depth (White and McKenzie, 1995; Griffiths and Campbell, 1990; Davies, 1994). Tomographic images of mantle plumes beneath the French Massif Central (Granet et al., 1995) and Yellowstone (Humphreys and Dueker, 1994a) have located anomalies of similar magnitude and shape (but lesser extent, both vertically and laterally) to the one described here, although neither of these experiments permitted the recovery of structure below 300 km.

However, in both of the cases referenced above there are surface expressions of current plume activity, in the form of substantial hot-spot magmatism and uplift, which have not been observed in the northern Cordillera (Souther and Yorath, 1991). In addition, if a plume were currently present beneath the northern Cordillera, we would expect to see some indication of a plume track out to the northern B.C. coast, due to the westward motion of the North American continent. Although plume tracks are not necessarily visible above thick continental lithosphere (Davies, 1994), the plume should have affected the continental margin. We might expect such a track to continue onto the Pacific plate, curving northward due to plate motions, although the Pacific portion might well have been subducted (Engebretson et al., 1995). No such track is visible on either of the Pacific and North American plates. Finally, although resolution is limited, the general geometry of the observed anomaly does not match that expected for mantle plumes. The large, deep-rooted anomaly we have observed is considerably broader below 200 km than would be expected from such models. In particular, our anomaly is somewhat larger and considerably deeper than the feature observed at Yellowstone (Humphreys and Dueker, 1994a). Due to these objections, we do not favor the interpretation that the low-velocity anomaly we have observed represents a mantle plume beneath the northern Cordillera, although it cannot

completely be ruled out.

A second possibility is that this feature is a consequence of past plume activity. Precedent for this is given in Vandecar et al. (1995), who describe a 1.5-2% slowness anomaly located beneath the Parana Basin flood basalts of the Brazilian shield. These authors relate both the flood basalts and the anomaly to the eruption of the Tristan de Cunha plume in the Cretaceous. The anomaly they observe penetrates to 600 km (the bottom of their model), and is similar in appearance to the one located in this study.

The Anahim Belt, a late Cenozoic chain of volcanic and plutonic rocks in central British Columbia, has been attributed to plume activity and so provides the nearest candidate plume; however, there are no surface rocks linked to this magma source in the northern Cordillera, and in any case, this plume would have been located a considerable distance out to sea at 20 Ma, due to the westward motion of North America (Souther, 1986; Engebretson et al., 1995). The only nearby hotspot track is located offshore of the Queen Charlotte Islands, ending at the the Bowie seamount (Nataf and VanDecar, 1983; Batiza, 1989); however, it has probably never underlain the North American continent and so did not affect our region. Johnston et al. (1996) link the Carmacks group, a Late Cretaceous volcanic sequence, to the Yellowstone hotspot; the presence of flood basalts in the sequence suggests that it represents the initial effusion of the plume. The possibility then arises that the low-velocity anomaly we have detected is a preserved remnant of the Cretaceous Yellowstone plume head.

There are, however, a number of serious objections to this hypothesis. First, the magnitude of the anomaly we observe is considerably greater than that described in Vandecar et al. (1995) (3% versus 1.5%), and is of comparable magnitude to those observed over currently active plumes (in the 2%-4% range) (Granet et al., 1995; Humphreys and Dueker, 1994a; Hoernle et al., 1995). In addition, while the Brazilian anomaly lies in a stable shield region, undisturbed by plate interactions since the Cretaceous, the northern Cordillera has experienced continuous

activity over the last 100 Ma. In particular, it is difficult to see how any mantle anomaly could have survived the subduction of the Kula plate, as the Kula slab probably passed through the position of our anomaly and should have completely disrupted it. The anomaly we observe is therefore unlikely to be older than 45 or 50 Ma, and is probably much younger. It is primarily due to this last objection that we believe that the plume-remnant hypothesis can be rejected.

5.3 Plate-related models for the observed low-velocity feature

There exist several possible sources for upper-mantle anomalies related to crust-mantle interactions and plate motions. The first stems from the widely accepted observation that orogenic belts are generally underlain by thinner lithosphere and hotter underlying mantle than other continental regimes. The "orogeny paradox" discussed by Silver and Chan (1991) refers to the difficulty in reconciling this observation with the expectation of an advectively thickened lithosphere in collisional zones. Delamination of continental lithosphere (Houseman et al, 1981) is a mechanism frequently called upon to resolve this apparent contradiction; however, the observed correlation between surface geologic fabric and lithospheric seismic anisotropy in orogenic belts (Silver and Chan, 1991) implies that the mantle lithosphere beneath such belts is not removed. Kincaid and Silver (1996) attempt to account for lithospheric thinning and heating beneath orogenies as being the result of strain heating due to lithospheric collision, and find that such heating may produce considerable thermal anomalies above 100 km depth for moderately fast convergence rates, although such anomalies are found to be short-lived. Whatever the physical mechanism, the association between lithospheric zones of high deformation and low upper-mantle seismic velocities is widely accepted.

In the case we are considering, lithospheric deformation is occurring between the Pacific and North American plates where they converge along the Alaska subduction zone, as well as to a lesser degree along the Fairweather-Queen Charlotte transform faults, where a component of

east-west convergence exists (Engebretson et al., 1995; Riddihough and Hyndman, 1991; see also Russo and Silver, 1996). In this context, the eastern edge of the low-velocity anomaly, which lies subparallel to and between the Tintina and Denali faults, may, at shallower levels, mark the eastern boundary of deformation in the subcrustal lithosphere. Deformation is likely to be particularly severe at the corner in the North American plate boundary formed by the junction between the Alaska panhandle and mainland, as evidenced by the continuing uplift of the St. Elias Mountains (Gabrielse et al., 1991) above an underplating or subducting Yakutat block (Bruns, 1983). Termination of the positive slowness anomaly to the southeast between stations WHY and DLBC would tend to support this, as it indicates concentration of the anomaly in this corner. However, it is unlikely that lithospheric heating, whatever its mechanism, is a sufficient explanation for the vertical extent of the low-velocity anomaly that we have detected, and therefore some other mechanism must be called upon to explain the heating of the upper mantle below 200 km depth.

Our preferred model for the low-velocity feature is upwelling related to the presence of a slab window in the northern Cordillera. A slab window is generally defined as being the gap between two slabs formed by the subduction of a spreading ridge (Dickinson and Snyder, 1979). When the ridge encounters the trench, growth of the spreading plates ceases in the subducted portions. As the plates at the surface continue to separate, a widening gap opens in the descending slab, its geometry dependent on the spreading rate, subduction rate, angle of subduction and angle between the ridge and the trench (figure 5.2). The geometry of slab windows is discussed in some detail in Thorkelson (1996), while slab windows beneath the North American Cordillera are discussed in Thorkelson and Taylor (1989). Two are expected to exist in present times (figure 5.3), one beneath California south of the Mendocino Triple Junction, the other beneath B.C. and the Yukon between the northern end of the Explorer Plate and the Alaska subduction zone. Our area of interest lies in the northern half of the B.C.-Yukon slab window; the slab

edge that we have imaged corresponds well with the expected western edge of the window.

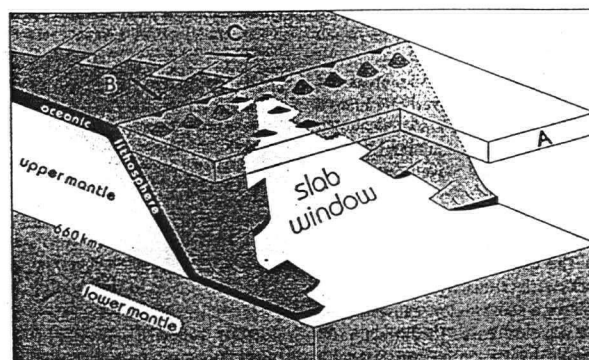


Figure 5.2: Geometry of a slab window, from Thorkelson (1996).

It is argued that mantle upflow is to be expected along the edges of slab windows (Thorkelson, 1994; Hole et al., 1991; Thorkelson, 1996). The retreat of the slab decompresses the underlying asthenosphere, which rises to fill the gap; this brings hotter material into the slab window, and the decompression may lead to partial melt and alkalic volcanism. This ties in well with our observations: the low-velocity anomaly parallels the slab edge, and peters out farther into the proposed window. As well, the recent low-volume volcanism in this region (Souther and Yorath, 1991; Souther, 1991) is suggestive. These volcanic rocks, generally associated with normal faults, occur throughout the northern Cordilleran slab window, and have alkalic compositions indicative of an undepleted mantle source (Souther and Yorath, 1991). They have generally been tied to young extension in the region, but could well be associated with slab-window decompression melting; however, such Neogene volcanism is not restricted to the edge of the slab window.

Although little geophysical work on the topic of slab windows has been performed (in particular, the geodynamics of slab window upflow have not been worked out), there is support for this hypothesis in the form of a teleseismic tomography study of the northern end of the

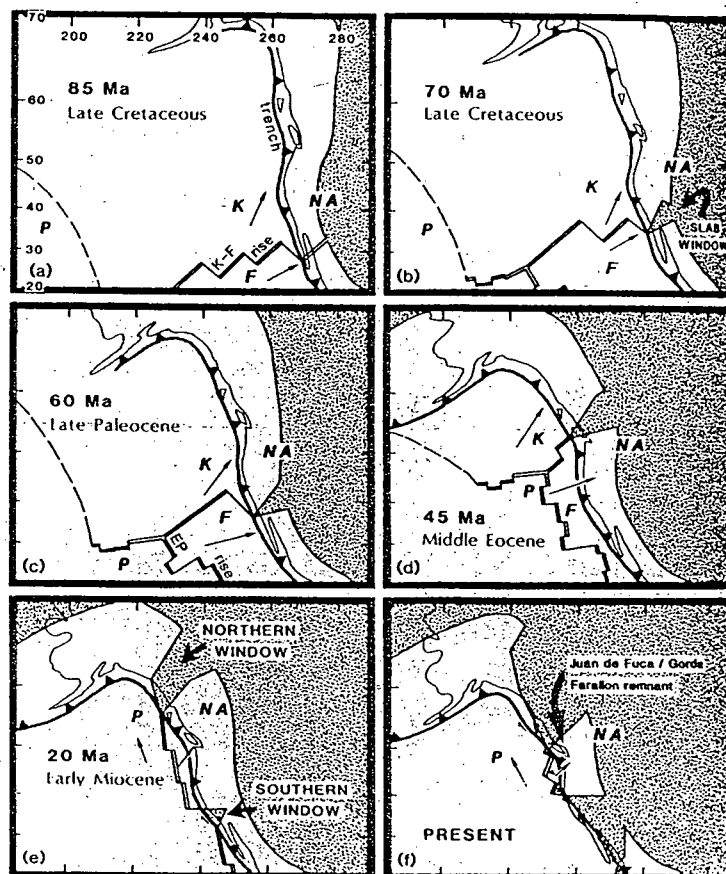


Figure 5.3: History of slab windows in the North American Cordillera from the Late Cretaceous to the present. From Thorkelson and Taylor (1989).

southern Cordilleran slab window (Benz et al., 1992). Although the geometry of this window is considerably different, the authors noted a negative velocity anomaly of up to 5.5% along the window edge, reaching depths of up to 170 km (in a model with a maximum depth of 250 km). Thus, there is precedent for the tomographic observation of a low-velocity feature along the edge of a slab window, albeit not to the depths to which we have resolved this type of structure.

The principal difficulty with this type of model is that the depth to which the withdrawal of a slab would produce a significant thermal anomaly is likely quite limited. Withdrawing the ≈ 50 km thick slab imaged by Zhao et al. (1995) seems unlikely to be sufficient to account for a thermal anomaly below 150 or 200 km depth. This difficulty may perhaps be resolvable by an appeal to ridge dynamics. Consistent lateral motion of the slab due to the opening of the window could produce circulation in the upper mantle (figure 5.4); the scale of such circulation would be comparable to the width of the moving slab, and so could affect mantle below 600 km (Hager and O'Connell, 1979). This is borne out by Grand (1994), who imaged a low-velocity mantle anomaly beneath the Mid-Atlantic Ridge to a depth of 400 km. Due to the mild component of east-west convergence between North America and the Pacific plate, the slab window is unlikely currently to be widening at a significant rate; however, the slab window has opened considerably in the past 20 Ma (Thorkelson and Taylor, 1989), requiring considerable lateral slab motion over that period, which may have been enough to produce the required circulation. Changes in slab dip may also have contributed to such mantle circulation, in that steepening of slab dip angles would require upflow to accommodate the enlarged mantle wedge above the slab (Thorkelson and Taylor, 1989). The hypothesis that the low-velocity anomaly we have observed represents slab window-related upflow is quite speculative and needs to be tested by further work; however, we favor it as being the model that best explains our the deep-seated nature of the positive slowness anomaly.

Other aspects of plate-mantle interaction may affect the model we see. The unusually sharp

northeastern edge of the low-velocity anomaly at shallow depths is a well-resolved feature that demands explanation. Its trend is roughly parallel to that of the Cordilleran deformation front, somewhat outboard of the edge of the ancestral North American miogeocline (figure 1.2). A possible hypothesis for the sharp edge we see is that it represents the edge of thicker, older, and colder lithosphere beneath ancestral North America, blocking the eastward flow of warmer material welling up along the slab edge. The more diffuse southeastern boundary of the anomaly in this context would then represent the limit of the slab's influence on upper-mantle circulation. Finally, the presence of a branch of the low-velocity anomaly extending beneath the inferred slab suggests that the flow in this region may be more complex than can be explained by simple geometric models.

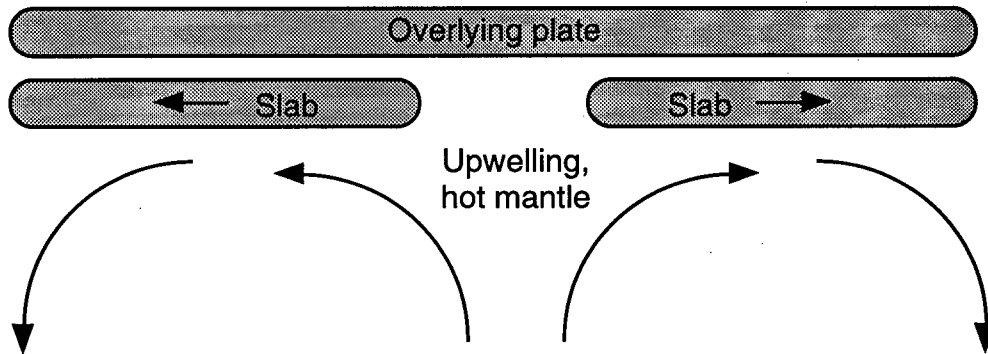


Figure 5.4: A conceptual model of flow due to the opening of a slab window. This pattern of flow would be superimposed on the downflow generated by subduction.

5.4 Summary

We have located two significant upper-mantle P-wave velocity anomalies beneath the northern Cordillera. We have interpreted the first, a high-velocity, relatively shallow region at the extreme west of our model, as reflecting the presence of the edge of the subducting Pacific slab, its position having been smeared downward due to the poor resolution at the edges of the model.

The second anomaly we have located, a large deep-rooted low-velocity zone in the best-resolved portion of our model, is more difficult to interpret. We suggest that it is a positive thermal anomaly of less than 200°C, possibly with some associated chemical anomaly as well. The most obvious source for such an anomaly is a mantle plume; however, there are no magmatic indications of a plume currently in this region, nor is there the plume track we would expect to find leading to it. Rather, the late Cenozoic intraplate volcanics in this area are widely scattered over much of the Yukon and British Columbia. The possibility that this anomaly represents the remnant of an older plume carried away by plate motions has been considered; however, it is improbable that such a deep-rooted anomaly could have survived the subduction of the Kula plate, and remained coupled to a crustal sliver which would have to have been transported northward by over 1000 km.

We therefore favor the hypothesis that this low-velocity feature represents a combination of upwelling along the edge of the northern Cordilleran slab window, perhaps due to circulation produced by past lateral motion of the Pacific slab or other interactions between the slab edge and the asthenosphere, and a contribution at the upper levels from strain heating beneath the St. Elias Mountains. Such a combination of effects would explain the southwest-northeast orientation of the anomaly, as well as its position. Such upwelling has been previously detected in the southern Cordilleran slab window (near the Mendocino triple junction) (Benz et al., 1992); the presence of Neogene volcanic rocks of intraplate character throughout the area of the northern Cordilleran slab window as defined in Thorkelson and Taylor (1989) is suggestive of window-related extension and melting. However, in order to confirm this hypothesis, there remains both theoretical and experimental work to be done. The geodynamics of such slab-edge upwelling has not been worked out; although there are strong qualitative arguments for the existence of such upwelling, we know little about its magnitude and depth penetration. Experimentally, heat-flow data from above the anomaly may better constrain its thermal magnitude;

as well, the location and configuration of the edge of the Pacific slab is poorly constrained, and could be determined through a more detailed tomographic experiment.

Bibliography

- Atwater, T. (1989). Plate tectonic history of the northeast Pacific and western North America, in *The Eastern Pacific Ocean and Hawaii*, edited by E.L. Winterer, Donald M. Hussong, and Robert W. Decker, 21-72.
- Batiza, R. (1989). Seamounts and seamount chains of the eastern Pacific, in *The Eastern Pacific Ocean and Hawaii*, edited by E.L. Winterer, Donald M. Hussong, and Robert W. Decker, 289-306.
- Benz, H.M., G. Zandt, and D.H. Oppenheimer (1992). Lithospheric structure of northern California from teleseismic images of the upper mantle, *J. Geophys. Res.* **97**, 4791-4807.
- Bruns, T.R. (1983). Model for the origin of the Yakutat block, an accreting terrane in the northern Gulf of Alaska, *Geology* **11**, 718-721.
- Creager, K.C. and T.H. Jordan (1984). Slab penetration into the lower mantle, *J. Geophys. Res.* **89**, 3031-3049.
- Davies, G.F. (1994). Thermomechanical erosion of the lithosphere by mantle plumes, *J. Geophys. Res.* **99**, 15,709-15,722.
- Dickinson, W.R. and W.S. Snyder (1979). Geometry of subducted slabs related to the San Andreas transform, *J. Geol.* **87**, 609-627.
- Edwards, B.R., T.S. Hamilton, J. Nicholls, M.Z. Stout, J.K. Russell, and K. Simpson (1996). Late Tertiary to Quaternary volcanism in the Atlin area, northwestern British Columbia, *Current Research 1996-A*, Geological Survey of Canada, 29-36.
- Engelbreton, D.C., A. Cox, and R.G. Gordon (1985). *Relative motions between oceanic and continental plates in the Pacific basin*, Geological Society of America Special Paper 206, 59 pp.
- Erdmer, P. and J.K. Mortensen (1993). A 1200-km-long Eocene metamorphic-plutonic belt in the northwestern Cordillera: evidence from southwest Yukon, *Geology* **21** 1039-1042.
- Gabrielse, H., J.W.H. Monger, J.O. Wheeler, and C.J. Yorath (1991). Tectonic framework, in *Geology of the Cordilleran Orogen in Canada*, edited by H. Gabrielse and C.J. Yorath, 15-28.

- Gorman, A.R., R.M. Clowes, R.M. Ellis, M.J.A. Burianyk, E.R. Kanasewich, Z. Hajnal, G.D. Spence, G.R. Keller, and A.R. Levander (1995). Seismic refraction imaging of the crust and upper mantle in the Archean Hearne Craton, Southern Alberta, Canada, for 1995 Fall meeting of the American Geophysical Union.
- Grand, S.P. (1994). Mantle shear structure beneath the Americas and surrounding oceans, *J. Geophys. Res* **99**, 11,591-11,621.
- Granet, M., M. Wilson, and U. Achauer (1995). Imaging a mantle plume beneath the French Massif Central, *Earth Planet. Sci. Let.* **136**, 281-296.
- Griffiths, R.W. and I.H. Campbell (1990). Stirring and structure in mantle starting plumes, *Earth Planet. Sci. Let.* **99**, 66-78.
- Hager, B.H. and R.J. O'Connell (1979). Kinematic models of large-scale flow in the Earth's mantle, *J. Geophys. Res* **84**, 1031-1048.
- Hoernle, K., Y. Zhang, and D. Graham (1995). Seismic and geochemical evidence for large-scale mantle upwelling beneath the eastern Atlantic and western and central Europe, *Nature* **374**, 34-39.
- Hole, M.J., G. Rogers, A.D. Saunders, and M. Storey (1991). Relation between alkalic volcanism and slab window formation, *Geology* **19**, 657-660.
- Houseman, G.A., D.P. McKenzie, and P. Molnar (1981). Convective instability of a thickened boundary layer and its relevance for the thermal evolution of continental convergent belts, *J. Geophys. Res* **86**, 6115-6132.
- Humphreys, E.D. and K.G. Dueker (1994a). Western U.S. upper mantle structure, *J. Geophys. Res* **99**, 9615-9634.
- Humphreys, E.D. and K.G. Dueker (1994b). Physical state of the western U.S. upper mantle, *J. Geophys. Res* **99**, 9635-9650.
- Irving, E., D.J. Thorkelson, P.M. Wheadon, and R.J. Enkin (1995). Paleomagnetism of the Spences Bridge Group and northward displacement of the Intermontane Belt, British Columbia: a second look, *J. Geophys. Res* **100**, 6057-6071.
- Johnston, S.T., P.J. Wynne, D. Francis, C.J.R. Hart, R.J. Enkin, and D.C. Engbretson (1996). Yellowstone in Yukon: the Late Cretaceous Carmacks group, *Geology*, in press.
- Kennett, B.L.N. and E.R. Engdahl (1991). Traveltimes for global earthquake location and phase identification. *Geophys. J. Int* **105**, 429-465.
- Kincaid, C. and P. Silver (1996). The role of viscous dissipation in the orogenic process, *Earth Planet. Sci. Let.* **142**, 271-288.

- Lowe, C., R.B. Horner, J.K. Mortensen, S.T. Johnston, and C.F. Roots (1994). New geophysical data from the northern Cordillera: preliminary interpretations and implications for the tectonics and deep geology, *Can. J. Earth Sci.* **31**, 891-904.
- Lowe, C. and J.F. Cassidy (1995). Geophysical evidence for crustal thickness variations between the Denali and Tintina Fault Systems in west-central Yukon, *Tectonics* **14**, 909-917.
- Monger, J.W.H. and W.J. Nokleberg (1996). Evolution of the North American Cordillera: generation, fragmentation, displacement and accretion of successive North American plate-margin arcs, for *1995 Geological Society of Nevada Symposium on Geology and Ore Deposits of the American Cordillera*.
- Nataf, J.C. and J. VanDecar (1993). Seismological detection of a mantle plume?, *Nature* **364**, 115-120.
- Page, R.A., C.D. Stephens, and J.C. Lahr (1989). Seismicity of the Wrangell and Aleutian Wadati-Benioff zones and the North American plate along the Trans-Alaska Crustal Transect, Chugach Mountains and Copper River Basin, southern Alaska, *J. Geophys. Res.* **94**, 16,059-16,082.
- Parker, R.L. (1994). *Geophysical Inverse Theory*, Princeton University Press, 386 pp.
- Riddihough, R.P. and R.D. Hyndman (1991). Modern plate tectonic regime of the continental margin of western Canada, in *Geology of the Cordilleran Orogen in Canada*, edited by H. Gabrielse and C.J. Yorath, 435-455.
- Russo, R.M. and P.G. Silver (1996). Cordillera formation, mantle dynamics, and the Wilson cycle, *Geology* **24**, 511-514.
- Ryberg, T., F. Wenzel, J. Mechie., A. Egorkin, K. Fuchs, and L. Solidov (1996). Two-dimensional velocity structure beneath northern Eurasia derived from the super long-range seismic profile Quartz, *Bull. Seis. Soc. Am.* **86**, 857-867.
- Scales, J.A. and A. Gersztenkorn (1988). Robust methods in inverse theory, *Inverse Problems* **4**, 1071-1091.
- Silver, P.G. and W.W. Chan (1991). Shear wave splitting and subcontinental mantle deformation, *J. Geophys. Res.* **96**, 16,429-16,454.
- Skulski, T., Francis, D., and Ludden, J. (1991). Arc-transform magmatism in the Wrangell volcanic belt, *Geology* **19**, 11-14.

- Sobolev, S.V., H. Zeyen, G. Stoll, F. Werling, R. Altherr, and K. Fuchs (1996). Upper mantle temperatures from teleseismic tomography of French Massif Central including effects of composition, mineral reactions, anharmonicity, anelasticity and partial melt, *Earth Planet. Sci. Let.* **139**, 147-163.
- Souther, J.G. (1986). The western Anahim Belt: root zone of a peralkaline magma system, *Can. J. Earth Sci.* **23**, 895-908.
- Souther, J.G. (1991). Volcanic regimes, in *Geology of the Cordilleran Orogen in Canada*, edited by H. Gabrielse and C.J. Yorath, 457-490.
- Souther, J.G. and C.J. Yorath (1991). Neogene assemblages, in *Geology of the Cordilleran Orogen in Canada*, edited by H. Gabrielse and C.J. Yorath, 373-401.
- Stephens, C.D., K.A. Fogleman, J.C. Lahr, and R.A. Page (1984). Wrangell Benioff zone, southern Alaska, *Geology* **12**, 373-376.
- Stock, J. and P. Molnar (1988). Uncertainties and implications of the late Cretaceous and Tertiary position of North America relative to the Farallon, Kula, and Pacific plates, *Tectonics* **7**, 1339-1384.
- Tapley, W.C. and J.E. Tull (1992). *SAC Users Manual, Revision 4*, Lawrence Livermore National Laboratory, 52 pp.
- Thorkelson, D.J. (1994). Ridge subduction: kinematics and implications for the nature of mantle upwelling: discussion, *Can. J. Earth Sci.* **31**, 1486-1489.
- Thorkelson, D.J. (1996). Subduction of diverging plates and the principles of slab window formation, *Tectonophysics* **255**, 47-63.
- Thorkelson, D.J. and R.P. Taylor (1989). Cordilleran slab windows, *Geology* **17**, 833-836.
- Umhoefer, P.J., J. Dragovich, J. Cary, and D.C. Engebretson (1989). Refinements of the "Baja British Columbia" plate-tectonic model for northward translation along the margin of western North America, in *Deep Structure and Past Kinematics of Accreted Terranes*, edited by John W. Hillhouse, 101-111.
- VanDecar, J.C. (1991). *Upper-Mantle Structure of the Cascadia Subduction Zone from Non-Linear Teleseismic Travel-Time Inversion*, Ph.D. thesis, Univ. of Washington, Seattle, 165 pp.
- VanDecar, J.C. and R.S. Crosson (1990). Determination of teleseismic relative phase arrival times using multi-channel cross correlation and least squares, *Bull. Seis. Soc. Am.* **80**, 150-169.

- VanDecar, J.C., D.E. James, and M. Assumpção (1995). Seismic evidence for coherent flow of the crust and upper mantle below South America since the breakup of Gondwana, *Nature* **378**, 25-31.
- von Huene, R. (1989). Continental margins around the Gulf of Alaska, in *The Eastern Pacific Ocean and Hawaii*, edited by E.L. Winterer, Donald M. Hussong, and Robert W. Decker, 383-401.
- White, R.S. and D. McKenzie (1995). Mantle plumes and flood basalts, *J. Geophys. Res* **100**, 17,543-17,585.
- Zhao, D., D. Christensen, and H. Pulpan (1995). Tomographic imaging of the Alaska subduction zone, *J. Geophys. Res* **100**, 6487-6504.

Appendix A

List of earthquakes used in this experiment

The following is a list of the teleseismic earthquakes recorded during this experiment that were used in the travel-time inversion. The event times and locations given are preliminary.

94/01/05	13:24:09	39.10N	15.10E	273.0	5.7	77.29	23.42	
94/05/23	06:46:16	35.60N	24.70E	76.0	6.0	82.34	16.62	
94/05/26	08:26:52	35.30N	4.10W	10.0	5.7	75.95	39.57	
94/05/31	17:41:55	7.40N	72.00W	12.0	6.3	70.48	110.58	
94/07/01	10:12:41	40.20N	53.40E	41.0	6.0	78.88	353.58	
94/07/01	19:50:04	40.20N	53.40E	44.0	5.6	78.89	353.57	
94/08/18	01:13:05	35.50N	0.10W	9.0	5.7	76.96	36.38	
95/03/08	03:45:58	16.60N	59.60W	8.0	6.3	68.44	94.45	
95/04/17	07:14:35	33.80N	38.60W	10.0	5.8	63.91	66.94	
95/05/13	08:47:12	40.20N	21.70E	14.0	6.2	77.38	18.15	
95/06/15	00:15:48	38.40N	22.30E	14.0	6.0	79.19	18.05	
95/07/21	22:44:08	36.40N	103.30E	33	5.6			GANSU, CHINA [MCBB]
95/07/24	19:13:21	55.51N	35.18W	10.0	5.4Mb	A		NORTH ATLANTIC OCEAN
95/07/25	15:13:25	10.72N	40.99W	10.0	5.5Ms	B		NORTHERN MID-ATLANTIC RIDGE
95/07/26	23:41:58	2.50N	127.80E	33	6.1			NORTHERN MOLUCCA SEA [MHBE]
95/07/28	14:29:04	21.00S	175.40W	33	6.2			TONGA ISLANDS [MJAS]
95/07/29	16:18:44	30.40N	138.30E	433	5.4			SOUTH OF HONSHU, JAPAN
95/07/30	05:11:21	23.40S	70.10W	33	7.8			NEAR COAST OF NORTHERN CHILE
95/07/30	11:51:18	29.30N	129.40E	33	5.5			RYUKYU ISLANDS [MLAY]
95/07/31	08:48:33	10.40S	77.80W	93	5.7			NEAR COAST OF PERU [MMAK]
95/08/03	08:18:53	28.10S	68.90W	103	5.8			LA RIOJA PROVINCE, ARGENTINA
95/08/06	11:59:29	44.42N	147.22E	33.0	5.4Mb			KURIL ISLANDS
95/08/14	04:37:05	4.64S	151.10E	33.0	6.5Mb	A		NEW BRITAIN REGION, P.N.G.
95/08/16	10:27:28	5.73S	154.09E	33.0	7.8Ms	B		SOLOMON ISLANDS
95/08/16	16:24:28	5.27S	153.76E	33.0	6.8Ms	B		NEW IRELAND REGION, P.N.G.
95/08/16	20:58:57	29.13N	128.80E	33.0	5.5Ms	B		NORTHWEST OF RYUKYU ISLANDS
95/08/16	23:10:27	5.75S	154.09E	70.6	7.2Ms	A		SOLOMON ISLANDS
95/08/17	00:15:52	5.88S	153.95E	33.0	6.6Ms	B		NEW IRELAND REGION, P.N.G.
95/08/17	00:59:57	41.57N	88.73E	0.0	6.1Mb	A		SOUTHERN XINJIANG, CHINA
95/08/17	10:01:27	5.01S	153.32E	33.0	6.4Ms	B		NEW IRELAND REGION, P.N.G.
95/08/17	23:14:19	36.40N	71.30E	238.0	5.5			AFGHANISTAN-TAJIKISTAN BORD RE

APPENDIX A. LIST OF EARTHQUAKES USED IN THIS EXPERIMENT

79

95/08/18 19:07:28	18.94N 144.89E	500.0	5.0Mb	B	MARIANA ISLANDS
95/08/19 21:43:31	4.99N 75.65W	126.3	6.2Mb	A	COLOMBIA
95/08/23 07:06:02	18.89N 145.16E	597.0	6.1Mb	A	MARIANA ISLANDS
95/08/24 01:55:34	18.96N 144.89E	587.4	5.7Mb	A	MARIANA ISLANDS
95/08/24 07:54:41	18.92N 144.77E	600.0	5.2Mb	A	MARIANA ISLANDS
95/08/25 14:25:25	20.04S 178.33W	540.7	5.1Mb	A	FIJI ISLANDS REGION
95/08/25 16:51:46	18.51S 175.61W	226.6	4.9Mb	B	TONGA ISLANDS
95/08/26 06:57:18	5.64S 153.53E	33.0	6.1Ms	B	NEW IRELAND REGION, P.N.G.
95/08/26 14:47:50	8.33N 127.34E	33.0	5.4Ms	B	PHILIPPINE ISLANDS REGION
95/08/28 10:46:10	25.92N 110.32W	10.0	6.3Ms	A	GULF OF CALIFORNIA
95/08/29 08:51:33	20.79S 174.55W	33.0	5.7Ms	B	TONGA ISLANDS
95/08/29 13:06:40	2.33N 127.51E	33.0	5.3Mb	B	NORTHERN MOLUCCA SEA
95/08/31 17:10:36	15.87S 166.16E	33.0	6.5Ms	A	VANUATU ISLANDS
95/09/01 05:18:04	13.33S 74.61W	109.3	5.1Mb	B	CENTRAL PERU
95/09/01 06:30:41	0.07S 123.51E	190.9	5.2Mb	B	MINAHASSA PENINSULA, SULAWESI
95/09/06 22:48:51	14.96N 94.09W	33.0	5.4Ms	A	OFF COAST OF CHIAPAS, MEXICO
95/09/08 17:25:49	14.93N 94.15W	33.0	5.5Mb	A	OFF COAST OF CHIAPAS, MEXICO
95/09/11 04:22:52	0.97N 101.36W	10.0	5.2Mb	A	EAST CENTRAL PACIFIC OCEAN
95/09/11 11:40:30	53.79N 160.40E	18.2	5.2Mb	B	NEAR EAST COAST OF KAMCHATKA
95/09/14 14:04:31	16.79N 98.61W	21.3	7.2Ms		NEAR COAST OF GUERRERO, MEXICO
95/09/15 23:52:03	43.03N 143.73E	106.2	5.0Mb	B	HOKKAIDO, JAPAN REGION
95/09/16 01:03:37	6.14S 154.80E	159.6	5.7Mb	B	SOLOMON ISLANDS
95/09/18 20:22:13	20.33S 179.10W	617.7	4.9Mb	B	FIJI ISLANDS REGION
95/09/19 03:31:56	20.71S 68.74W	108.2	5.8Mb	C	CHILE-BOLIVIA BORDER REGION
95/09/20 23:27:35	35.71N 117.63W	5.0	5.5Mb	A	CENTRAL CALIFORNIA
95/09/22 05:39:28	5.92S 146.42E	33.0	6.0Ms	A	E NEW GUINEA REG., P.N.G.
95/09/23 02:34:13	5.80S 146.30E	33.0	5.9Ms	A	E NEW GUINEA REG., P.N.G.
95/09/23 20:56:03	24.36S 128.00W	10.0	5.4Mb	A	SOUTH PACIFIC OCEAN
95/09/23 22:31:56	10.64S 78.25W	70.0	6.2Mb	A	NEAR COAST OF PERU
95/09/26 04:39:07	41.89N 81.54E	50.9	5.4Mb	A	SOUTHERN XINJIANG, CHINA
95/09/26 07:14:37	41.79N 143.38E	33.0	6.0Mb	A	HOKKAIDO, JAPAN REGION
95/09/26 18:24:12	13.15S 166.81E	186.6	5.4Mb	B	VANUATU ISLANDS
95/10/01 15:57:15	38.03N 30.15E	33.0	6.0Ms	A	TURKEY
95/10/01 17:06:03	29.30N 139.04E	423.6	5.6Mb	A	SOUTH OF HONSHU, JAPAN
95/10/01 23:29:57	22.30S 138.83W	0.0	5.5Mb	A	TUAMOTU ARCHIPELAGO REGION
95/10/02 23:48:22	15.28S 175.01W	33.0	5.9Ms	A	TONGA ISLANDS
95/10/03 01:51:25	2.70S 77.86W	33.0	6.9Ms	A	PERU-ECUADOR BORDER REGION
95/10/03 12:44:59	2.78S 77.79W	33.0	6.1Ms	A	PERU-ECUADOR BORDER REGION
95/10/06 05:13:24	18.88N 104.18W	33.0	5.2Ms	A	NEAR COAST OF JALISCO, MEXICO
95/10/06 11:39:36	19.82S 176.14W	209.7	5.5Mb	A	FIJI ISLANDS REGION
95/10/07 21:28:05	2.73S 77.70W	33.0	5.5Mb	B	PERU-ECUADOR BORDER REGION
95/10/08 08:55:48	40.96N 72.06E	33.0	6.0Mb	A	KYRGYZSTAN
95/10/09 13:43:42	21.38S 169.86E	117.8	5.6Ms	B	LOYALTY ISLANDS REGION
95/10/09 15:35:51	18.86N 104.14W	33.0	7.6Ms	A	NEAR COAST OF JALISCO, MEXICO
95/10/12 16:52:56	18.92N 103.97W	33.0	5.5Ms	A	NEAR COAST OF MICHOACAN, MEX 4.6Mb
95/10/14 08:00:41	25.73S 177.60W	71.6	5.9Mb	A	SOUTH OF FIJI ISLANDS
95/10/15 15:04:13	6.49S 154.38E	50.9	6.0Ms	B	SOLOMON ISLANDS
95/10/18 09:30:38	36.34N 70.32E	222.8	5.7Mb	A	HINDU KUSH REGION, AFGHANISTAN
95/10/18 10:37:24	28.14N 130.38E	10.0	6.9Ms	A	RYUKYU ISLANDS
95/10/19 00:32:03	28.37N 130.25E	10.0	6.4Ms	A	RYUKYU ISLANDS
95/10/19 02:41:36	28.41N 130.64E	10.0	6.9Ms	A	RYUKYU ISLANDS

APPENDIX A. LIST OF EARTHQUAKES USED IN THIS EXPERIMENT

80

95/10/20 19:21:28	18.87N 145.12E	225.4	5.3Mb	B	MARIANA ISLANDS
95/10/21 02:38:49	16.57N 93.38W	100.0	6.3Mb	A	CHIAPAS, MEXICO
95/10/23 22:46:54	25.88N 102.25E	33.0	6.4Ms	A	YUNNAN, CHINA
95/10/26 04:23:25	39.17N 72.04E	33.0	5.4Mb	B	KYRGYZSTAN
95/10/27 21:59:57	21.95S 139.19W	0.0	5.5Mb	A	TUAMOTU ARCHIPELAGO REGION
95/10/28 14:38:33	6.33S 154.33E	33.0	5.8Mb	B	SOLOMON ISLANDS
95/10/29 06:27:20	39.64N 51.79E	33.0	5.7Mb	A	CASPIAN SEA
95/10/29 18:44:21	0.78N 126.07E	33.0	5.6Mb	B	NORTHERN MOLUCCA SEA
95/10/29 19:24:29	0.77N 125.99E	33.0	6.1Mb	A	NORTHERN MOLUCCA SEA
95/10/29 19:40:56	21.58S 179.68W	600.0	5.5Mb	A	FIJI ISLANDS REGION
95/11/01 00:35:33	28.95S 71.18W	33.0	6.3Ms	A	NEAR COAST OF CENTRAL CHILE
95/11/01 09:35:59	28.89N 130.06E	33.0	5.6Mb	B	RYUKYU ISLANDS
95/11/01 12:29:28	42.91N 80.29E	33.0	5.5Mb	B	KYRGYZSTAN-XINJIANG BDR REG.
95/11/02 22:13:45	6.74S 130.42E	100.0	5.7Mb	B	BANDA SEA
95/11/08 16:01:20	1.33N 121.67E	33.0	5.6Ms	B	MINAHASSA PENINSULA, SULAWESI
95/11/09 05:10:31	35.57N 59.90E	33.0	5.4Mb	B	NORTHERN IRAN
95/11/13 02:17:51	3.60N 126.77E	33.0	6.2Ms	B	TALAUD ISLANDS, INDONESIA
95/11/13 07:38:45	14.96S 173.60W	33.0	5.9Ms	B	SAMOA ISLANDS REGION
95/11/13 08:43:14	55.96N 114.58E	24.3	5.9Mb	A	EAST OF LAKE BAYKAL, RUSSIA
95/11/14 04:01:45	5.92S 150.43E	33.0	5.6Mb	A	NEW BRITAIN REGION, P.N.G.
95/11/14 15:14:02	18.99N 144.69E	600.0	4.5Mb	B	MARIANA ISLANDS
95/11/17 02:12:36	6.78N 72.05W	156.1	4.8Mb	B	NORTHERN COLOMBIA
95/11/18 16:24:32	46.52N 150.16E	100.0	5.0Mb	B	KURIL ISLANDS
95/11/22 04:15:11	28.54N 34.75E	10.0	7.2Ms	B	EGYPT
95/11/23 04:41:44	41.50N 142.51E	33.0	5.0Mb	A	HOKKAIDO, JAPAN REGION
95/11/24 17:24:12	44.39N 149.13E	33.0	6.4Ms	A	KURIL ISLANDS
95/11/25 13:24:01	44.39N 149.17E	33.0	5.0Mb	B	KURIL ISLANDS
95/11/26 03:04:04	12.87S 166.27E	33.0	5.8Mb	C	SANTA CRUZ ISLANDS
95/11/27 15:52:58	44.52N 149.27E	33.0	6.0Ms	A	KURIL ISLANDS
95/11/29 18:40:36	16.72S 176.62W	371.9	5.1Mb	B	FIJI ISLANDS REGION
95/11/30 15:09:23	44.22N 145.66E	145.9	6.1Mb	A	HOKKAIDO, JAPAN REGION
95/11/30 23:37:36	44.17N 149.37E	33.0	6.0Ms	A	KURIL ISLANDS
95/12/01 05:20:27	10.06N 104.04W	10.0	6.2Ms	A	OFF COAST OF MEXICO
95/12/01 10:30:12	44.42N 149.50E	33.0	5.0Mb	B	KURIL ISLANDS
95/12/02 17:13:21	44.81N 149.22E	33.0	6.5Ms	A	KURIL ISLANDS
95/12/02 17:28:16	44.50N 149.23E	33.0	5.4Mb	B	KURIL ISLANDS
95/12/02 19:40:10	44.32N 149.57E	33.0	5.4Mb	A	KURIL ISLANDS
95/12/03 18:01:09	44.85N 149.42E	33.0	8.0Ms	A	KURIL ISLANDS
95/12/03 18:14:27	45.01N 150.66E	33.0	6.3Mb	B	KURIL ISLANDS
95/12/03 21:38:36	44.60N 150.16E	33.0	5.5Mb	B	EAST OF KURIL ISLANDS
95/12/05 14:54:44	1.65N 127.31E	100.0	5.6Mb	B	HALMAHERA, INDONESIA
95/12/05 18:49:31	39.19N 40.41E	33.0	5.6Mb	B	TURKEY
95/12/06 23:17:20	44.23N 149.39E	33.0	5.6Mb	B	KURIL ISLANDS
95/12/07 03:22:03	44.36N 149.38E	33.0	5.7Mb	A	KURIL ISLANDS
95/12/07 05:12:22	44.43N 149.38E	33.0	5.8Mb	A	KURIL ISLANDS
95/12/07 10:04:13	19.94S 168.55E	33.0	5.7Ms	A	VANUATU ISLANDS
95/12/07 18:00:55	34.81N 24.06E	33.0	5.3Mb	A	CRETE
95/12/07 19:30:24	44.68N 149.57E	33.0	5.9Mb	A	KURIL ISLANDS
95/12/08 07:41:14	72.53N 2.38E	10.0	5.3Mb	B	NORWEGIAN SEA
95/12/10 03:27:49	34.78N 24.11E	33.0	5.3Mb	A	CRETE
95/12/10 22:23:15	44.42N 149.76E	33.0	6.4Ms	B	KURIL ISLANDS

APPENDIX A. LIST OF EARTHQUAKES USED IN THIS EXPERIMENT

81

95/12/10 22:48:08	44.27N 149.89E	33.0	5.5Mb	B	KURIL ISLANDS
95/12/10 23:47:00	21.24S 178.40W	412.4	5.8Mb	B	FIJI ISLANDS REGION
95/12/11 05:22:46	64.47N 17.92W	10.0	4.9Mb	B	ICELAND
95/12/11 06:17:22	51.08N 157.69E	33.0	5.2Mb	B	NEAR EAST COAST OF KAMCHATKA
95/12/11 14:09:21	18.50N 105.46W	33.0	6.1Ms	A	OFF COAST OF JALISCO, MEXICO
95/12/17 23:48:31	52.62N 32.08W	10.0	5.3Mb	B	NORTH ATLANTIC OCEAN
95/12/18 02:05:58	52.65N 142.75E	33.0	5.1Mb	B	SAKHALIN ISLAND
95/12/19 23:28:13	3.53S 140.22E	71.3	6.3Ms	B	IRIAN JAYA, INDONESIA
95/12/20 09:08:43	42.88N 145.63E	33.0	5.2Mb	B	HOKKAIDO, JAPAN REGION
95/12/20 11:39:20	27.85N 128.26E	33.0	5.3Mb	B	RYUKYU ISLANDS
95/12/21 07:54:46	12.38S 166.67E	241.8	5.0Mb	B	SANTA CRUZ ISLANDS
95/12/21 20:38:28	11.67N 86.35W	100.0	5.2Mb	B	NEAR COAST OF NICARAGUA
95/12/22 22:54:19	15.45S 68.85W	244.4	5.2Mb	A	CENTRAL BOLIVIA
95/12/25 03:19:44	36.41N 70.41E	228.0	5.4Mb	B	HINDU KUSH REGION, AFGHANISTAN
95/12/25 04:43:26	6.36S 129.23E	150.0	6.7Ms	B	BANDA SEA
95/12/26 20:10:35	47.42N 148.25E	365.4	4.9Mb	B	NORTHWEST OF KURIL ISLANDS
95/12/26 21:55:15	5.80S 150.43E	33.0	5.5Mb	B	NEW BRITAIN REGION, P.N.G.
95/12/29 13:01:40	9.91N 70.13W	33.0	5.5Mb	A	VENEZUELA
95/12/29 14:36:50	14.34N 59.89W	33.0	5.2Mb	A	WINDWARD ISLANDS
95/12/30 03:26:08	4.64S 104.66W	10.0	5.7Ms	B	CENTRAL EAST PACIFIC RISE
95/12/30 12:11:07	40.96N 143.18E	33.0	6.2Ms	B	OFF E COAST OF HONSHU, JAPAN
95/12/30 12:17:37	40.89N 143.28E	33.0	5.5Mb	B	OFF E COAST OF HONSHU, JAPAN
95/12/30 12:23:15	25.80N 125.79E	33.0	5.6Mb	C	SOUTHWESTERN RYUKYU ISLANDS
95/12/30 16:15:32	31.42N 140.10E	100.0	5.5Mb	B	SOUTH OF HONSHU, JAPAN
96/01/02 06:41:04	18.69S 69.08W	107.0	5.3Mb	B	NORTHERN CHILE
96/01/02 18:09:10	8.96N 126.22E	33.0	5.5Mb	C	MINDANAO, PHILIPPINE ISLANDS
96/01/06 15:48:32	4.08S 151.96E	100.0	5.3Mb	B	NEW BRITAIN REGION, P.N.G.
96/01/07 13:14:29	6.81S 155.55E	33.0	5.5Mb	B	SOLOMON ISLANDS
96/01/08 09:20:17	16.22N 98.11W	33.0	5.0Mb	B	NEAR COAST OF GUERRERO, MEXICO
96/01/08 10:04:51	53.22N 142.76E	33.0	5.5Mb	A	SAKHALIN ISLAND
96/01/08 11:52:12	20.29S 68.53W	140.0	5.0Mb	B	CHILE-BOLIVIA BORDER REGION
96/01/08 13:40:57	17.86S 178.70W	595.5	4.8Mb	B	FIJI ISLANDS REGION
96/01/08 13:59:44	45.36N 150.14E	28.1	5.3Mb	B	KURIL ISLANDS
96/01/10 15:57:47	6.72N 73.01W	170.0	4.6Mb	B	NORTHERN COLOMBIA
96/01/10 22:35:58	6.18S 133.49E	10.0	5.9Mb	B	ARU ISLANDS REGION, INDONESIA
96/01/11 03:51:34	8.36S 158.61E	94.9	5.6Mb	B	SOLOMON ISLANDS
96/01/13 05:26:29	51.13N 157.70E	33.0	5.4Mb	A	NEAR EAST COAST OF KAMCHATKA
96/01/14 06:28:20	44.52N 148.96E	33.0	5.4Mb	A	KURIL ISLANDS
96/01/16 05:15:23	18.68S 177.58W	300.0	5.3Mb	A	FIJI ISLANDS REGION
96/01/18 09:33:50	41.66N 77.57E	33.0	5.5Mb	B	KYRGYZSTAN-XINJIANG BDR REG.
96/01/19 19:01:59	10.37S 78.83W	35.7	5.8Mb	A	NEAR COAST OF PERU
96/01/20 08:43:04	3.30S 151.84E	300.0	5.0Mb	B	NEW IRELAND REGION, P.N.G.
96/01/22 00:10:23	44.56N 147.91E	33.0	5.2Mb	B	KURIL ISLANDS
96/01/22 08:59:53	2.82S 141.33E	33.0	6.0Mb	A	NR N COAST OF NEW GUINEA, PNG.
96/01/22 13:14:56	40.11N 142.18E	33.0	5.1Mb	B	NEAR E COAST OF HONSHU, JAPAN
96/01/25 12:45:02	18.35N 101.94W	33.0	5.2Mb	A	GUERRERO, MEXICO
96/01/26 02:21:11	30.90N 91.41E	33.0	5.2Mb	B	XIZANG
96/01/27 17:48:08	9.01N 126.48E	33.0	5.6Ms	B	MINDANAO, PHILIPPINE ISLANDS
96/01/27 21:29:57	22.30S 138.94W	0.0	5.4Mb	A	TUAMOTU ARCHIPELAGO REGION
96/01/28 00:28:29	1.99S 77.51W	152.3	4.6Mb	B	ECUADOR
96/01/29 13:06:21	11.22N 125.23E	47.9	5.4Mb	B	SAMAR, PHILIPPINE ISLANDS

APPENDIX A. LIST OF EARTHQUAKES USED IN THIS EXPERIMENT

82

96/01/30 02:28:30	47.05N 151.61E	33.0	5.4Mb	B	KURIL ISLANDS
96/01/30 21:14:57	36.47N 135.22E	366.3	5.1Mb	A	SEA OF JAPAN
96/01/31 19:21:26	44.50N 149.48E	33.0	5.3Ms	A	KURIL ISLANDS
96/01/31 20:30:44	44.49N 149.47E	33.0	5.9Ms	A	KURIL ISLANDS
96/02/01 04:21:19	17.88S 178.61W	570.4	4.7Mb	B	FIJI ISLANDS REGION
96/02/01 07:18:05	44.93N 146.26E	180.0	5.8Mb	A	KURIL ISLANDS
96/02/01 17:57:56	37.72N 19.86E	10.0	5.3Mb	A	IONIAN SEA
96/02/02 00:41:05	32.67N 137.32E	300.0	4.8Mb	B	SOUTH OF HONSHU, JAPAN
96/02/02 18:36:10	11.62N 141.31E	33.0	5.5Ms	B	WESTERN CAROLINE ISLANDS
96/02/03 11:14:22	27.25N 100.46E	33.0	6.4Ms	A	YUNNAN, CHINA
96/02/03 12:26:48	2.99N 79.18W	33.0	5.0Mb	B	SOUTH OF PANAMA
96/02/04 11:57:18	45.01N 149.45E	33.0	5.4Mb	A	KURIL ISLANDS
96/02/04 16:58:09	27.04N 100.48E	33.0	5.6Mb	B	YUNNAN, CHINA
96/02/05 06:45:24	43.93N 28.37W	10.0	5.0Mb	B	NORTHERN MID-ATLANTIC RIDGE
96/02/05 21:20:40	6.19S 154.22E	54.2	5.5Mb	B	SOLOMON ISLANDS
96/02/07 01:33:16	35.85N 136.30E	33.0	5.2Mb	B	WESTERN HONSHU, JAPAN
96/02/07 21:36:44	45.17N 149.96E	33.0	7.0Ms	A	KURIL ISLANDS
96/02/09 17:33:49	5.86S 146.50E	33.0	5.8Ms	A	E NEW GUINEA REG., P.N.G.
96/02/11 09:28:49	45.37N 150.46E	33.0	5.1Mb	B	KURIL ISLANDS
96/02/12 02:58:52	45.16N 150.15E	33.0	5.3Mb	B	KURIL ISLANDS
96/02/14 20:31:05	45.29N 150.37E	33.0	5.9Mb	A	KURIL ISLANDS
96/02/14 21:26:55	29.28N 140.37E	133.1	5.9Mb	B	SOUTH OF HONSHU, JAPAN
96/02/16 11:34:30	15.08S 173.63W	33.0	5.6Ms	B	TONGA ISLANDS
96/02/16 15:22:57	37.26N 142.54E	33.0	6.2Mb	A	OFF E COAST OF HONSHU, JAPAN
96/02/17 03:26:42	3.20N 147.39E	33.0	5.4Mb	B	E. CAROLINE ISL, MICRONESIA
96/02/17 05:59:33	0.50N 135.83E	33.0	8.0Ms	C	IRIAN JAYA REGION, INDONESIA
96/02/17 08:42:08	0.93S 136.02E	33.0	5.6Mb	B	IRIAN JAYA REGION, INDONESIA
96/02/17 10:18:03	6.94S 125.30E	541.0	5.9Mb	B	BANDA SEA
96/02/17 13:25:36	6.16S 154.49E	56.1	5.6Mb	B	SOLOMON ISLANDS
96/02/17 14:21:24	0.48S 135.91E	33.0	6.7Ms	B	IRIAN JAYA REGION, INDONESIA
96/02/17 20:17:50	0.76S 136.01E	33.0	6.6Ms	B	IRIAN JAYA REGION, INDONESIA
96/02/18 02:12:19	0.69S 136.45E	33.0	6.3Ms	B	IRIAN JAYA REGION, INDONESIA
96/02/18 02:25:37	1.40S 136.39E	33.0	6.4Ms	C	IRIAN JAYA REGION, INDONESIA
96/02/18 09:57:16	13.84N 120.60E	243.3	5.5Mb	B	MINDORO, PHILIPPINE ISLANDS
96/02/18 12:02:49	0.69S 136.40E	33.0	5.5Mb	C	IRIAN JAYA REGION, INDONESIA
96/02/18 13:58:16	0.55S 136.42E	33.0	5.5Mb	C	IRIAN JAYA REGION, INDONESIA
96/02/19 12:14:18	40.40N 142.40E	33.0	5.2Mb	B	NEAR E COAST OF HONSHU, JAPAN
96/02/19 23:48:36	20.42S 169.05E	33.0	5.6Mb	B	VANUATU ISLANDS
96/02/21 04:59:51	28.75N 34.85E	10.0	5.3Mb	A	EGYPT
96/02/21 12:51:04	9.66S 79.75W	33.0	6.7Ms	B	OFF COAST OF NORTHERN PERU
96/02/21 13:47:19	9.52S 80.18W	33.0	5.6Mb	C	OFF COAST OF NORTHERN PERU
96/02/22 08:38:36	8.57N 83.17W	33.0	5.0Mb	A	COSTA RICA
96/02/22 13:40:53	33.58S 71.29W	43.7	5.9Mb	A	NEAR COAST OF CENTRAL CHILE
96/02/22 14:59:09	45.28N 148.52E	133.3	5.9Mb	A	KURIL ISLANDS
96/02/24 15:52:58	0.87S 137.05E	33.0	5.9Ms	B	IRIAN JAYA REGION, INDONESIA
96/02/25 03:08:16	16.00N 97.90W	33.0	6.8		NEAR COAST OF OAXACA, MEXICO
96/02/25 04:17:09	22.20S 176.40W	33.0	5.6		SOUTH OF FIJI ISLANDS [UOA]
96/02/25 09:17:59	16.09N 97.88W	33.0	5.7Mb	A	OAXACA, MEXICO
96/02/25 14:17:20	12.92N 91.01W	33.0	5.5Mb	A	OFF COAST OF CENTRAL AMERICA
96/02/25 14:27:30	16.07N 97.66W	33.0	5.3Mb	A	OAXACA, MEXICO
96/02/25 16:14:10	35.72N 56.92E	33.0	5.2Ms	B	NORTHERN IRAN

APPENDIX A. LIST OF EARTHQUAKES USED IN THIS EXPERIMENT

83

96/02/26 01:37:32	15.78N	97.67W	33.0	5.1Mb	A	NEAR COAST OF OAXACA, MEXICO
96/02/26 07:17:24	28.27N	35.54E	10.0	5.1Mb	B	WESTERN ARABIAN PENINSULA
96/02/26 08:08:18	28.27N	57.21E	33.0	5.7Mb	B	SOUTHERN IRAN
96/02/27 18:03:03	14.12S	167.11E	33.0	5.7Mb	B	VANUATU ISLANDS
96/02/28 09:44:00	1.69N	125.93E	33.0	6.3Mb	B	NORTHERN MOLUCCA SEA
96/02/28 11:22:01	29.03N	104.78E	33.0	5.3Mb	B	SICHUAN, CHINA
96/02/29 19:39:57	24.04S	66.65W	200.0	4.9Mb	B	SALTA PROVINCE, ARGENTINA
96/03/01 06:48:55	34.26N	25.98E	33.0	5.1Mb	A	CRETE
96/03/02 01:50:04	6.11S	146.36E	63.2	6.1Ms	A	E NEW GUINEA REG., P.N.G.
96/03/03 02:41:25	0.56S	135.96E	21.0	5.7Ms	C	IRIAN JAYA REGION, INDONESIA
96/03/03 14:55:05	10.83N	86.64W	33.0	6.4Ms	B	OFF COAST OF COSTA RICA
96/03/03 16:37:26	11.12N	86.68W	33.0	6.6Ms	B	NEAR COAST OF NICARAGUA
96/03/04 15:59:05	2.62N	125.44E	146.2	5.9Mb	B	TALAUD ISLANDS, INDONESIA
96/03/05 14:52:32	24.75N	122.28E	33.0	6.4Ms	B	TAIWAN REGION
96/03/05 17:32:13	24.07N	123.27E	33.0	5.6Ms	B	SOUTHWESTERN RYUKYU ISLANDS
96/03/06 01:35:02	18.50S	175.02W	133.3	5.3Mb	A	TONGA ISLANDS
96/03/06 14:35:30	35.84N	139.07E	33.0	5.2Mb	B	NEAR S. COAST OF HONSHU, JAPAN
96/03/07 01:58:57	29.02N	138.34E	350.0	4.6Mb	B	SOUTH OF HONSHU, JAPAN
96/03/07 08:38:58	22.97S	70.08W	30.9	5.4Mb	A	NEAR COAST OF NORTHERN CHILE
96/03/07 12:41:04	18.37N	64.51W	76.2	4.7Mb	A	VIRGIN ISLANDS
96/03/09 16:15:37	43.60N	147.99E	33.0	5.9Ms	B	KURIL ISLANDS
96/03/09 22:35:38	37.03N	24.33W	10.0	5.3Mb	A	AZORES ISLANDS REGION
96/03/10 08:56:21	12.95S	69.25W	32.4	5.9Mb	A	CENTRAL PERU
96/03/12 03:44:25	8.93N	126.24E	55.8	5.4Mb	B	MINDANAO, PHILIPPINE ISLANDS
96/03/12 18:43:46	48.76N	87.90E	33.0	5.7Mb	B	NORTHERN XINJIANG, CHINA
96/03/13 16:26:31	6.23S	126.29E	33.0	5.5Mb	C	BANDA SEA
96/03/15 09:43:33	52.16N	30.11W	8.0	5.2Mb	A	NORTHERN MID-ATLANTIC RIDGE
96/03/16 22:04:06	29.06N	138.91E	476.3	5.9Mb	A	SOUTH OF HONSHU, JAPAN
96/03/17 14:48:56	14.74S	167.23E	164.4	6.0Ms	A	VANUATU ISLANDS
96/03/17 17:58:20	5.90S	147.42E	33.0	6.0Ms	B	E NEW GUINEA REG., P.N.G.
96/03/18 03:15:17	23.92S	66.89W	173.8	5.1Mb	B	JUJUY PROVINCE, ARGENTINA
96/03/18 09:04:48	21.44S	178.50W	400.0	4.9Mb	B	FIJI ISLANDS REGION
96/03/18 10:30:14	6.02S	147.36E	33.0	5.6Ms	A	E NEW GUINEA REG., P.N.G.
96/03/18 22:05:06	43.26N	147.05E	33.0	5.1Mb	A	KURIL ISLANDS
96/03/19 15:00:26	39.92N	76.69E	33.0	5.9Mb	A	SOUTHERN XINJIANG, CHINA
96/03/19 17:12:42	15.80N	97.20W	33.0	5.8Mb	A	NEAR COAST OF OAXACA, MEXICO
96/03/20 04:53:25	15.77N	97.23W	33.0	5.3Mb	A	NEAR COAST OF OAXACA, MEXICO
96/03/20 18:08:40	15.85N	97.22W	33.0	5.3Mb	A	NEAR COAST OF OAXACA, MEXICO
96/03/20 22:22:41	51.09N	29.56W	10.0	5.0Mb	B	NORTHERN MID-ATLANTIC RIDGE
96/03/22 08:26:38	40.10N	76.72E	33.0	5.1Mb	B	KYRGYZSTAN-XINJIANG BDR REG.
96/03/23 03:05:53	8.32N	72.68W	199.0	4.9Mb	B	VENEZUELA
96/03/23 07:10:36	51.03N	156.93E	33.0	5.0Mb	B	KAMCHATKA
96/03/24 03:19:34	10.58N	62.59W	65.2	5.0Mb	B	NEAR COAST OF VENEZUELA
96/03/27 12:34:49	16.43N	97.97W	33.0	5.5Mb		OAXACA, MEXICO
96/03/27 20:52:06	11.68N	87.99W	33.0	5.6Mb	A	NEAR COAST OF NICARAGUA
96/03/28 09:52:49	43.27N	147.06E	33.0	5.2Mb	B	KURIL ISLANDS
96/03/28 23:03:49	1.06S	78.60W	33.0	5.7Mb	A	ECUADOR
96/03/29 03:28:57	24.25N	122.39E	33.0	5.5Ms	B	TAIWAN REGION
96/03/29 04:59:56	10.31N	126.11E	33.0	5.3Mb	B	PHILIPPINE ISLANDS REGION
96/03/30 23:16:37	44.50N	149.23E	33.0	5.2Mb	A	KURIL ISLANDS
96/03/31 01:39:31	9.99S	160.69E	64.3	5.2Mb	B	SOLOMON ISLANDS

APPENDIX A. LIST OF EARTHQUAKES USED IN THIS EXPERIMENT

84

96/03/31 23:41:43	10.97S 165.41E	33.0 6.1Ms	B	SANTA CRUZ ISLANDS
96/04/01 03:43:02	16.59N 95.71W	58.1 5.1Mb	A	OAXACA, MEXICO
96/04/01 05:06:08	14.57N 93.51W	33.0 5.2Mb	A	NEAR COAST OF CHIAPAS, MEXICO
96/04/01 06:10:52	14.50N 93.36W	33.0 5.3Mb	A	NEAR COAST OF CHIAPAS, MEXICO
96/04/01 08:08:02	31.51N 73.52E	43.4 5.6Mb	A	PAKISTAN
96/04/02 07:59:23	37.83N 27.07E	10.0 5.2Mb	A	TURKEY
96/04/02 18:50:36	3.27N 125.87E	33.0 5.7Mb	B	TALAUD ISLANDS, INDONESIA
96/04/03 23:00:48	14.66N 93.44W	33.0 5.1Mb	A	NEAR COAST OF CHIAPAS, MEXICO
96/04/04 11:11:19	3.03N 126.28E	33.0 5.7Mb	B	TALAUD ISLANDS, INDONESIA
96/04/06 09:18:51	9.97S 75.42W	33.0 5.1Mb	C	CENTRAL PERU
96/04/06 22:04:41	44.31N 148.99E	33.0 5.3Mb	A	KURIL ISLANDS
96/04/07 00:07:25	44.40N 149.34E	33.0 5.3Mb	A	KURIL ISLANDS
96/04/07 14:18:59	53.29N 159.84E	51.0 5.3Mb	B	NEAR EAST COAST OF KAMCHATKA
96/04/08 16:49:42	6.18S 154.56E	57.2 5.6Ms	B	SOLOMON ISLANDS
96/04/08 20:46:38	10.61S 161.45E	61.2 5.3Mb	B	SOLOMON ISLANDS
96/04/10 23:24:13	13.02S 76.04W	70.3 5.0Mb	B	NEAR COAST OF PERU
96/04/11 10:51:14	56.96N 33.51W	10.0 5.0Mb	B	NORTH ATLANTIC OCEAN
96/04/11 11:24:25	10.77S 161.22E	33.0 5.8Mb	B	SOLOMON ISLANDS
96/04/12 18:45:49	6.04S 154.53E	33.0 5.9Ms	C	SOLOMON ISLANDS
96/04/12 22:31:06	56.97N 33.37W	10.0 4.9Mb	A	NORTH ATLANTIC OCEAN
96/04/15 14:55:32	6.07S 154.42E	55.3 5.7Mb	A	SOLOMON ISLANDS
96/04/16 00:30:53	24.09S 177.28W	109.8 6.8Ms	A	SOUTH OF FIJI ISLANDS
96/04/18 06:12:59	12.93N 125.00E	44.6 5.7Ms	B	SAMAR, PHILIPPINE ISLANDS
96/04/19 00:19:31	23.85S 69.99W	49.6 6.1Ms	A	NORTHERN CHILE
96/04/19 02:30:08	17.60S 179.77E	600.0 5.2Mb	A	FIJI ISLANDS
96/04/20 19:17:06	23.88S 66.70W	195.5 5.3Mb	B	JUJUY PROVINCE, ARGENTINA
96/04/20 23:03:31	22.02S 179.94E	610.0 5.1Mb	B	SOUTH OF FIJI ISLANDS
96/04/22 11:27:55	29.80N 129.03E	196.9 5.1Mb	B	RYUKYU ISLANDS
96/04/22 14:42:33	39.15N 47.31E	33.0 5.2Mb	B	ARMENIA-AZERBAIJAN-IRAN BORD
96/04/23 04:08:00	39.13N 141.33E	73.9 5.2Mb	B	EASTERN HONSHU, JAPAN
96/04/23 06:53:35	17.26N 101.28W	33.0 5.3Mb	A	NEAR COAST OF GUERRERO, MEXICO
96/04/24 09:36:23	17.84S 178.75W	500.0 5.1Mb	A	FIJI ISLANDS REGION
96/04/24 17:06:36	8.10S 74.27W	150.3 5.6Mb	A	PERU-BRAZIL BORDER REGION
96/04/24 18:56:22	18.81N 70.39W	79.6 5.2Mb	A	DOMINICAN REPUBLIC REGION
96/04/25 04:51:15	30.07S 71.02W	60.3 5.5Mb	A	NEAR COAST OF CENTRAL CHILE
96/04/25 05:50:08	21.97S 178.89E	641.6 5.1Mb	A	SOUTH OF FIJI ISLANDS
96/04/26 07:01:27	36.43N 28.13E	71.8 5.4Mb	A	DODECANESE ISLANDS
96/04/26 16:30:59	28.18N 87.65E	33.0 5.1Mb	B	XIZANG
96/04/26 17:03:44	44.51N 150.22E	33.0 5.3Mb	B	EAST OF KURIL ISLANDS
96/04/26 18:28:55	20.60S 179.13W	500.0 4.9Mb	B	FIJI ISLANDS REGION
96/04/27 00:16:19	54.05N 162.03E	33.0 5.3Mb	C	NEAR EAST COAST OF KAMCHATKA
96/04/27 03:01:04	52.57N 30.42W	10.0 4.6Mb	B	NORTHERN MID-ATLANTIC RIDGE
96/04/27 08:40:45	3.02N 79.29W	10.0 5.9Ms	B	SOUTH OF PANAMA
96/04/29 14:40:39	6.52S 154.80E	33.0 7.5Ms	B	SOLOMON ISLANDS
96/04/29 22:31:15	8.06N 39.02W	10.0 5.0Mb	B	CENTRAL MID-ATLANTIC RIDGE
96/04/30 05:27:40	6.29S 154.04E	33.0 5.5Mb	B	SOLOMON ISLANDS
96/05/01 09:21:23	6.59S 154.64E	33.0 6.0Ms	A	SOLOMON ISLANDS
96/05/01 10:05:09	6.67S 154.69E	33.0 6.0Ms	B	SOLOMON ISLANDS
96/05/02 02:32:34	6.32S 154.33E	33.0 6.0Ms	B	SOLOMON ISLANDS
96/05/02 05:45:12	31.92N 131.35E	33.0 5.1Mb	B	KYUSHU, JAPAN
96/05/02 06:38:24	6.61S 154.72E	33.0 5.5Mb	B	SOLOMON ISLANDS

APPENDIX A. LIST OF EARTHQUAKES USED IN THIS EXPERIMENT

85

96/05/02 13:34:19	4.40S	154.79E	400.0	5.7Mb	A	SOLOMON ISLANDS
96/05/03 03:32:48	40.83N	109.73E	33.0	5.7Ms	A	WESTERN NEI MONGOL, CHINA
96/05/04 16:13:04	13.89N	146.33E	33.0	5.6Ms	A	SOUTH OF MARIANA ISLANDS
96/05/04 16:49:24	13.90N	146.22E	33.0	5.7Ms	A	SOUTH OF MARIANA ISLANDS
96/05/07 08:44:36	1.56N	126.61E	33.0	6.0Mb	B	NORTHERN MOLUCCA SEA
96/05/07 21:43:40	14.93S	69.69W	242.0	5.1Mb	B	PERU-BOLIVIA BORDER REGION
96/05/07 23:19:59	43.67N	147.58E	50.0	6.2Ms	A	KURIL ISLANDS
96/05/10 10:19:38	13.88S	74.25W	101.1	5.3Mb	A	CENTRAL PERU
96/05/11 02:18:45	19.28N	64.95W	37.6	5.4Mb	A	VIRGIN ISLANDS
96/05/11 04:38:36	80.52N	2.20W	10.0	5.6Ms	A	NORTH OF SVALBARD
96/05/11 13:43:44	6.52S	154.85E	33.0	6.4Ms	A	SOLOMON ISLANDS
96/05/11 16:41:44	52.11N	30.02W	10.0	4.8Mb	B	NORTHERN MID-ATLANTIC RIDGE
96/05/13 09:59:20	4.73S	145.16E	195.2	5.2Mb	B	NR N COAST OF NEW GUINEA, PNG.
96/05/14 04:34:44	20.32S	69.19W	118.4	4.9Mb	B	NORTHERN CHILE
96/05/14 12:36:59	17.80S	178.74W	606.1	5.5Mb	A	FIJI ISLANDS REGION
96/05/14 17:34:10	24.28S	177.75W	167.8	5.2Mb	B	SOUTH OF FIJI ISLANDS
96/05/14 23:08:55	18.86S	174.12W	54.0	5.3Mb	B	TONGA ISLANDS
96/05/15 16:28:49	0.53S	135.73E	33.0	5.7Mb	B	IRIAN JAYA REGION, INDONESIA
96/05/18 03:30:19	54.95N	168.21E	33.0	5.1Mb	A	KOMANDORSKY ISLANDS REGION
96/05/18 07:42:25	23.11S	68.91W	96.5	5.3Mb	B	NORTHERN CHILE
96/05/19 23:21:41	1.30N	122.63E	33.0	5.6Mb	B	MINAHASSA PENINSULA, SULAWESI
96/05/22 20:26:32	20.99S	178.30W	435.0	5.0Mb	B	FIJI ISLANDS REGION
96/05/23 01:57:22	5.84N	77.47W	33.0	5.4Mb	A	NEAR WEST COAST OF COLOMBIA
96/05/24 06:35:55	27.79N	53.69E	10.0	5.2Mb	B	SOUTHERN IRAN
96/05/26 01:43:43	22.20S	171.23E	107.6	5.5Mb	A	LOYALTY ISLANDS REGION
96/05/26 07:31:00	22.58N	45.08W	10.0	4.6Mb	B	NORTHERN MID-ATLANTIC RIDGE
96/05/26 08:58:27	53.65N	154.08E	460.0	4.9Mb	B	SEA OF OKHOTSK
96/05/31 01:31:38	5.45S	147.86E	253.8	5.2Mb	A	E NEW GUINEA REG., P.N.G.
96/06/02 00:50:37	9.62S	79.52W	33.0	5.4Mb	A	OFF COAST OF NORTHERN PERU
96/06/02 02:19:32	30.51N	41.83W	33.0	5.1Mb	A	NORTHERN MID-ATLANTIC RIDGE
96/06/02 02:48:46	30.53N	41.73W	10.0	5.2Mb	B	NORTHERN MID-ATLANTIC RIDGE
96/06/02 02:52:09	10.64N	42.29W	10.0	6.8Ms	A	NORTHERN MID-ATLANTIC RIDGE
96/06/02 09:37:47	27.51N	128.53E	44.3	5.9Mb	B	RYUKYU ISLANDS
96/06/03 08:15:38	9.10S	156.88E	33.0	6.1Ms	B	SOLOMON ISLANDS
96/06/03 10:46:00	9.08S	157.00E	33.0	5.3Mb	B	SOLOMON ISLANDS
96/06/03 10:50:14	9.09S	157.01E	33.0	6.2Ms	B	SOLOMON ISLANDS
96/06/03 11:55:22	17.62N	94.23W	160.0	5.1Mb	A	CHIAPAS, MEXICO
96/06/04 23:22:03	18.57N	146.81E	33.0	5.5Ms	B	MARIANA ISLANDS
96/06/06 06:26:51	21.53S	169.03E	33.0	5.5Mb	C	LOYALTY ISLANDS REGION
96/06/06 09:04:59	6.72N	73.16W	160.1	4.5Mb	B	NORTHERN COLOMBIA
96/06/07 05:09:23	45.39N	26.97E	150.0	4.5Mb	B	ROMANIA
96/06/07 14:21:39	12.72N	88.09W	64.1	4.9Mb	A	OFF COAST OF CENTRAL AMERICA
96/06/08 02:55:57	41.62N	88.65E	0.0	6.0Mb	A	SOUTHERN XINJIANG, CHINA
96/06/08 05:26:08	58.31N	31.69W	10.0	5.1Mb	A	NORTH ATLANTIC OCEAN
96/06/09 01:12:17	17.50N	145.74E	146.6	6.0Mb	A	MARIANA ISLANDS
96/06/11 07:29:20	21.74S	176.34W	140.9	5.0Mb	B	FIJI ISLANDS REGION
96/06/11 16:52:12	17.26N	68.23W	33.0	5.2Mb	A	MONA PASSAGE
96/06/11 18:22:55	12.71N	125.00E	33.0	7.0Ms	B	SAMAR, PHILIPPINE ISLANDS